

# Investigation of photoinduced effects in plasmonic nanocavities

Présentée le 8 octobre 2021

Faculté des sciences de base  
Groupe Galland  
Programme doctoral en photonique

pour l'obtention du grade de Docteur ès Sciences

par

**Aqeel AHMED**

Acceptée sur proposition du jury

Prof. C. Bostedt, président du jury  
Prof. C. M. G. Galland, directeur de thèse  
Prof. G. Acuna, rapporteur  
Prof. F. Koenderink, rapporteur  
Prof. F. Stellacci, rapporteur





To see a world in a grain of sand  
and a heaven in a wild flower  
hold infinity in the palm of your hand  
and eternity in an hour

— Auguries of Innocence by William Blake

To my family...



# Abstract

Light matter interaction can be boosted by several orders of magnitude by tailoring the photonic environment, thus enabling a wide range of applications. One particular example are plasmonic nanostructures that support localized surface plasmon polariton (LSPP) leading to enhancement and confinement of incident electromagnetic fields. These novel properties provide access to a large number of optically driven effects within matter placed in the vicinity of such nanostructures. In this thesis, we investigate the effects of optical excitation on gold nanostructures in the presence of Raman active molecules. This is accomplished by fabricating nanoparticle on mirror (NPoM) plasmonic nanostructures where a gold nanoparticle is placed at a fixed distance from a smooth gold film using molecular monolayers. As the nanoparticle and mirror are placed only a few nanometers apart, optical excitation leads to formation of hybridized LSPP modes due to coupling between the plasmons within the nanoparticle and the mirror. This plasmonic coupling also results in confinement and subsequent enhancement of the incident light within the gap and is extremely sensitive to structural parameters of the NPoM. The creation of a homogeneous gap between the nanoparticle and mirror is quite challenging due the roughness of the mirror. Moreover, due to the large number of NPoM nanostructures present on the sample it is quite difficult to locate a specific NPoM. To bypass these difficulties atomically smooth and patterned substrates were developed using template stripping combined with conventional photolithography techniques. Next, in order to characterize the optical response of the NPoMs, a custom optical setup was built. The setup was primarily designed to investigate the plasmonic properties of the NPoM using elastic scattering spectroscopy along with surface enhanced Raman scattering (SERS) from the molecules within the gap. The combination of these two techniques was later used to investigate the effect of laser power on the NPoMs. It was discovered that the scattering spectra of the NPoMs changed irreversibly after laser exposure even with a few  $\mu\text{W}/\mu\text{m}^2$  incident intensities. Moreover, the plasmonic response of the NPoMs fabricated with well organized molecular monolayer changed much faster than the NPoMs prepared with disorganized ones. This phenomenon was also investigated in NPoMs prepared using a dielectric gap layer, by changing the gap conductivity, and by changing the nanoparticle shape. The experimental results combined with simulations suggest a decrease in gap height due to the reorientation of the molecular monolayer under optical excitation.

---

Key words: Localized surface plasmon polaritons, nanoparticle-on-mirror, bonding dipole mode, self-assembled monolayers, electrochemical characterization, scanning tunneling microscope, dark-field spectroscopy, surface enhanced Raman scattering.

# Contents

<b>Abstract</b>	<b>v</b>
<b>1 Introduction</b>	<b>1</b>
<b>2 Light and noble metal nanostructures</b>	<b>3</b>
2.1 Localized surface plasmons . . . . .	3
2.2 Coupled plasmonic nanostructures . . . . .	5
2.3 Fabrication methods . . . . .	6
2.4 Surface enhanced Raman scattering (SERS) . . . . .	8
2.5 Thermometry at the nanoscale with SERS . . . . .	10
<b>3 Sample Preparation</b>	<b>17</b>
3.1 Nanoparticle on mirror (NPoM) . . . . .	17
3.2 The ultimate mirror . . . . .	18
3.3 Patterned template stripped substrates . . . . .	19
3.4 The nLOF method . . . . .	20
3.5 The KOH etch method . . . . .	22
3.6 Method for spacer formation . . . . .	24
3.7 Self-assembled monolayers (SAM) . . . . .	26
3.8 Kinetics of self-assembly . . . . .	27
3.9 Molecular structure within self-assembled monolayers . . . . .	29
3.10 Protocol for SAM based NPoM on template stripped Au . . . . .	31
3.11 Protocol for SAM on Au nanoparticles . . . . .	31
<b>4 Experimental methods</b>	<b>33</b>
4.1 Electrochemical (EC) characterization . . . . .	33
4.2 Scanning tunneling microscopy (STM) . . . . .	34
4.3 Optical spectroscopy setup . . . . .	34
4.4 Setup calibration . . . . .	47
4.5 Repeatability . . . . .	48
4.6 Automation . . . . .	53

<b>5</b>	<b>Experiments and Results</b>	<b>57</b>
5.1	Raman measurement on silicon and diamond . . . . .	57
5.2	Effect of incubation time on NPoM . . . . .	61
5.3	EC and STM characterization of SAM . . . . .	62
5.4	SAM dependent optical stability of NPoM . . . . .	69
5.5	Measurements with constant laser power . . . . .	70
5.6	Measurements with increasing laser power . . . . .	73
5.7	Measurements on NPoMs with functionalized nanoparticles . . . . .	77
5.8	Measurements on NPoMs with conductive spacer . . . . .	82
5.9	Measurement on NPoMs with Au nanocubes (AuNCs) . . . . .	86
5.10	Comparing experiments and simulations . . . . .	89
<b>6</b>	<b>Conclusion and Outlook</b>	<b>95</b>
<b>A</b>	<b>Appendix</b>	<b>99</b>
A.1	Raman from citrates on ALD-NPoM samples . . . . .	99
A.2	Scattering at 632 nm (S2 BPT vs. S2 BPDT) . . . . .	100
A.3	Scattering at 632 nm Au nanocubes (S2 vs. S24) . . . . .	101
A.4	Effect of refractive index . . . . .	102
A.5	Effect of gap size with <i>s</i> polarization . . . . .	103
A.6	Effect of gap size with <i>p</i> polarization . . . . .	104
A.7	Effect of rotation with Au nanocubes . . . . .	105
	<b>Bibliography</b>	<b>117</b>
	<b>Curriculum Vitae</b>	<b>119</b>

# 1 Introduction

The surface charges within nanoscale metallic structures oscillate under the influence of an external electromagnetic (EM) field, resulting in localized surface plasmon resonances (LSPR). If two or more nanostructures are positioned within a few nanometers on each other, the LSPR of the individual nanostructures may hybridize resulting in new modes [1], each with a unique EM field distribution. In most cases the magnitude of the incident field is greatly enhanced within the gap due to the extremely localized surface charges [2]. This enhancement is very sensitive to the properties of the nanostructures, especially shape, size, material, angle of illumination, and the properties of the gap between nanostructures [3]. The enhancement and confinement of incident fields within the gaps of a few nanometers are used in a number of applications: chemical sensors [4], photodetection [5], photochemistry [6, 7], super-resolution imaging [8], and electro-optical conversion for integrated photonics [9, 10], to name a few. These structures are also very interesting from the aspect of fundamental science: confinement of light within atomic scale structures [11], strong coupling [12, 13] and nonlinear effects [14, 15] can also be observed. The oscillation of charges within plasmonic nanostructures when illuminated causes heating of the nanostructure due to Joules effect [16]. This property has been employed for thermal sensing and manipulation of biological specimens [17, 18]. In light of the above mentioned and many other potential uses, a vast library of plasmonic nanostructures have been designed and developed [19, 20]. The fabrication of plasmonic structures can be classified into top-down and bottom-up approaches. In the former approach, photolithography is used to create the nanostructures with dimensions ranging from a few 100's of nanometer down to 10's of nanometer. The latter approach utilizes the spontaneous self-assembly of nanostructures and is often employed to reach gap sizes even below a nanometer [21, 22].

The nanoparticle on mirror (NPoM) is a very specific bottom-up approach where a metallic nanoparticle is placed above a metallic film (mirror). The gap between the nanoparticle and the film can be formed in a number of ways including assembly of molecular layers, or growth of dielectric layers on mirror surface. The gap can also be defined by placing nanoparticles with metallic core and dielectric shell on pristine mirror surface. Simple fabrication along with freedom in the choice of structural parameters make the NPoM a very versatile platform used to study

## Chapter 1. Introduction

---

light matter interaction at the nanoscale. When illuminated, the incident electric field induces LSPR within the nanoparticle that interact with the charges in the mirror surface forming hybrid plasmonic modes with specific magnitudes of enhancement and confinement of the incident field. Owing to the great potential of these plasmonic properties, several studies have been undertaken in order to understand the plasmonic landscape within the NPoM [23, 24, 25, 26].

In this thesis, the interaction of a laser beam with the molecules forming the gap in NPoM structures is investigated. In Chapter 2, a brief overview of plasmonics and Raman scattering is presented. Next, in Chapter 3 the fabrication of NPoM structures on patterned, ultra-flat Au substrates is described. The details of the experimental techniques used to study the molecular monolayers and their impact on the optical response of the NPoM are discussed in Chapter 4. The specifics of the optical setup developed to characterize the NPoMs via combination of elastic and inelastic scattering spectroscopy are also mentioned in Chapter 4. The key experimental results including bulk and localized characterization of molecular assembly, using electrochemical (EC) characterization and scanning tunneling microscopy (STM), as well as the optical response of the corresponding NPoMs are described in Chapter 5. The EC and STM reveal that the molecular orientation is greatly dependent on the duration of self-assembly, yielding highly ordered and well packed monolayers for long assembly times while disordered layers for shorter one. The assembly time of molecules thus provides an additional degree of freedom to create NPoMs with a specific molecular orientation within the gap. Optical characterization reveals that the NPoMs with disordered molecular layer can sustain exposure to larger laser intensities than the ones formed using ordered ones.



## 2 Light and noble metal nanostructures

Light and its interaction with matter have always fascinated humanity partly due to its aesthetic value and partly by the enigmatic underlying principles that govern these phenomena. These interactions lie at an intersection of numerous arenas of science: physics, chemistry, mathematics, and biology to name a few. Hence, over the course of history scientists toiled to develop the theoretical and experimental foundations to aid in the investigation of light induced phenomena prompting major developments in our understanding of the nature of light. These advances allowed us to control light and to harness its power as a tool to manipulate matter, heralding the era of photonic devices such as light-emitting diodes, solar cells, lasers to name a few. The modern day internet also owes its feasibility to the developments made by the study of light matter interaction.

### 2.1 Localized surface plasmons

Over the last few decades, great efforts have been made to decrease the size of electrical and optical components in order to cater the ever growing demand for faster speed, greater functionality, lower power consumption and smaller mass. Thus, the study of light and its interplay with matter at the nanoscale is propelled by this necessity to create smaller devices. Moreover, from the perspective of fundamental science, the very nature of matter at nanoscale is significantly different from its macroscopic counterparts [27] hence the light matter interactions are also not the same and warrant further study. Due to the small size of atoms and molecules within a material compared to the wavelength of visible light, the probability of absorption and emission is relatively small [28]. Light matter interaction is significantly boosted by alteration of the photonic environment surrounding the material [20]. One particular example is the enhancement of the electric field component of the incident light in presence of noble metal nanostructures.

This phenomenon occurs due to the excitation of plasmons, quasiparticles attributed to the coherent oscillation of the surface density of free electrons within noble metals, by the electric field component of incident light. Considering a nanostructure much smaller than the wavelength

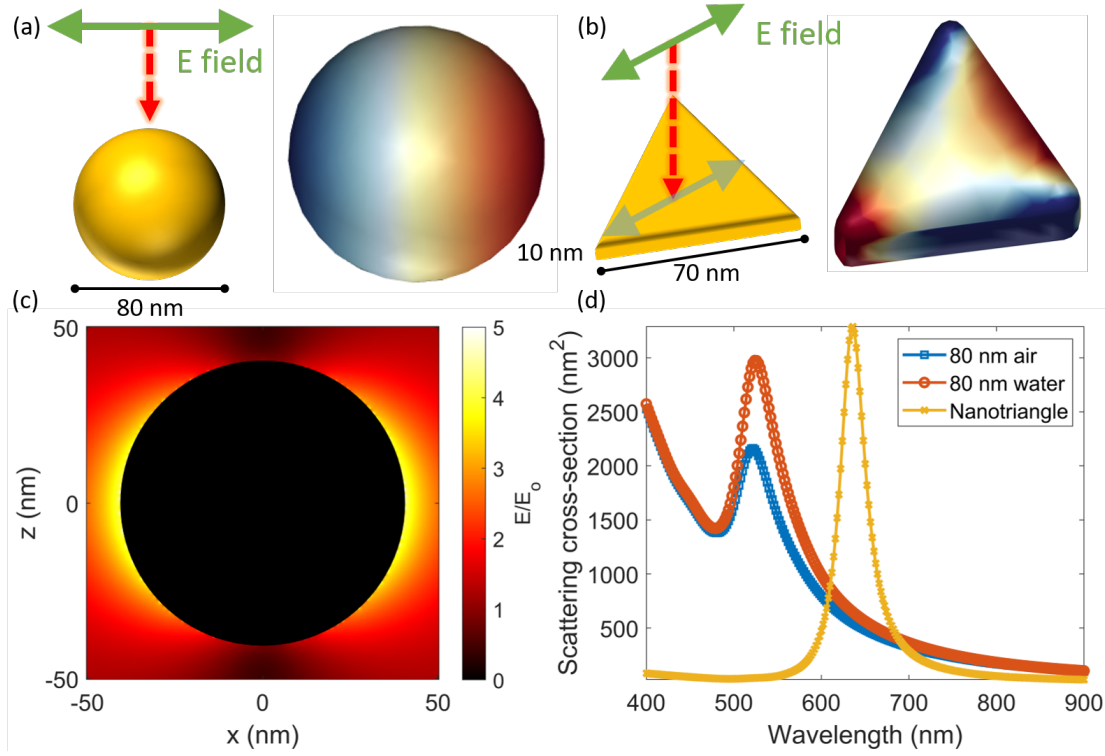


Figure 2.1: Linearly polarized light irradiating gold nanosphere with 80 nm diameter **(a)** and nanotriangle **(b)** results in oscillation of charges within the nanostructures (blue: positive, red: negative). Apart from the geometry of the nanostructure, the charge distribution is dependent on the wavelength and incidence angle of light. The charge distribution shown in **a**, **b** are for the wavelengths 530 nm and 620 nm respectively, with normal incidence. **(c)** The localized charges enhance the incident electric field  $E_0$  in their vicinity. **(d)** The impact of the dielectric environment and nanoparticle shape on the scattering spectrum: 80 nm gold nanosphere in air (blue line), 80 nm gold nanosphere in dielectric with refractive index  $n = 1.3$  (red), and nanotriangle in air (yellow). The charge distribution, electric field enhancement, and scattering spectra were calculated using MNPBEM 17 package [29].

of incident light (quasistatic approximation), all the electrons in the structure are driven simultaneously by the electric field thus segregating the negative (red) and positive charges (blue) (Figure 2.1 a). These charges oscillate with the electric field of the incident light forming a dipole (Figure 2.1 a, b). It is this confinement and oscillation of charges that leads to enhancement of the electric field (Figure 2.1 c). Apart from enhancing the incident electric field, the plasmons can also be used to manipulate and confine light to dimensions much smaller than its wavelength. The plasmons within metallic nanostructures are typically known as localized surface plasmon polaritons (LSPP) and can only be excited at a certain frequency of the incident light. This frequency is dependent on the material, size, shape and the dielectric environment and can be tuned by changing any of these parameters (Figure 2.1 d). This has prompted the development of new methods to synthesize metallic nanoparticles with well-defined shapes ranging from almost 2 nm up to several hundred nm (Figure 2.2).

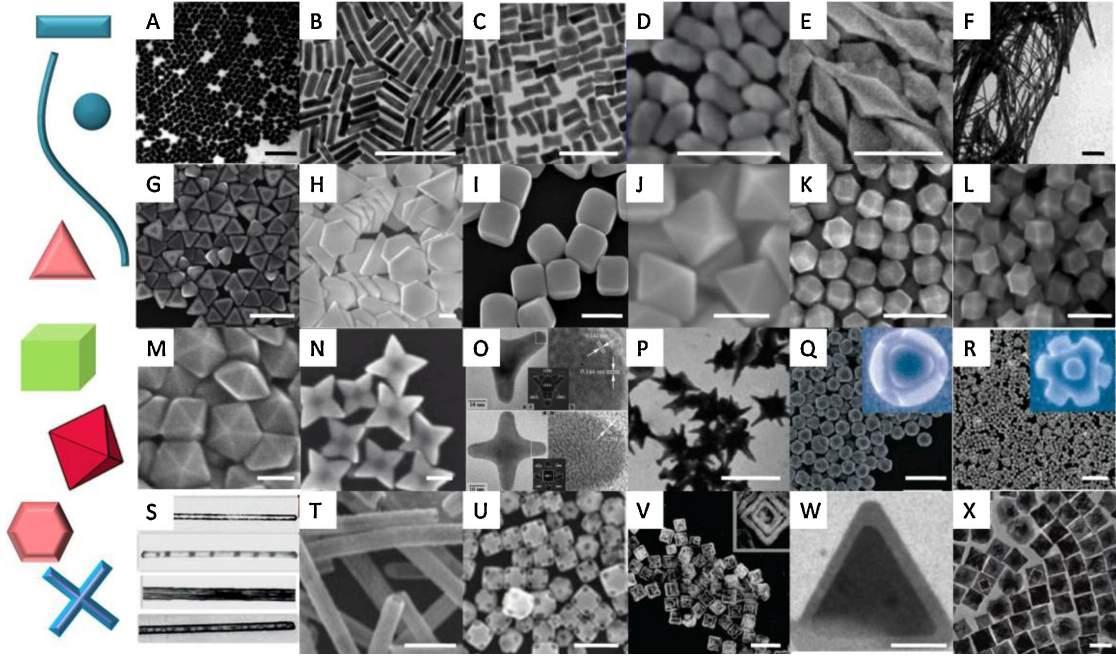


Figure 2.2: Different noble metal nanoparticle: (A) sphere, (B) rod, (C) dog bone, (D) peanut, (E) penta-branch, (F) wire, (G) triangular plate, (H) hexagonal plate, (I) cube, (J) octahedron, (K) cubooctahedron, (L) rhombic dodecahedron, (M) pentagonal bipyramid, (N) star-like octapod, (O) tripod (up) and tetrapod (down), (P) star, (Q) edge truncated octahedron, (R) octapod, (S) core-shell wire/cylinder, (T) tube, (U) cage, (V) double-walled box, (W) core-shell triangular plate, and (X) core-shell cube. Scale bar: 200 nm for A–E, G–I, K, L, P, R and T–V; 1  $\mu\text{m}$  for F and Q; 50 nm for J, M, N, W and X. Figure from [30].

## 2.2 Coupled plasmonic nanostructures

The LSPP of individual nanostructures placed in close proximity can also couple to form new modes corresponding to a distinct charge distribution in each case. This is achieved either by periodic arrangement of a large number of nanostructures or by bringing two or more individual nanostructures extremely close to each other. In the former case if the spacing between individual nanostructures is much larger than the wavelength of incident light, the nanostructures are said to be coupled in the far-field [31]. Alternatively, the nanostructures are said to be coupled in the near-field if the inter-particle spacing is smaller than the wavelength of light [31]. For this thesis, only the near-field case is investigated.

To illustrate the near-field coupling within metallic nanostructures consider two gold nanospheres (AuNS) with diameter 80 nm, placed 1 nm apart in a media with refractive index 1.3. The original LSPPs of the AuNS hybridize to form low and high energy modes which can be attributed to the Coulomb interactions between surface charges and can be observed in the scattering spectrum [25]. The mode at low energy (higher wavelength) is called the bonding dipolar plasmon (BDP) mode as the charges on the nanospheres form a tightly localized dipole within the gap. This extreme localization of charges on the surface of the AuNS enhances the incident field by several

orders of magnitude within the gap, which is often called a hotspot. A higher order dipole mode is also visible at shorter wavelength. In reality, as nanoparticles are not perfectly spherical, but rather have facets [32], cavity modes such as those found in metal-insulator-metal (MIM) junctions also exist within the gap [33] and may couple to the dipole modes to form hybrid modes. The resonance position for the BDP mode redshifts accompanied by a decrease of peak height as the distance between the AuNS is decreased [34]. This is caused by the enormous built-up of charges within the gap that hinder the oscillations of the dipolar mode. At even smaller gaps still ( $< 1$  nm), tunneling effects between the nanoparticles become dominant and the BDP blueshifts [35]. This gap dependent shift of the peak position and amplitude of the dipolar mode is therefore used to measure atomic scale changes in the spacing between coupled nanostructures [36].

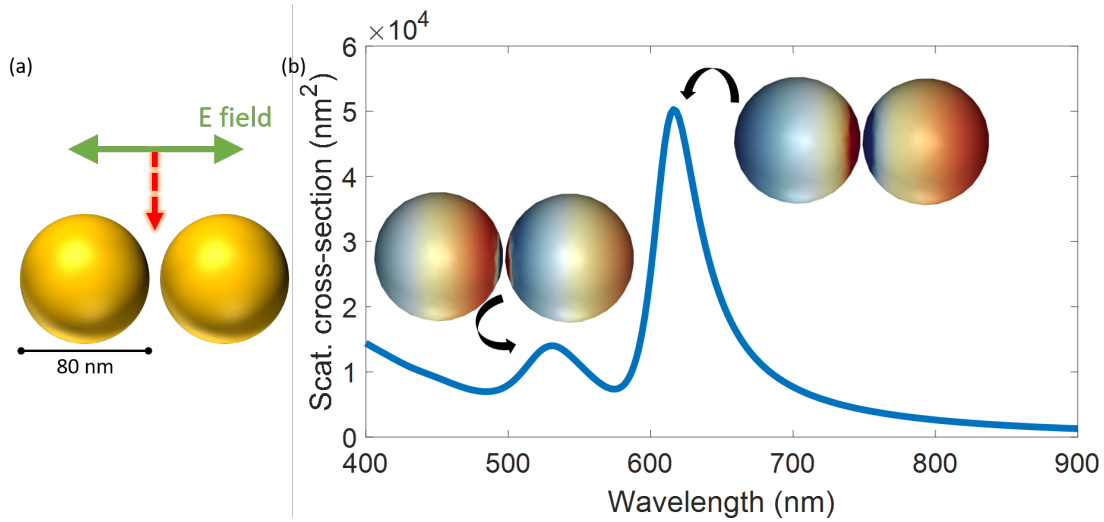


Figure 2.3: (a) Schematics of a dimer with 80 nm gold nanospheres separated by 1 nm illuminated with linearly polarized light. (b) The simulated scattering spectrum for the dimer shows two distinct plasmonic modes: the bonding dipole mode (BDP) at 620 nm and the higher order dipole mode at 530 nm. The charge distribution on the nanospheres depicts the tight confinement of charges that leads to several fold enhancement of the incident electric field within the gap (500 times for the BDP, 100 times for the higher order dipole mode).

### 2.3 Fabrication methods

In order to exploit the properties of coupled plasmonic nanostructures, a number of different fabrication methods have been developed. The most common approach is to deposit a metallic layer on a substrate and then pattern it to create nanostructures. Conventional photolithographic techniques are bound by the diffraction limit of light and are only able to reach a resolution of a few hundred nm. In order to fabricate even smaller structures with a resolution of tens of nm electron beam lithography (EBL), and focus ion beam (FIB) are used. The EBL is quite similar to photolithography, but with one key difference: in EBL a beam of electrons is used to write the pattern on the photoresist and is therefore not bound by the diffraction limit. Once the pattern is transferred to the substrate, conventional fabrication processes can be performed. On the other



hand, FIB uses highly accelerated ions of gallium, helium, neon, or beryllium to remove the material from the sample and thus directly fabricate the structure, bypassing other processes (i.e. photoresist development, etching, lift-off). However, both methods have very small throughput, as the beam needs to scan the entire surface. Moreover, extremely sophisticated equipment along with a well-controlled environment is necessary to obtain best results.

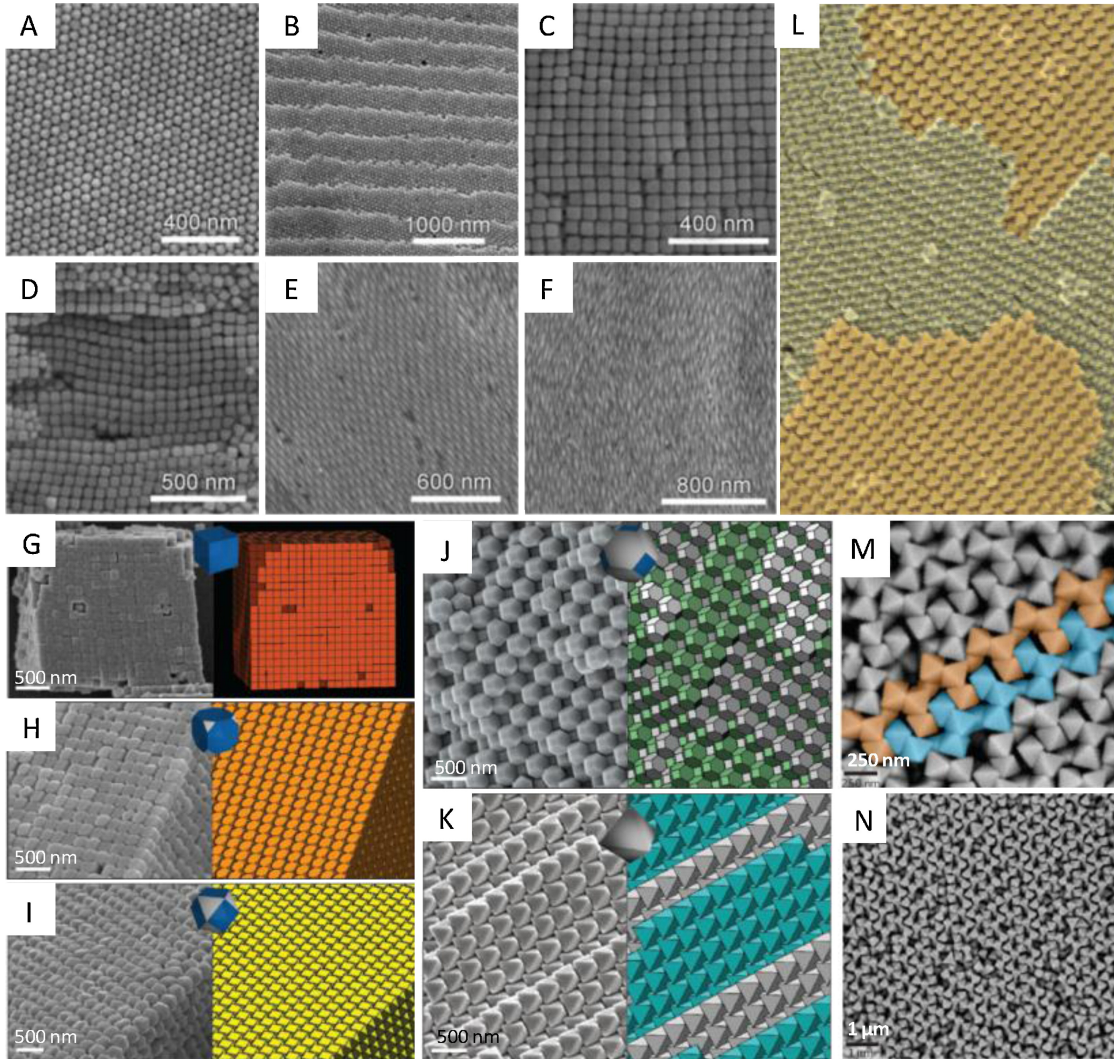


Figure 2.4: Scanning electron microscopy (SEM) images of the ordered assemblies formed from (A) hexagonally packed Au polyhedra, (B) hexagonally packed Au polyhedra with steps, (C) tetragonally packed Au nanocubes, (D) steps of the Au nanocubes at different layers, (E) 3D ordered superstructure formed from Au bipyramids, and (F) nematic superstructure formed from Au bipyramids. (G–N) Self-assembled dense Ag polyhedron lattices. Figure from [30]

Another approach is to assemble plasmonic nanoparticles in specific geometries (Figure 2.4). This can be accomplished in different ways depending on the properties of the nanoparticles and the required structure. Thin films and random structures composed of nanoparticles can be produced by depositing the nanoparticle solution on a substrate and letting the liquid evaporate.

This is a spontaneous process and takes place due to the convective flow and unequal density of nanoparticles at the interfaces [37]. It has been shown that complex structures can be obtained by engineering the interfacial layers [38, 39, 40]. The spontaneous assembly of nanoparticles can be performed in a more controlled manner by tuning the surfactants used to prevent the nanoparticles from agglomerating. An even more precise method is the selective functionalization of nanoparticle surface by block copolymers leading closely packed superstructures of nanoparticles [41]. The nanoparticles can be assembled in 2D and 3D structures using linker molecules such as cucurbit[n]uril (CB[n]) [42]. Deoxyribonucleic acid (DNA) strands have also been used for nanoparticle assembly into a number of structures [43]. This method allows a very flexible design where the inter-particle distances can be easily tuned by adjusting the length of the DNA strand [43].

While all the methods described above are ideal for large throughput of nanostructures with a huge number of hotspots, they have their limitations. The most common issue with the preparation of plasmonic nanostructures using these methods is the variation in the size of hotspots. Moreover, intensive chemical modification of the nanoparticle surface significantly alters its plasmonic response thus making it difficult to predict the optical properties of the assembled nanostructures. Finally, such methods are inherently subject to inhomogeneous broadening and cannot be used for single hotspot study, as is our goal in this thesis. The drawbacks of both the approaches described above are remedied by the nanoparticle on mirror (NPoM) geometry which allows to fabricate a large number of individual plasmonic nanostructures with extremely uniform gap size. This approach consists of a nanoparticle placed above a smooth substrate with a well-defined gap in between. The gap can be formed using organic or inorganic layers making the NPoM quite versatile in its applications. The freedom of choice in gap material, gap size and nanoparticle shape allow a tunable plasmonic response. Moreover, as a finite number of analyte molecules are present under the nanoparticle, the enhancement factor can be accurately estimated. This thesis focuses on the fabrication (Chapter 3: Sample preparation) and characterization (Chapter 5: Experiments and results) of the NPoM plasmonic nanostructures. Also, the interaction of incident light with molecules can be enhanced by placing the molecules between the nanoparticle and the mirror.

## 2.4 Surface enhanced Raman scattering (SERS)

Raman scattering, since its discovery in 1928 [44], has changed the paradigm for optical spectroscopy by enabling identification of the moieties present within an analyte by their unique vibrational signatures. Unlike Rayleigh scattering where the energy of the incident photons is conserved, Raman scattering is inelastic and the photons may lose a part of their energy, creating vibrations (phonon) within the analyte (Figure 2.5 a)<sup>1</sup>. As these vibrations are unique to the chemical bonds present within the analyte, thus the chemical composition can be determined by examining the energy difference between the incident and the scattered photons (Figure 2.5 b).

---

<sup>1</sup>In the following discussion, the term phonon is used to refer to the molecular vibrations.

## 2.4 Surface enhanced Raman scattering (SERS)

This type of Raman scattering is known as Stokes scattering. Alternatively, the incident photons may also gain energy during Raman scattering by taking energy from the phonons. However, as this process is dependent on the population of phonons, the emission is much smaller than Stokes emission. This type of scattering is known as anti-Stokes scattering. The probability of a molecule to undergo Raman scattering is given by its Raman cross-section and is different for Stokes and anti-Stokes scattering. Commonly both, Stokes and anti-Stokes emission, takes place via virtual energy level (off resonance Raman scattering), however if the incident photon is resonant with an electronic state present within the analyte, resonant Raman scattering may also occur. Within this thesis, the discussion will be limited to spontaneous Raman scattering only.

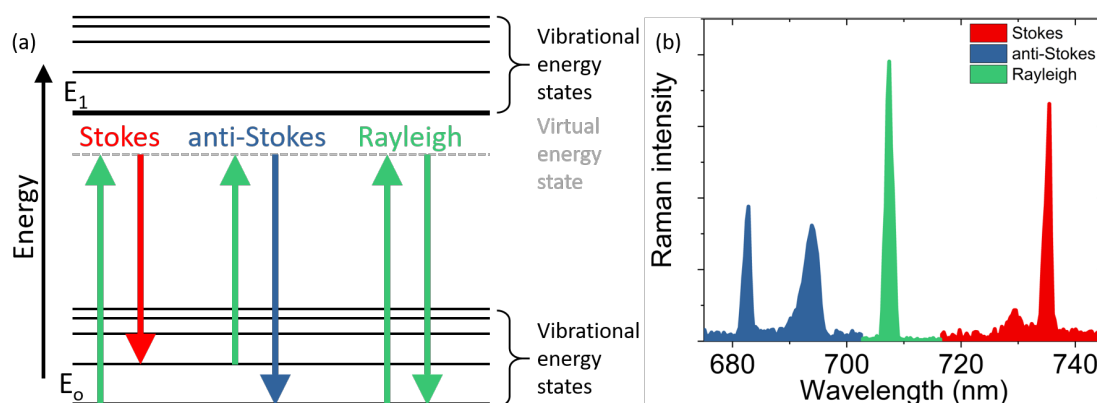


Figure 2.5: **(a)** Jablonski diagram showing the inelastic (Stokes and anti-Stokes) and elastic (Rayleigh) scattering of light via virtual energy state. **(b)** The anti-Stokes (blue) and the Stokes (red) sidebands of silicon using 710 nm laser wavelength. The anti-Stokes scaled up 10 times.

The Raman emission is very weak by itself and a large volume of the analyte along with high excitation powers are required to improve signal to noise ratio. This restricted the use of Raman spectroscopy for analysis of small analyte volume until the discovery of surface enhanced Raman spectroscopy (SERS) in 1974 by Fleischmann et al. [45]. Over the years, several variations of this technique have displayed many orders of magnitude enhancement of the Raman signal, hence enabling detection from monolayer up to single analyte molecule [46, 47]. This enhancement of the Raman signal was explained in multiple works [48, 49, 50], however the relation of SERS with LSPP was first suggested by Moskovits [51]. This suggests that in presence of an extremely localized electric field, the intrinsic Raman scattering of the analyte would be significantly enhanced. A new theory was recently developed which treats the molecule as an oscillator coupled to a plasmonic cavity, within the framework of cavity optomechanics [52, 53]. This theory predicts a new regime where an out of equilibrium phonon population in the analyte molecules is created by parametric amplification under laser excitation. This requires that the phonon creation rate be large compared to their decay rate, demanding extreme field confinement and enhancement.

In order to control and utilize the enhancement of the Raman signal, the substrates are usually engineered to contain several hotspots. This is accomplished either by using specifically designed

nanoparticles with sharp features (nano-urchin, nano-star) or by assembly of less intricate nanoparticles. The enhancement of the Raman signal is usually dependent on the enhancement of electric field  $E(\omega)$  within the hotspot normalized by the incident electric field  $E_0(\omega)$ , where  $\omega$  is the angular frequency of incident light. The difference in the frequency of the Raman mode  $\omega'$  and the incident light is taken into account by  $E(\omega')$  term and thus the SERS intensity is given by:

$$\text{Theoretical SERS enhancement} = \frac{|E(\omega)|^2 |E(\omega')|^2}{|E_0(\omega)|^4} \quad (2.1)$$

While this is a good approximation, the electric field enhancement is rarely homogeneous within plasmonic nanostructures due to irregularities of the surfaces. Moreover, plasmonic modes other than the dipole mode may have electric field distributions that may excite the analyte more efficiently. This can lead to Raman enhancement that is larger than the calculated values [54]. Thus it is often much simpler to determine the SERS enhancement experimentally by:

$$\text{Experimental SERS enhancement} = \frac{\frac{I_{SERS}}{N}}{\frac{I_o}{N_o}} \quad (2.2)$$

where  $N$  is the number of molecules within the plasmonic hotspot that result in SERS signal  $I_{SERS}$  while  $I_o$  is the Raman signal from the bulk with a known number of molecules  $N_o$ . The  $I_{SERS}$  and  $I_o$  need to be measured independently along with fairly good estimate of the number of molecules in each case. The methods to evaluate the SERS enhancement have been investigated in great detail by McFarland et al. [55]. The SERS enhancement does not necessarily require the analytes molecule to bind to plasmonic nanostructures, however the SERS intensity is also greatly dependent on the position of the analyte molecules with respect to the hotspot [56]. The binding of the molecules to the plasmonic structure can also contribute to the enhancement of the Raman signal. A molecule may bind with a nanostructure by Van der Waals forces (physisorption) or form a chemical bond (chemisorption) with the atoms of the nanostructure. In both cases, the Raman scattering of a bounded molecule is different compared to that of an unbound one. The Raman scattering may be altered even if the adsorption of molecule on the nanostructure does not create a new electronic state, but rather changes the geometry of the molecule [57].

### 2.5 Thermometry at the nanoscale with SERS

The Raman scattering, apart from its use in identification of molecular composition of analyte, can also be used to determine the temperature of the analyte. The bond length within a molecule is dependent on the temperature. Thus, any thermally driven change in the bond length results



in a shift in the Stokes peak. The temperature can then be estimated using this shift provided that the Stokes peak is sufficiently narrow and a high resolution spectrometer is used to obtain the Raman spectrum [58]. Another possible method is by taking anti-Stokes to Stokes ratio for a specific vibrational mode to determine the phonon population and using Fermi-Dirac, Bose-Einstein or Boltzmann distribution to obtain the temperature. This method requires simultaneous measurement of both Stokes and anti-Stokes peaks, and so using laser wavelength at 785 nm and measuring the temperature for a Raman mode at  $1500 \text{ cm}^{-1}$  would require a minimal spectral range from 700 nm to 900 nm. Therefore, depending on the wavelength of incident light and the Raman mode of interest, a spectrometer covering a large spectral range may be required. In this thesis, the discussion is restricted to the second method only.

The intensity of the Stokes ( $I_S$ ) emission is dependent on the intensity of the incident laser ( $I_L$ ), the number of molecules  $N$ , and the Stokes cross-section of each molecule  $\sigma_S$ . The Stokes emission is generally independent of the phonon population  $n$ , as the lifetime  $\tau$  of phonons is on the order of a few picoseconds and the typically vibrational modes have quantized energies larger than that available at ambient conditions leading to  $n \ll 1$ . On the other hand, the anti-Stokes intensity ( $I_{aS}$ ) is always dependent on the phonon population along with all the other parameters described above. As the Stokes and anti-Stokes emission occur at different wavelengths, the Raman cross-section of these processes are also different. In case of SERS, the LSPR may have a dramatic impact on the Raman cross-sections, depending on the laser detuning with respect to the resonance position. The expressions for the intensities of Stokes and anti-Stokes can be stated as [59]:

$$I_S = N\sigma_S I_L(1 + n) \cong N\sigma_S I_L \quad (2.3)$$

$$I_{aS} = nN\sigma_{aS} I_L \quad (2.4)$$

The phonon population  $n$  for a particular vibrational level, identified by Raman shift  $\tilde{\nu}$ , is dependent on two factors: thermal excitation and the optical excitation. Under normal Raman conditions, the phonon population is dominated by thermally excited phonons. However, under SERS conditions, the incident field is enhanced by several order of magnitudes and thus the optically excited phonons may have a major contribution to the phonon population as well. Taking into account the thermal and the optical influences the rate of change of phonon population can be expressed as [59]:

$$\frac{dn}{dt} = \frac{\sigma_S I_L}{\hbar\omega_L} + \frac{\exp\left(\frac{-hc\tilde{\nu}}{k_B T}\right)}{\tau} - \frac{n}{\tau} \quad (2.5)$$

where  $c$  is the speed of light in vacuum,  $k_B$  is the Boltzmann constant,  $T$  is the temperature,  $h$  is the Planck's constant, and  $\hbar$  is the reduced Planck's constant. The first term in Equation 2.5 specifies the optical excitation with frequency  $\omega_L$  while the second term refers to the thermal influence. The third term accounts for the inverse proportionality of phonon pumping rate with phonon lifetime. If the laser power is extremely high, phonon excitation rate may become comparable to phonon lifetime resulting in an out of equilibrium phonon population. This is known as vibrational pumping. Alternatively, under weak excitation, the steady state phonon population ( $\frac{dn}{dt} = 0$ ) is given by [59]:

$$n = \frac{\tau\sigma_S I_L}{\hbar\omega_L} + \exp\left(\frac{-\hbar c\tilde{\nu}}{k_B T}\right) \quad (2.6)$$

In case of weak optical excitation and to account for the small Stokes cross-section ( $10^{-28} \text{ m}^2$ ) the above equation can be further simplified by removing the first term, yielding [59]:

$$n = \exp\left(\frac{-\hbar c\tilde{\nu}}{k_B T}\right) \quad (2.7)$$

Inserting Equation 2.7 into Equation 2.3 and Equation 2.4 and taking the ratio of anti-Stokes to Stokes intensity results in the following expression:

$$\rho = \frac{I_{aS}}{I_S} = \frac{\sigma_{aS}}{\sigma_S} \exp\left(\frac{-\hbar c\tilde{\nu}}{k_B T}\right) \quad (2.8)$$

The  $\frac{\sigma_{aS}}{\sigma_S}$  factor may be approximated by  $\left(\frac{\omega_{aS}}{\omega_S}\right)^3$  or  $\left(\frac{\omega_{aS}}{\omega_S}\right)^4$  depending on the method of detection. The dependence of anti-Stokes to Stokes ratio on the energy of the Raman mode as well as the temperature is shown in Figure 2.6. Beginning with the Raman mode located at low energies, the phonon population is significantly dominated by thermal contribution however larger energy levels are much more sparsely populated. As the temperature is decreased, the curve becomes independent of temperature as the exponential term is very small. Thus in this regime the phonon population is maintained by optical pumping. The temperature where the transition between the two regimes occur is known as cross over temperature  $T_{cr}$ .

Alternatively, for sufficiently low laser powers, by inserting the measured  $\frac{I_{aS}}{I_S}$  in to Equation 2.8 and rearranging, the temperature  $T$  can be measured [60]. An example using the SERS signal from biphenyl-4-thiol (BPT) molecules in NPoM is shown in Figure 2.7. The NPoM was excited with approx. 10  $\mu\text{W}$  at 710 nm and the scattered anti-Stokes (Figure 2.7 a) and Stokes (Figure

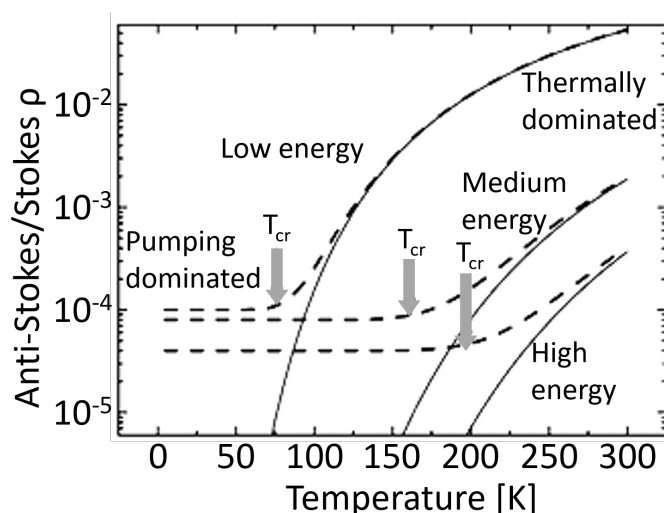


Figure 2.6: The dependence of anti-Stokes to Stokes ratio ( $\rho$ ) on temperature and the energy of the vibrational modes. At low temperatures the phonon population is independent of the temperature and solely dependent on optical excitation. At high temperatures, the phonon population is maintained by thermal contributions. The transition between these two regions occurs at cross over temperature  $T_{cr}$ . Figure from [59].

2.7 b) signals are recorded. The acquisition of Raman signal was divided in 22 measurements (white dashed line), with 150 Raman spectra per measurement. The anti-Stokes and Stokes signal for the vibrational modes at  $1079\text{ cm}^{-1}$ ,  $1251\text{ cm}^{-1}$ , and  $1586\text{ cm}^{-1}$  are then used to extract the temperature, from each spectrum (Figure 2.7 c), as well as from the mean spectrum of a measurement (Figure 2.7 d). The calculated values of temperatures are reasonable, however it must be noted that the anti-Stokes signal is very small and could leads to errors in determining the temperature. Moreover, the effect of overlap between plasmonic resonance and Raman lines was also not considered [61]. Therefore, in this thesis only temperature measurements on silicon and diamond (Chapter 5) are reported, leaving the treatment of NPoM for future studies.

There is yet another technique that can be used to determine the temperature of plasmonic nanostructures and requires neither the anti-Stokes nor the Stokes peaks. Rather the exponentially decaying background under the anti-Stokes peaks is used, and is found to be present in plasmonic nanostructures regardless of the presence of molecules. For a long time this spectral feature has been largely ignored; in part due to its elusive origins and in part as it contain no signature from the analyte. The broad emission is fundamentally different from the discrete Raman or electronic transitions and points to continuum of states with lifetimes much shorter than other transitions. The underlying reason for this broad emission, especially for gold nanostructure, has been a matter of debate with two main phenomena: photoluminescence and electronic Raman scattering. In the former case, a transition between the electronic bands, specifically the sp band and the d band in gold, leads to inelastic emission [62, 63]. This type of interband transitions occur when Au is excited with photon energies exceeding 2.4 eV, however the anti-Stokes

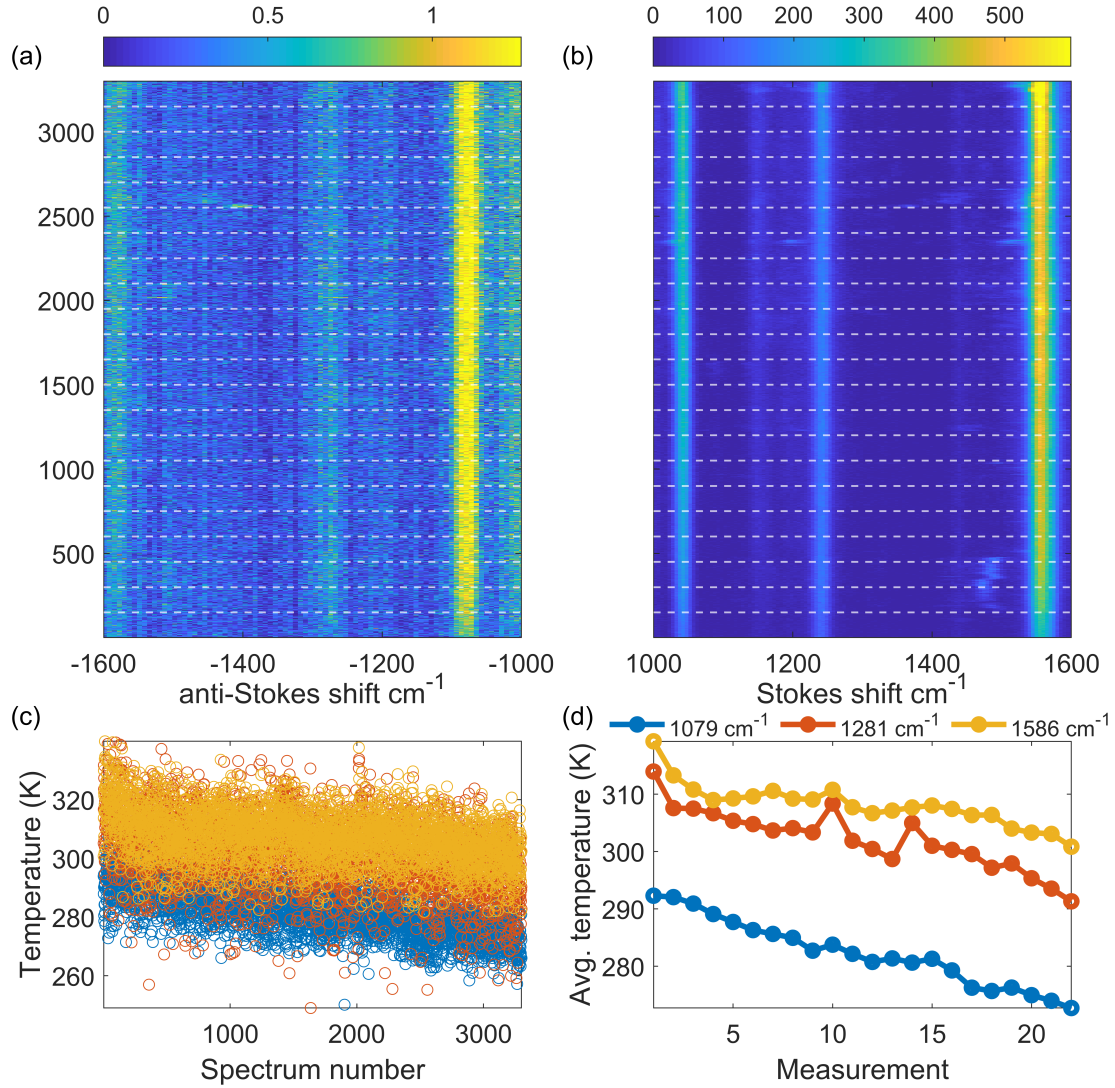


Figure 2.7: SERS spectra with anti-Stokes **(a)** and Stokes **(b)** sidebands of BPT in NPoM. The spectra were acquired in 22 measurements (white dashed line) with 150 spectra per measurement with 1 second integration time. **(c)** Temperature calculated for each spectrum using the anti-Stokes and the Stokes peaks from 3 vibrational modes. **(d)** Temperature calculated for each measurement by the anti-Stokes and the Stokes ratio of the mean Raman spectra of a measurement.

background was also found when excited with lower photon energies [64]. This implies that interband photoluminescence cannot be the only cause of the anti-Stokes background, nonetheless intraband photoluminescence might still contribute [65]. On the other hand electronic Raman scattering explains the anti-Stokes background as inelastic scattering of light by the electrons in the sp band. The incident photon excites the electrons present at an energy level just above the Fermi energy to a virtual state, later returning to energy level just below the Fermi energy [66]. Thus, the scattered photon is blueshifted compared to the incident photon. The required momentum for this transition is provided by the localized electric field present in plasmonic

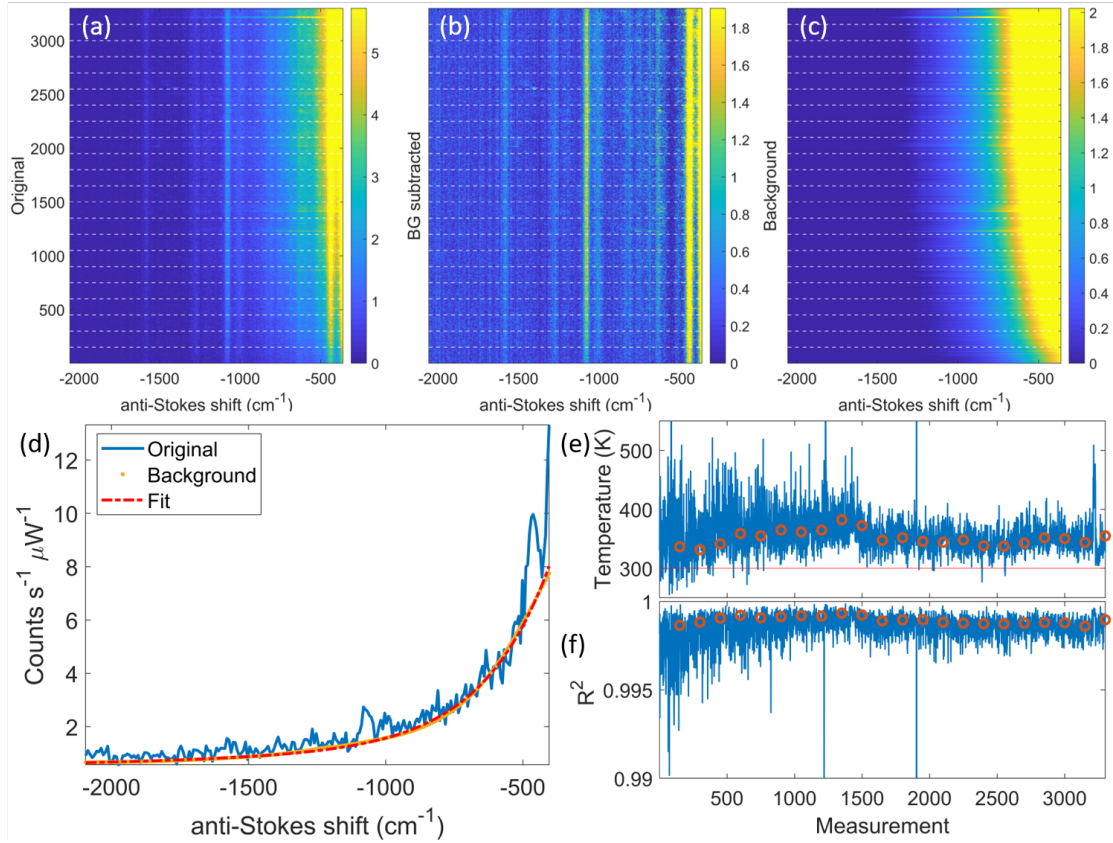


Figure 2.8: The acquired anti-Stokes (a) signals are used to extract the anti-Stokes Raman peaks (b) and the underlying background (c). The anti-Stokes Raman peaks can be used along with the Stokes to extract the temperature as shown in Figure 2.7 while the background is fit by an exponential to extract the temperature (d). The extracted values of temperature (e) as well as the corresponding R-squared values (f). The blue lines denote the values calculated for each spectrum while the red circle denotes the value extracted from the mean spectrum of a measurement.

nanostructures [66]. As the electronic Raman scattering can also occur at wavelengths much longer than those required for interband transition, this mechanism better explains the origin anti-Stokes background. Sample temperature can be extracted by appropriately fitting the background using either Fermi-Dirac [67] or Bose-Einstein [68] distribution. Recently, it was also suggested that the difference between these two distributions not significant below  $1000 \text{ cm}^{-1}$  and as such can be modelled by Boltzmann statistics [69]. This approach was applied to the anti-Stokes data from the Raman spectra in Figure 2.7. First, the original anti-Stokes portion (Figure 2.8 a) is used to extract the anti-Stokes peaks (Figure 2.8 b) and the anti-Stokes background (Figure 2.8 c). This background is then fit using the Boltzmann distribution (Figure 2.8 d) and the returned argument of the exponential function is used to extract the temperature (Figure 2.8 e) for a certain goodness of fit (Figure 2.8 f). This method can be applied to each spectrum (blue line, Figure 2.8 e, f) or to the average spectrum of a measurement (red o, Figure 2.8 e, f). The observed values are quite close to those measured earlier using the ratio of anti-Stokes and Stokes intensities (Figure

2.7).

## 3 Sample Preparation

This chapter describes the fabrication of plasmonic nanocavities that were used in the experiments. The chapter begins with a brief overview of the NPoM structure followed by the development of patterned, ultraflat gold substrates that serve as the mirror for NPoM. The various methods of crafting nanometer scale spacer for the NPoM are also mentioned. The history and kinetics of molecular self-assembly are also concisely described. Finally, a detailed description of the protocols used in this thesis is presented.

### 3.1 Nanoparticle on mirror (NPoM)

The nanoparticle-on-mirror (NPoM) geometry is a type of bottom-up fabrication method that combines easy fabrication and high reproducibility. The NPoM comprises of a nanoparticle that is positioned on top of a metallic substrate (mirror) with a controlled distance between them created using a spacer (Figure 3.1). A number of different materials may be used to function as the mirror and the nanoparticle; the most common among them being gold and silver although metal dielectric hybrid NPoMs have also been developed [70]. In order to obtain a specific plasmonic response the nanoparticle shape and size along with the gap height are usually tuned. NPoM can be formed using nanospheres, nanocubes, or nanorods with sizes from a few 100's of nanometer down to a few nanometers. The gap height is dependent on the material chosen as spacer and could be scaled from a few nanometers with Raman active molecules and quantum emitters down to sub nanometer regime with single layer 2D materials such as graphene. Apart from single nanoparticles, dimers and oligomers can also be fabricated upon the mirror substrate. The large number of possible configurations combined with the simplicity and ease of fabrication make the NPoM an attractive system.

To the best of our knowledge, the first demonstration of NPoM can be traced back to the enhancement of light emission from metal-insulator-metal tunnel junctions observed by McCarthy et al. [71] in 1977. A few groundbreaking experimental studies include the works of Holland et al. [72]; with silver flakes on top of silver films with lithium fluoride spacer, and Kume et al. [73];



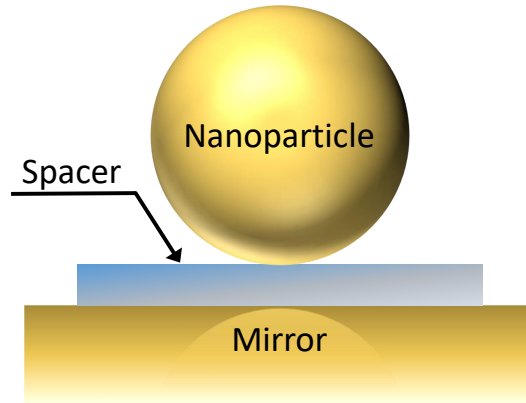


Figure 3.1: Schematics of an ideal nanoparticle on mirror plasmonic nanostructure formed of three components: an ultraflat mirror, a well-defined spacer, and nanoparticle on top

with silver nanoparticles embedded in silica matrix on top of silver film. NPoM with molecular self-assembled monolayers as spacer layer were introduced at the beginning of the 21<sup>st</sup> century by Hutter et al. [74] and Okamoto et al. [75] Since then the NPoM has been studied extensively in a number of works primarily focusing on sub-5 nm gaps [25, 76, 77, 26, 78, 79, 80]. (The text in this paragraph is extracted from [81].)

The NPoM not only enables to circumvent the limits imposed by conventional photolithography processes but also provides easy access to novel light matter interactions due to the huge enhancement and extreme confinement of light. These unique properties can allow the observation of the quantum limits to field confinement due to effects such as charge tunneling across the spacer [82]. The field enhancement and confinement to very small mode volume renders the coupled plasmonic modes of the NPoM extremely sensitive to structural variations, [3] mainly to the properties of the spacer and hence the NPoM can be employed to study light matter interaction at the nanoscale.

## 3.2 The ultimate mirror

The need for extremely smooth substrates is driven by the constraints on gap height of NPoM. Noble metal thin films deposited using physical vapor deposition method such as electron beam (e-beam) evaporation and sputtering require a few nanometers of chromium (Cr) or titanium (Ti) to serve as an adhesion layer between the gold thin film and the substrate. It has been shown that Cr and Ti have a significant impact on the morphology and other physical properties of gold layers [83, 84]. The values of root mean square (RMS) roughness for such substrates may range from a few nanometers to a few 10's of nanometer. While such layers could serve as mirrors in micron scale optical cavities, for NPoM as the gap is decreased below 5 nm the roughness of the substrate tends to become comparable to the gap height and hence can result in an inhomogeneous gap height. Such distortion within the gap lead to deterioration of plasmonic response and complicates modelling of such structures.



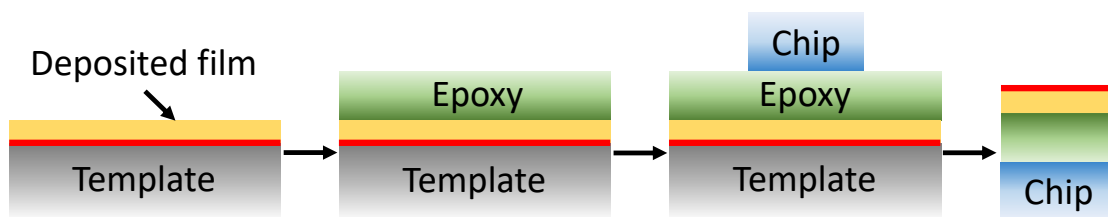


Figure 3.2: Schematic representation of template stripping technique. First, a thin film is deposited on a smooth substrate. The interface between the thin film and the substrate is colored red. Next, an epoxy is applied on top of the film and another smaller piece (chip) attached. The epoxy is then cured to strengthen the adhesion. Finally, the chip is pulled out, removing the thin film along with it. The surface of the thin film that was initially at the interface with the template becomes the top surface after stripping the chip.

A number of methods have been developed to improve the roughness of deposited noble metal substrates. These include replacement of Cr/ Ti adhesion layer by organic molecules [85], 2D materials [86] or encapsulated annealing of the deposited film [87]. One such method developed by Hegner et al. [88] in 1993 known as template stripping is commonly used to obtain polycrystalline substrates with atomic scale roughness. The required thin film is first deposited on a smooth substrate, such as mica or single crystal silicon, that acts as a template (Figure 3.2). Next, small chips are attached to the thin film using an adhesive. After curing the adhesive, the chip is removed along with the thin film. In doing so, the surface of the film that was initially in contact with the template (red region in Figure 3.2) becomes the top surface of the film-adhesive-chip structure with ultraflat surface. Other than its simplicity, the major advantage of this method is the absence of chemical precursors and longer shelf life guaranteeing pristine surfaces for experiments.

In order to compare the quality of e-beam evaporated Au films to their template-stripped counterparts we investigated the two types of samples under scanning electron microscope (SEM) and atomic force microscope (AFM) as shown in Figure 3.3. The films used were deposited on the same silicon wafer without any adhesion layer. The SEM and AFM scans show considerable improvement in the grain size and film quality with almost 5 times less roughness with the template-stripped film.

### 3.3 Patterned template stripped substrates

As the template-stripped films enable to produce nanocavities with uniform gap heights, a method to locate specific nanocavities is also necessary for complete characterization across multiple instruments. For this purpose, we developed a scheme of “markers” using photolithography to aid in locating NPoMs efficiently. The scheme involves dividing a sample into 9 sections, where each section contains 10 rows and 10 columns of rectangular markers, each enclosing a region of almost  $30\text{ }\mu\text{m} \times 30\text{ }\mu\text{m}$  and with a  $30\text{ }\mu\text{m}$  distance between each marker. Within a section, the markers were labelled with the section, row and column number using dots. In order to achieve

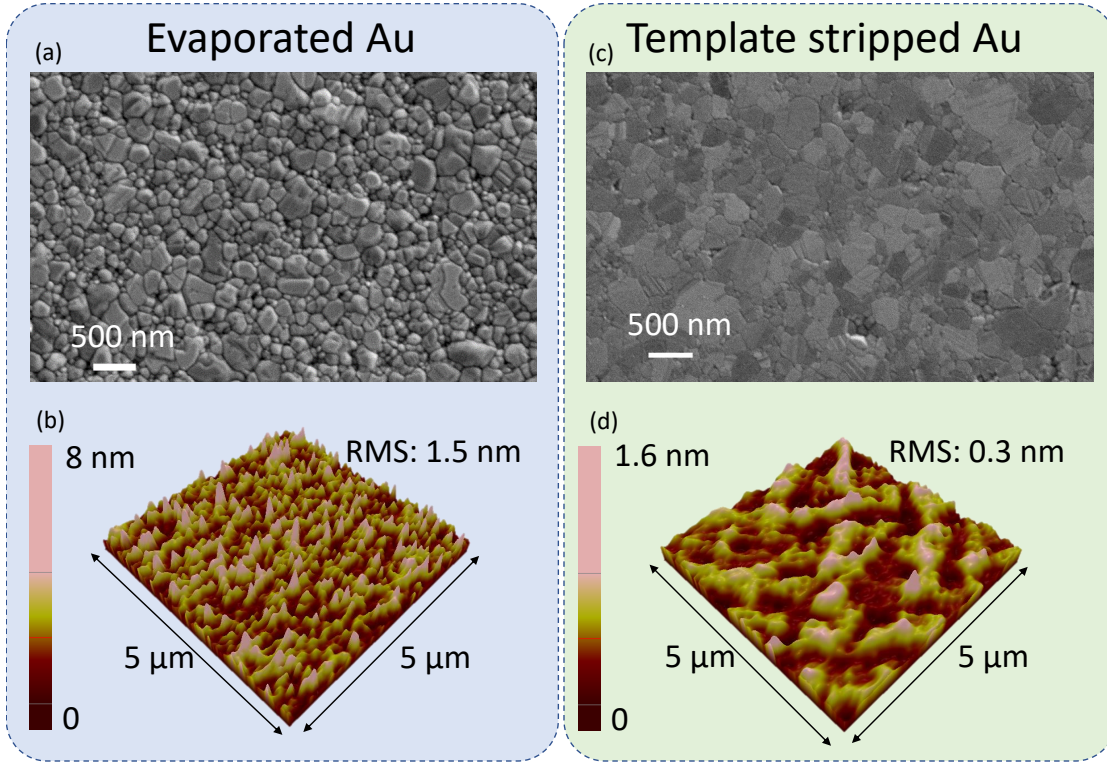


Figure 3.3: (a, c) The SEM images show the distinction between evaporated and template stripped gold, with the latter showing a better surface roughness than the former. (b, d) A more quantitative estimate of surface roughness can be extracted by AFM scans depicting an RMS roughness value of 1.5 nm and 0.3 nm for evaporated and template stripped gold respectively.

this, two processes were developed namely: the negative lift off (nLOF) and potassium hydroxide (KOH) etch. It has been shown before that micro and nanostructured films can also be template stripped by forming the desired structures on the template before deposition of the thin film [89].

### 3.4 The nLOF method

The nLOF process begins with coating a 100 mm diameter silicon test wafer with a  $1.4\ \mu\text{m}$  thick layer of negative photoresist (PR) AZ nLOF 2020 using an automatic coater ASC 200 (Figure 3.4 a step 1). The wafer is then exposed in a mask aligner (MA6 Gen3) at i-line (365 nm) with a dose of approximately  $90\ \text{mJ}/\text{cm}^2$  in contact mode with a mask (Figure 3.4 a step 2). The mask contains the layout of the marker scheme and hence during exposure this layout is imprinted on the PR. The unexposed PR is removed during the development procedure and only the regions exposed to the UV light remain on the wafer (Figure 3.4 a step 3). Next, a 200 nm gold film is deposited at a rate of  $5\ \text{\AA}/\text{s}$  using e-beam evaporation (EVA 451) (Figure 3.4 a step 4). The deposition were carried out in ultra-high vacuum (UHV) with pressure slightly above  $10^{-7}$  mbar. No Cr or Ti adhesion layer was used between gold and silicon. SEM images indicate that the Au layer does not completely cover the PR structures (Figure 3.4 c). Conventionally, the nLOF is to

be removed after evaporation however without the adhesion layer between gold and silicon PR removal leads to delamination of the gold film. Hence, the nLOF is not removed. The next steps in the process are identical to conventional template stripping. The wafer is heated up to 60 °C on a hotplate and held there while a thermal curing epoxy (EPO-TEK 377) is used to attach 10 mm × 10 mm Si chips on top of the wafer (Figure 3.4 a step 6). Once the chips are attached the temperature is increased to 150 °C and held for 2 hours before slow cooling it back to room temperature. The silicon chips can then be peeled off for experiments as needed (Figure 3.4 a step 7). The unique values of section, row and column can be used to locate any structures present in the vicinity (Figure 3.4 b).

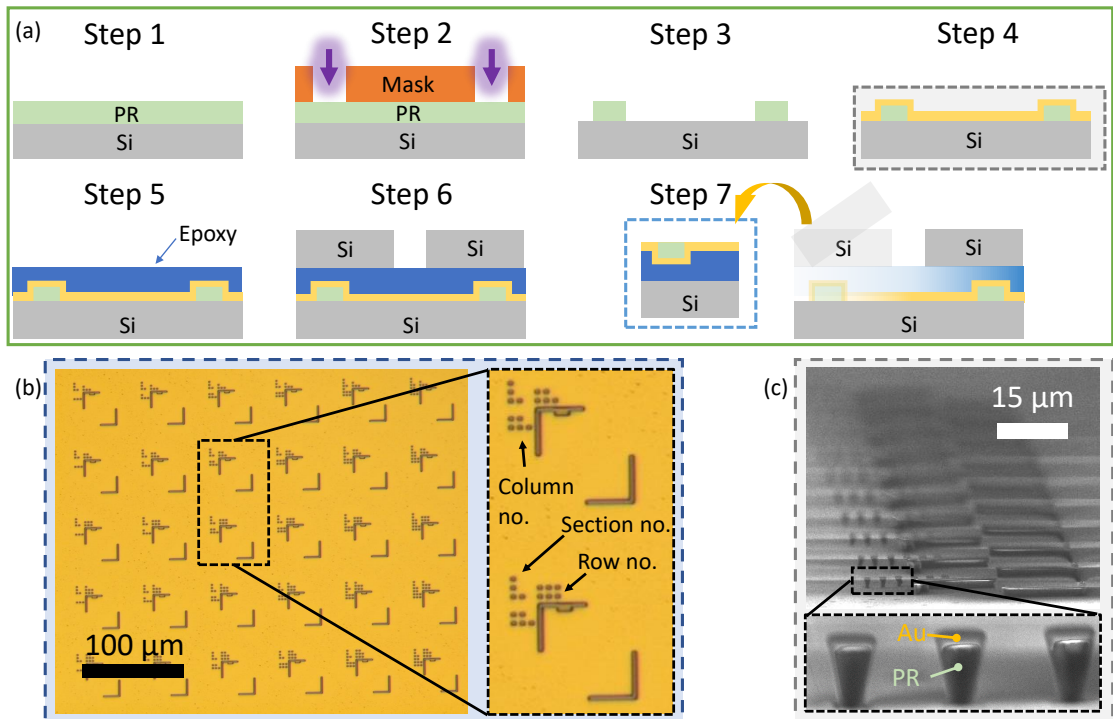


Figure 3.4: **(a)** Step by step fabrication of patterned, template stripped samples via nLOF method. **(b)** A microscope image of a section of markers. The zoomed view show the dots indicating the section, row and column numbers. **(c)** SEM image showing upright standing markers. The gold thin film is distinctly visible on top of the negative photoresist.

While the nLOF method provides easy access to marked template stripped samples by mere 7 steps, it is not suitable when the sample has to be incubated in solution for duration exceeding 2 hours. The problem arises due to the reaction between the PR and the solvent in which the sample is being incubated. The solvents tend to dissolve the PR over time leading to severe contamination and distortion of the template stripped surface (Figure 3.5). Dark-field imaging reveals numerous contaminations on the surface of the sample after incubation for 24 hours in ethanol solution (Figure 3.5 a). Using white light interferometry we found deformations in the film surrounding the marker region. We also note that the PR at the marker position has been removed as seen by black region in (Figure 3.5 b). The removal of the PR is related to the contact

region with the solvent, the smaller the contact the less the PR is removed. The solvent was also found to react with the epoxy causing loss of adhesion and resulting in distortion of the surface.

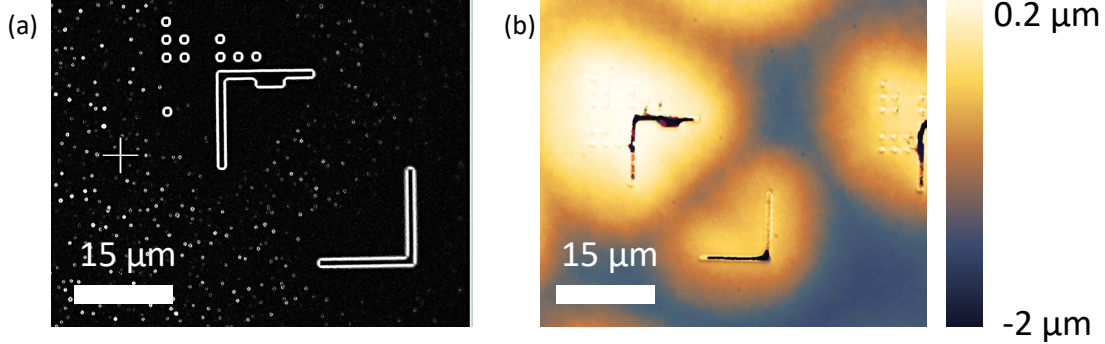


Figure 3.5: (a) Dark-field image of surface impurities around the marker region. (b) Distortions on the surface around the marker due to incubation in ethanol solution for 12 hrs.

### 3.5 The KOH etch method

In order to circumvent the limitations posed by the nLOF process, the KOH process was developed by improvising the method suggested by Nagpal et al. [89]. In contrast to the previous process, we begin with 100 nm  $\text{Si}_3\text{N}_4$  LPCVD on silicon  $\langle 100 \rangle$  wafer. The wafer is coated with a 600 nm positive PR (AZ ECI 3000) using ACS 200 automatic coater (Figure 3.6 step 1). The exposure is performed in contact mode using MA6 Gen3 mask aligner at i-line (365 nm) with a dose of 100  $\text{mJ}/\text{cm}^2$  (Figure 3.6 step 2). A new mask with minor improvements was designed for this process. The illuminated PR is then removed during the development revealing the pattern (Figure 3.6 step 3). The pattern is then etched in to the  $\text{Si}_3\text{N}_4$  underneath by reactive ion etcher (RIE) in presence of  $\text{CHF}_3/\text{SF}_6$  gases (Figure 3.6 step 4). The  $\text{Si}_3\text{N}_4$  is etched at a rate of 80 nm/min however this may vary depending on the size of the sample being etched due to loading effects. After the  $\text{Si}_3\text{N}_4$  is etched the PR is removed and the silicon layer below is revealed at marker positions (Figure 3.6 step 5). The wafer is then immersed in 40% by weight KOH solution at 70 °C to etch silicon with the  $\text{Si}_3\text{N}_4$  acting as a hard mask (Figure 3.6 step 6). As the etch rate of Si in KOH is dependent on the crystalline axis, this leads to anisotropic etching of Si with the  $\langle 100 \rangle$  plane etching almost 200 times faster than  $\langle 111 \rangle$ . The etch rate for  $\langle 100 \rangle$  plane at the above stated conditions is lower than 10  $\mu\text{m}/\text{hour}$  resulting in atomically smooth etch. During the KOH etch the wafer is regularly taken out, washed and inspected under a microscope to determine if the etching is complete. Once finished, the  $\text{Si}_3\text{N}_4$  layer is removed by immersing the wafer in 49% hydrofluoric (HF) acid bath for 10 minutes at room temperature (Figure 3.6 step 7). Next, the wafer is treated with oxygen plasma for 60 seconds to form the native oxide on the Si surface. This is crucial, since in the absence of native oxide the Si binds tightly to Au film and stripping would not be possible. The Au layer is then deposited on the patterned substrates with similar conditions as for the nLOF process. Diced glass chips are then attached to the Au surface after dispensing UV hardening epoxy (NOA 61) on the wafer and curing under a UV lamp for 1 hour

(Figure 3.6 steps 9 and 10). The glass chips can be easily stripped along with patterns created by KOH on Si (Figure 3.6 step 11). As the Au film covers all the etched regions near the markers uniformly, the interaction of epoxy and solvent is only possible far away from the markers at the edges of the sample. Therefore, the KOH method delivers contamination free and extremely smooth Au substrates albeit slightly increasing the number of fabrication steps.

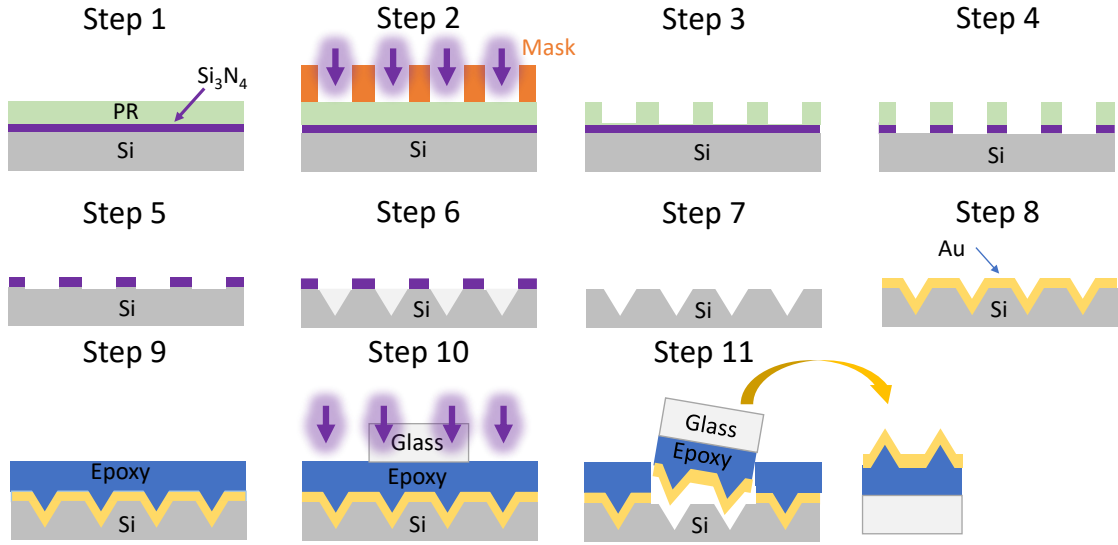


Figure 3.6: Fabrication process to obtain patterned, template stripped substrates by KOH method.

The KOH method can only be used for simple patterns involving straight lines otherwise the KOH etching may deviate from the pattern. This is evident when the mask used for nLOF process is used for the KOH. The marker structure consisting to two intersecting lines (Figure 3.7 a, dashed yellow line) etches towards the center of the marker pattern. This occurs due to the joining of the line as marked by blue circle (Figure 3.7 a). Once the etching is complete, the result is a huge pyramid carved into the Si surface (Figure 3.7 b) with free standing  $\text{Si}_3\text{N}_4$  on the edges. The depth of these structures is approximately  $30\text{ }\mu\text{m}$ . After  $\text{Si}_3\text{N}_4$  removal and Au evaporation (Figure 3.7 c) template stripping is performed to produce micron scale pyramids; larger pyramids with  $30\text{ }\mu\text{m} \times 30\text{ }\mu\text{m}$  square base for the marker region and smaller pyramids ( $1\text{ }\mu\text{m} \times 1\text{ }\mu\text{m}$ ) for the section, row and column labels (Figure 3.7 d). Even though the process did not work as intended, the samples have no contaminations or surface distortions for large or small pyramids. Such structures have been studied for other applications involving SPP such as plasmonic focusing [90] and can therefore be used in other experiments. We were also able to create free standing membranes of  $\text{Si}_3\text{N}_4$  with different patterns which can also be used to study the NPoM with ultrathin mirror and isolated from the bulk (Figure 3.7 e-h).

In order to create markers without forming pyramids a mask was designed where the two marker lines did not intersect. This approach was successful with the formation of the marker structure on template on template stripped Au (Figure 3.8). The marker scheme depicting section, row and column by dots was unchanged, however a few new features were implemented. Lines



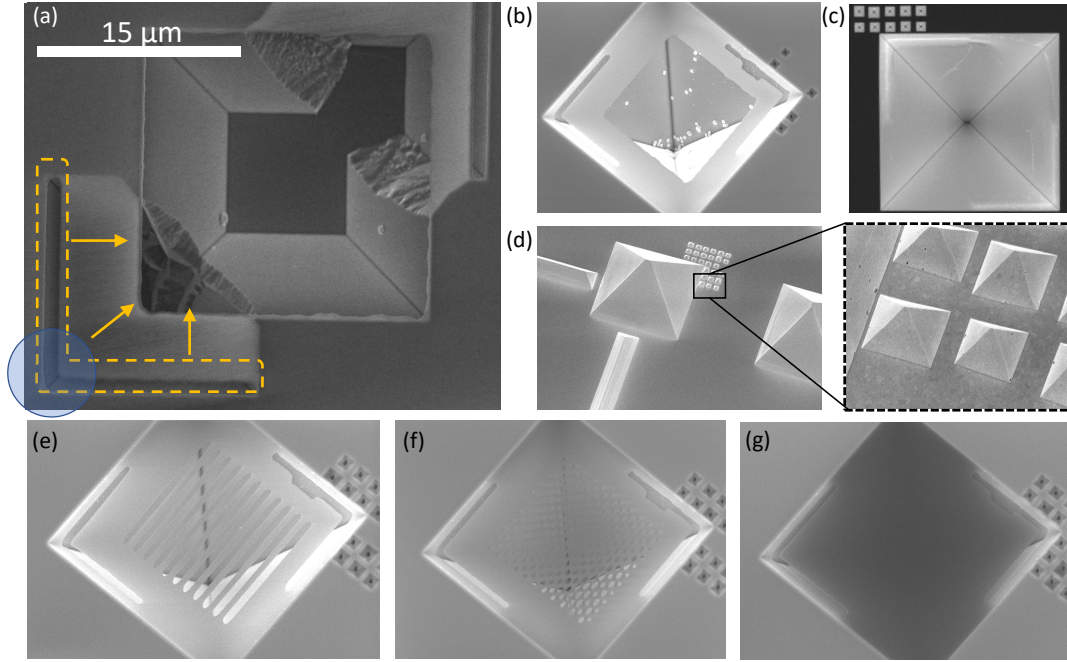


Figure 3.7: **(a)** SEM showing incomplete KOH etching. The marker lines (dashed yellow line) did not etch downwards but rather etched towards the center of the marker as denoted by the yellow arrows. This is due to the intersection of the marker lines. **(b)** After completion, a micro-pyramid emerges in Si with some suspended  $\text{Si}_3\text{N}_4$  on the edges. **(c)** The micro-pyramid revealed after removal of  $\text{Si}_3\text{N}_4$ . **(e-f)** Example of other suspended  $\text{Si}_3\text{N}_4$  membranes with different patterns that were fabricated.

between sections (Figure 3.8 a, red dashed lines) were added to aid in finding a section in optical setups with high magnification objective. In order to locate large-scale fabrication issues; such as contamination on mask, bow of the Si wafer, a number indicating the sample position on the wafer was placed with each section in a sample (Figure 3.8 a, red dashed line). The markers; with perfect rectangular or squares bases that are formed after template stripping, reflect the incoming light and hence appear dark (bright) when inspected with bright (dark) field illumination (Figure 3.8 b, c) in an optical microscope. Inspection with SEM shows the template stripped Au film homogeneously covering the markers without favoring any particular structure (Figure 3.8 d-f).

### 3.6 Method for spacer formation

In order to realize the NPoM structure a uniform gap between the ultraflat substrate and nanoparticle is required. This goal can be achieved in number of different ways depending on the specific spacer material, the required thickness and the intended experiments. Gaps ranging from 1 nm up to a few hundred nanometers can be easily achieved with great accuracy by atomic layer deposition (ALD) [91]. This method fall under the category of chemical vapor deposition (CVD) where the precursors are cycled through a chamber in the presence of the substrate (Figure 3.9

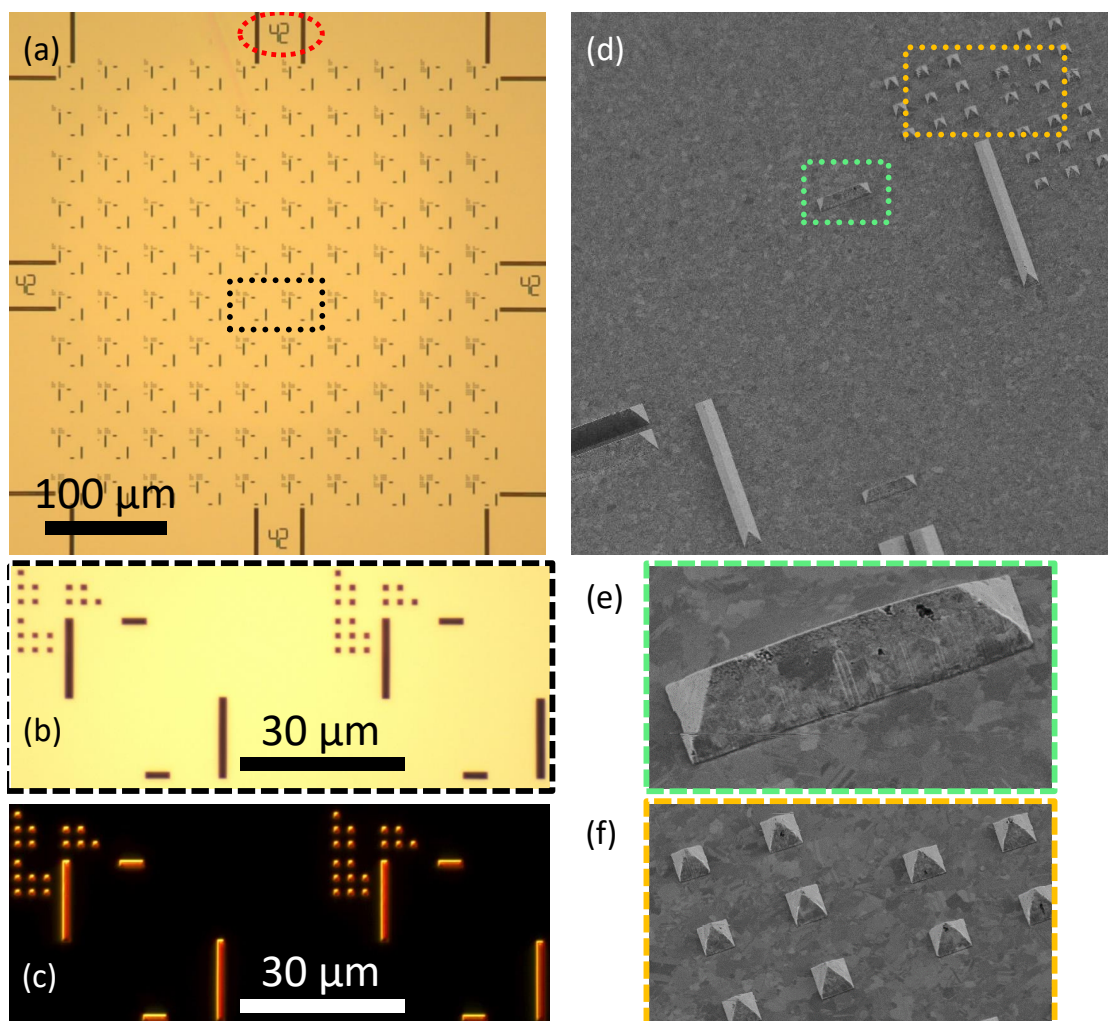


Figure 3.8: (a) A section of markers imaged by a microscope. The red dotted region show the sample number. Lines on the sides of the section lead to other sections. A magnified view of the markers (black dotted region) is shown with BF (b) and DF (c) illumination. SEM image of a marker (d) showing template stripped Au surface with micro-pyramid markers. Close up of some structures (e-f) of the marker shows Au covering all types of structures.

a). By controlling the temperature and pressure in the chamber the precursors react above the substrate forming atomic layers in each half cycle. The excess precursors and the byproducts are purged before the next deposition (Figure 3.9 a). This method however requires exceptional control and optimization of the process parameters and the choice of material that can be deposited is quite limited as well. These factors impose great restriction on the use of ALD. An alternative approach is to stack polycations and polyanions successively on the substrate (Figure 3.9 b). Such stacks can be used to create spacer from 2 nm up to 20 nm by simply stacking alternate layer [92]. While this method is flexible to accommodate a large variety of material, the resulting molecular structure within the stack is irregular. To achieve homogeneous molecular arrangement with gaps ranging from tens of nanometer down to sub 1 nm, 2D material can be

used (Figure 3.9 c). Unfortunately, due to poor control on the number of layers and limitations on lateral dimensions, the properties of such layer may vary significantly from point to point. Alternatively, densely packed and highly oriented molecular layers produced by self-assembly can be used to reach gap sizes similar to those achieved with 2D materials. Unlike the other methods, such layers can be used to place molecules into otherwise inaccessible spaces such as those found in 3D nanostructures [93]. Hence the gap in the NPoM can be created by either coating the mirror or the nanoparticle with molecular monolayers. Owing to the simplicity in preparation, large coverage, high uniformity and good Raman activity, in this thesis we only discuss self-assembled monolayers of benzene derivative molecules such biphenyl-4-thiol (BPT) and biphenyl-4,4'-dithiol (BPDT) on polycrystalline, template stripped Au substrates.

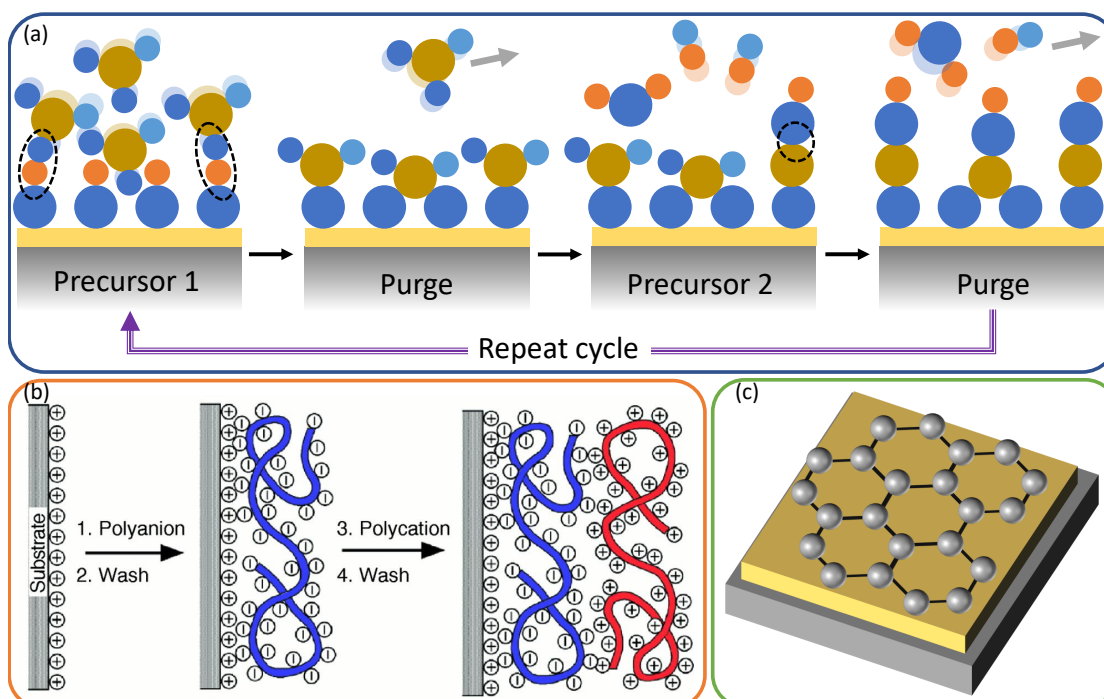


Figure 3.9: **(a)** Schematics of atomic layer deposition (ALD). A substrate with oxidized surface is placed in chamber to react with precursor 1 forming a layer on top. The excess precursor and byproduct are then purged. Precursor 1 is then introduced to react precursor 1 deposited before to complete the formation of the layer. The chamber is purged again the cycle may be repeated. **(b)** Depiction of a layer by layer assembly of polycations and polyanions (Schematic from [92]). **(c)** Gaps down to sub-nm scales can be achieved by using 2D materials as spacers.

### 3.7 Self-assembled monolayers (SAM)

The first organic films were prepared in 1935 by Langmuir and Blodgett using mechanical means to form monolayers of fatty acids on water surface. Assembly of molecular monolayers in absence of external stimuli was first predicted by Bigelow et al. [94] in 1946. However, SAM of organic disulfides on Au was first prepared almost 3 decades later in 1983 by Nuzzo et al. [95].



SAM provided one key advantage over the layers prepared by Langmuir and Blodgett: the former were created spontaneously by immersion of the substrate into solution containing the intended adsorbate species while the latter required mechanical extraction.

Since their discovery, various molecular species have been used to create SAM on numerous substrates, the most common being: organic silane on oxidized surfaces, and aliphatic/ aromatic thiols on noble metals. The most simple, rapid and common method used to produce SAM is by placing the sample in a solution containing the desired molecules (Figure 3.9 a). Parameters such as the concentration of molecules, the solvent of choice, and temperature of solution can be tuned to obtain the required structure [96]. Vapor phase deposition of SAM is also possible under vacuum conditions leading to monolayers free from ambient effects [97]. SAMs have been extensively used to study heat and charge transfer at interfaces [98, 99, 100], catalysis in chemical reactions [101, 102], and tribological properties of surfaces [103]. Organosilicon SAMs such as hexamethyldisilazane (HMDS) are used frequently used in semiconductor foundries to improve photoresist binding to silicon wafers. Sensors can be designed by coupling SAM with electrochemical characterization techniques to bind and detect scarce quantities of analytes with high specificity [104]. SAM are also being studied as potential candidate for their uses in the next generation of low power microcircuits [105].

### 3.8 Kinetics of self-assembly

The adsorption dynamics of SAM, particularly thiols on Au, have been studied with an arsenal of techniques such as scanning tunneling microscopy (STM) [106], cyclic voltammetry (CV) [107], and quartz microbalance [108]. Optical and X ray spectroscopic methods including ellipsometry [109], surface enhanced Raman scattering (SERS) [107], nonlinear optical frequency conversion [110], x-ray photoelectron spectroscopy (XPS) [85], and low energy electron diffraction (LEED) [111], are but a few commonly used ones. The physical and chemical properties of SAM can also be predicted, theoretically, by density function theory (DFT) and molecular dynamics (MD) simulations.

The atomic groups in self-assembling molecules are classified into three main categories with respect to their functionality: head, backbone and tail (Figure 3.10 b). The head group is the part responsible for anchoring the entire molecule on a substrate. Upon contact, the head group initially attaches to the substrate via van der Waal force (Figure 3.10 c). In surface science, this is also known as physisorption. Over time, the atoms in the head group may form chemical bonds with substrate atoms (Figure 3.10 d). This is known as chemisorption [112]. The transition from physisorption to chemisorption is common for most SAM layers however there are a few molecules that can also form SAM by physisorption only. An example of this is methyldisulfide SAM on Au [113]. The adsorption process for thiol (-SH) on Au(111) takes place by the cleavage of the bond between sulfur and hydrogen. The sulfur atom then covalently binds to the Au atom releasing hydrogen (Figure 3.10 e). After the initial assembly is complete, the backbone plays a crucial role in defining the structural properties and molecular interactions. This has been

experimentally observed by comparing desorption of aromatic and aliphatic thiols [114]. The aromatic backbone is also assumed to be more stable due to  $\pi - \pi$  interactions which are absent in aliphatic chains [115]. The tail group are very important for the application of SAM as these can be tailored according to requirement. They serve as custom templates to bind organic [116] and inorganic [117] material. Moreover, it has been shown that the tail group participates alongside the backbone and the head group to define the SAM properties [118]. The tail group can also provide binding site for other molecules which can be used to tune the height by stacking multiple layers (Figure 3.10 f) over long incubation time [119].

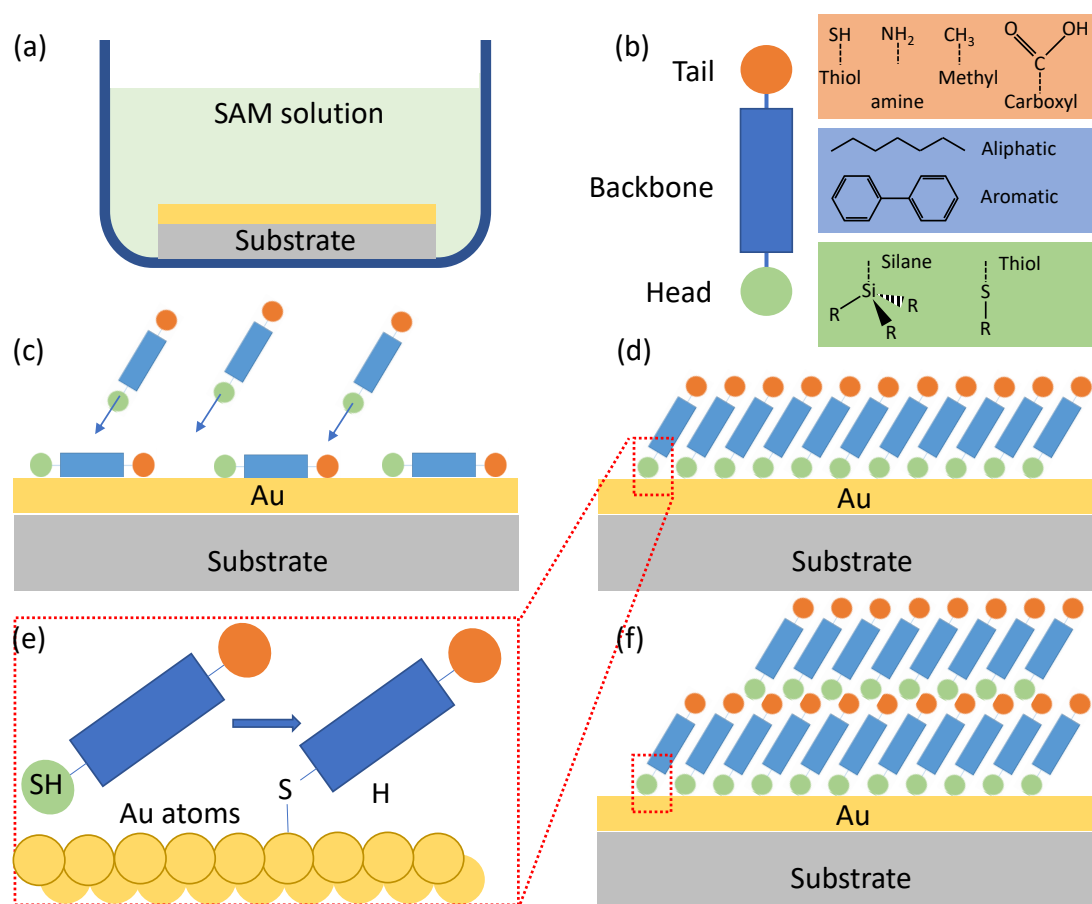


Figure 3.10: (a) Representation of sample incubation in a solution with self-assembling molecules. (b) The functional groups in self-assembling molecules. (c) Physisorption of molecules on substrate surface immediately after immersion into the solution. (d) Well defined monolayer formation after chemisorption. (e) The removal and hydrogen atom and binding of sulfur to gold during chemisorption. (f) Formation of multiple layer of molecules over long incubation times.

The mechanism behind self-assembly is the adsorption of molecular moieties at the surface of a material (particularly metals) in order to decrease the free energy at the interface [120]. During the last few decades, studies of molecular self-assembly by various experimental means and theoretical modelling [113, 121] point towards a two-step process of the SAM formation

[122, 123]. In the first step the molecules approach the surface and are rapidly adsorbed and desorbed, leading to a highly mobile arrangement [122] with thiol molecules adopting a lying-down conformation on the surface (i.e. the molecular axis being almost parallel to substrate). Once a critical concentration of molecules adsorbed on the surface is reached, the nucleation of the well-packed SAM starts locally as small islands growing over time until the saturation point is reached [122]. In the second step the initial phase is slowly re-organized into a densely packed phase with the molecules standing upright (the molecular axis being close to the surface normal) [124]. Although a strong covalent bond is formed between thiol and Au atom, the molecular re-organization continues due to the motion of the thiol-Au ad-atoms [125]. The Au adatom bound to the thiol molecule lifts off the surface and moves along the surface until finding a new position where it rests. This ceaseless surface reconstruction finally results in the formation of Au islands [126].

The two-step process generally describes the formation of thiol-based SAMs on Au. However, the adsorption kinetics and its final SAM structure strongly depend on the surface conditions of the Au substrate and on the preparation protocol. The critical surface conditions affecting SAM ordering are: the size of the crystalline facets, the orientation of the surface facets (expressed as ratio of (111):(100):(110) facets) [127], and the presence of atomic and nanometer-sized (e.g. grain boundaries) surface defects. The main parameters of the preparation protocol affecting SAM ordering are: the solvent [128], the temperature [129], and the incubation time. (The text in this paragraph is extracted from [81].)

### 3.9 Molecular structure within self-assembled monolayers

STM based studies have shown that a large number of heterogeneities could be observed in the SAM, with spatial scales below 50 nm. STM stands out as the microscopy method with the highest possible resolution (down to atomic level) and serves as the main technique for studying molecular ordering on metals and semiconductors [130, 131]. However, STM characterization is doable only over surface areas up to  $1 \mu\text{m}^2$ . To obtain information on the SAM structure over the whole sample surface, STM characterization is often combined with spatially averaged spectroscopic, diffraction, and electrochemical techniques [113]. Thus by understanding the parameters affecting the SAM preparation, it is evident that perfect SAM are not possible. The most ordered SAM structures can be prepared on freshly prepared Au surfaces free of defects and oxides and having mostly large crystalline facets. Even though some guidelines have been established by years of research on model systems [121, 130, 131], there are significant differences between SAMs prepared on single-crystal surfaces used in surface science and the ones prepared on polycrystalline substrates used typically used for plasmonics. In this case the face centered cubic (fcc) structure of gold (Figure 3.11 a) provides mainly Au (111) (Figure 3.11 b), along with Au (100) (Figure 3.11 c) albeit in lower quantities [132].

If the symmetries of the molecules and surface atom are closely related the orientation of the SAM molecules is commonly denoted by Wood's notation [133]. Aromatic thiols on Au (111)

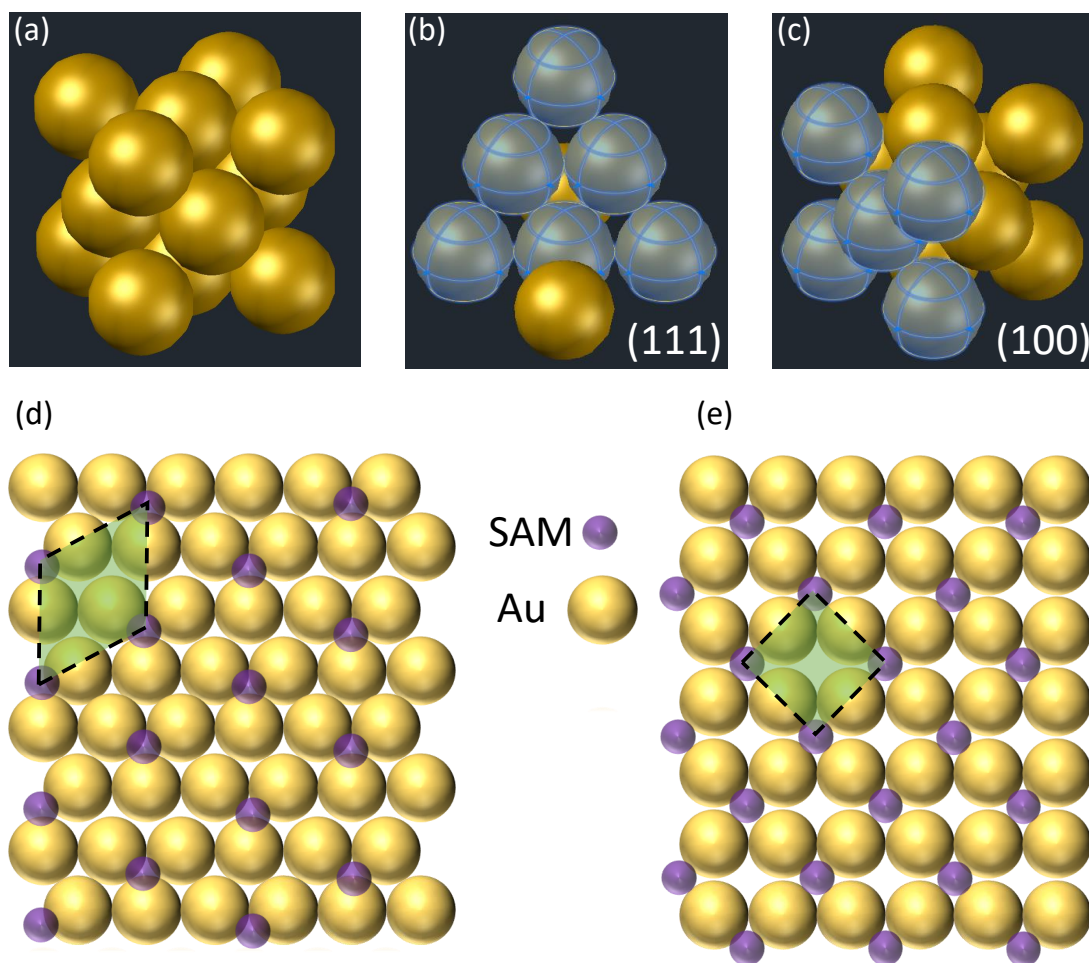


Figure 3.11: (a) Face centered cubic (fcc) structure of Au. The highlighted atoms (blue) mark the (111) (b) and (100) (c) planes. The molecular arrangement of BPT SAM on Au (111) (d) and Au (100) (e).

prefer to arrange in a closely packed ( $(\sqrt{3} \times \sqrt{3})R30^\circ$ ) scheme [134] (Figure 3.11 d). Switching from single crystal surfaces to polycrystalline ones leads to the formation of various SAM phases on facets of different crystalline orientations and around surface defects. In contrast to molecular on Au (111), the arrangement on Au (100) is significantly distinct (Figure 3.11 e). Such inhomogeneity in SAM arrangement may lead to a poor quality SAM with high permeability [135]. This issue is most prominent on polycrystalline Au substrates, where each crystalline grain can be considered as a stand-alone sub-micrometer-wide substrate on which SAM formation proceeds independently with respect to the neighboring domains. These spatial heterogeneities in SAM ordering become evident when working with SAM-functionalized samples and devices and if starting with the assumption of having only robust and perfect SAM layers.

### 3.10 Protocol for SAM based NPoM on template stripped Au

Throughout this thesis we commonly use the following method to create SAM on mirror to function as spacers in the NPoM. Freshly stripped, patterned Au sample is placed in an airtight container with 3 mL of thiol solution. The concentration of thiols is kept at 1mM while ethanol is chosen as the solvent. The incubation of sample is performed at room temperature. Either of the two different incubation times, 2 hours and 24 hours, are used to investigate the effects of molecular orientation on the characteristics of corresponding NPoMs. At the end of incubation, the sample is removed from the thiol solution and rinsed multiple times, alternatively with ethanol and deionized (DI) water before drying under a stream of nitrogen. The samples are then immediately used to create NPoM by drop- casting commercially available gold nanospheres (AuNS) and gold nanocubes (AuNC). A 50  $\mu$ L drop of as purchased nanoparticles is slowly pipetted on top of the sample. The drop is then removed after 30 seconds by nitrogen stream, to obtain a good density of nanoparticles on the substrate. The timing in this step is crucial to obtain single, sparsely distributed NPoMs: longer times lead to coverage of the entire sample surface and create aggregates. The time for nanoparticle drop-casting is dependent of the concentration of the nanoparticles in the solution as well as the SAM layer. Once the NPoMs are ready, they are mount on the optical setup and experiments are performed without delay.

### 3.11 Protocol for SAM on Au nanoparticles

SAM coated nanoparticles were also prepared to create NPoMs. Commercially available, 80 diameter AuNS were purchased from BBI Solutions. The AuNS were diluted in by 2 mM sodium citrate solution with 1:1 ratio by volume. The diluted AuNS solution is then mixed with 10 mM of thiol solution and incubated with gentle shaking for 24 hours. Afterwards, the AuNS are thorough washed to remove excess thiol and citrate. This is done by centrifuging the solution at 14000 RPM for 5 minutes to settle the AuNS to the bottom. Visual inspection would show a clear liquid with a small dot at the bottom of the centrifuge tube. The liquid is then carefully removed by a pipette and replaced with the exact volume of DI water. The AuNS are then dispersed by sonication with the solution beginning to show uniform color. This process is repeated 3 times and finally the AuNS are dispersed in DI water. The volume of the DI water can also be tuned to achieve specific particle densities. The functionalized AuNS are placed above patterned, template stripped Au samples by the drop-casting method described above. However, in this case the AuNS are left for 5 minutes above the mirror surface before washed the sample with DI water and dried with nitrogen. These samples were also characterized without delay to avoid SAM degradation under ambient conditions.



## 4 Experimental methods

In this chapter the experimental setups used to characterize the NPoMs are discussed. An overview of bulk inspection of SAM quality and coverage by cyclic voltammetry (CV) is presented. This is followed by a description of scanning tunneling microscopy (STM) that is common tool used to understand the SAM organization at the nanometer scale. At the end, details of a custom spectroscopy setup, combining various optical techniques that are used to probe the NPoM, are presented.

### 4.1 Electrochemical (EC) characterization

The electrochemical (EC) characterization was performed using a single-compartment, gas-tight EC cell (BM EC model, redox.me) at Max-Planck EPFL Nanolab. Before EC experiments, the cell was cleaned by Caro's acid and boiled three times in DI water. A silver/silver chloride (Ag/AgCl) electrode immersed in 3 M potassium chloride (KCl) was used as the reference electrode, a coiled Au wire was used as a counter electrode. All potentials in the text are referred to the scale versus Ag/AgCl (3 M KCl) reference electrode. The sample surface was used as a working electrode. For EC experiments, the BPT SAM were prepared on 200 nm Au were evaporated on glass substrates with 5 nm Cr as adhesion layer. Template stripped samples are not used to avoid reaction between the epoxy and the electrolyte. Before each experiment, the electrolyte (0.1 M NaOH, 8 mL) and the assembled, gas-tight cell were purged with nitrogen for at least 20 minutes. Gas inlet was then lifted to the gas compartment above the electrolyte. Nitrogen was purged in the gas compartment during EC characterization experiments. Electrochemical measurements were performed using VSP-300 (BioLogic) potentiostat. Thiol reductive electrodesorption was performed by scanning the potentials from open circuit potential to -1.2 V versus Ag/AgCl (3 M KCl) at a scan speed of 50 mV/s in 0.1 M nitrogen-saturated NaOH. (The text in this paragraph is extracted from [81].)



### 4.2 Scanning tunneling microscopy (STM)

Scanning tunneling microscopy (STM) experiments were performed using MS10 STM (Bruker) coupled with NanoScope Controller V (Bruker) and NanoScope software version 8.15 (Figure 4.1), at Max-Planck EPFL Nanolab. During measurements, the STM was placed on a vibration isolating table and covered with a hood to remove spurious effects from the surroundings. The STM measurements were performed in constant current mode. In this configuration, a feedback loop is used to keep the tunneling current constant by adjusting the distance between the tip and the sample. The surface profile can be mapped by measuring the voltage used by the piezo actuator to adjust the tip position. Before each experiment, the sample stage and the top contact were thoroughly cleaned using ethanol and then, dried with nitrogen. Tips were prepared upon mechanically cutting platinum/iridium wire (0.25 mm in diameter, GoodFellow). To avoid any contamination, a new tip was prepared for each experiment. The STM experiments were carried out within two hours of the sample preparation. BPT SAM sample prepared with 24 hour incubation was first characterized in air after which 2  $\mu\text{L}$  of nonanoic acid was added to the center of the sample surface to facilitate high-resolution STM imaging. Both, STM images obtained at the air/solid and at the nonanoic acid/solid interface show no significant differences in SAM structures. STM images were analyzed using WSxM software [136]. (The text in this paragraph is extracted from [81].)

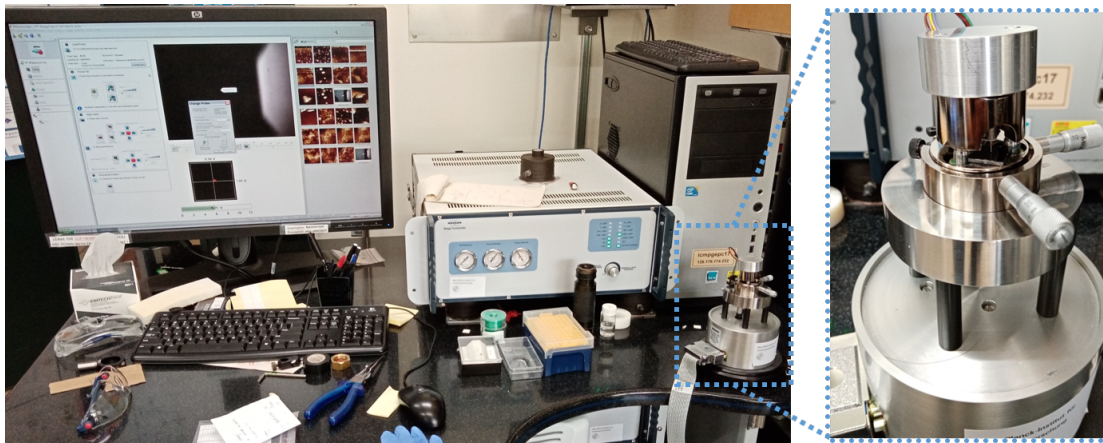


Figure 4.1: Scanning tunneling microscope at Max-Planck EPFL Nanolab. A magnified view of the STM scanner.

### 4.3 Optical spectroscopy setup

The optical setup consists of a confocal microscope that was built entirely from scratch to allow easy combination of different spectroscopy techniques such as multi-wavelength Raman scattering, polarized elastic scattering, photoluminescence and absorption spectroscopy. The setup can also be used as a conventional bright-field microscope. Since most of the components in the setup are mounted on actuators, the transition from one technique to the other can be



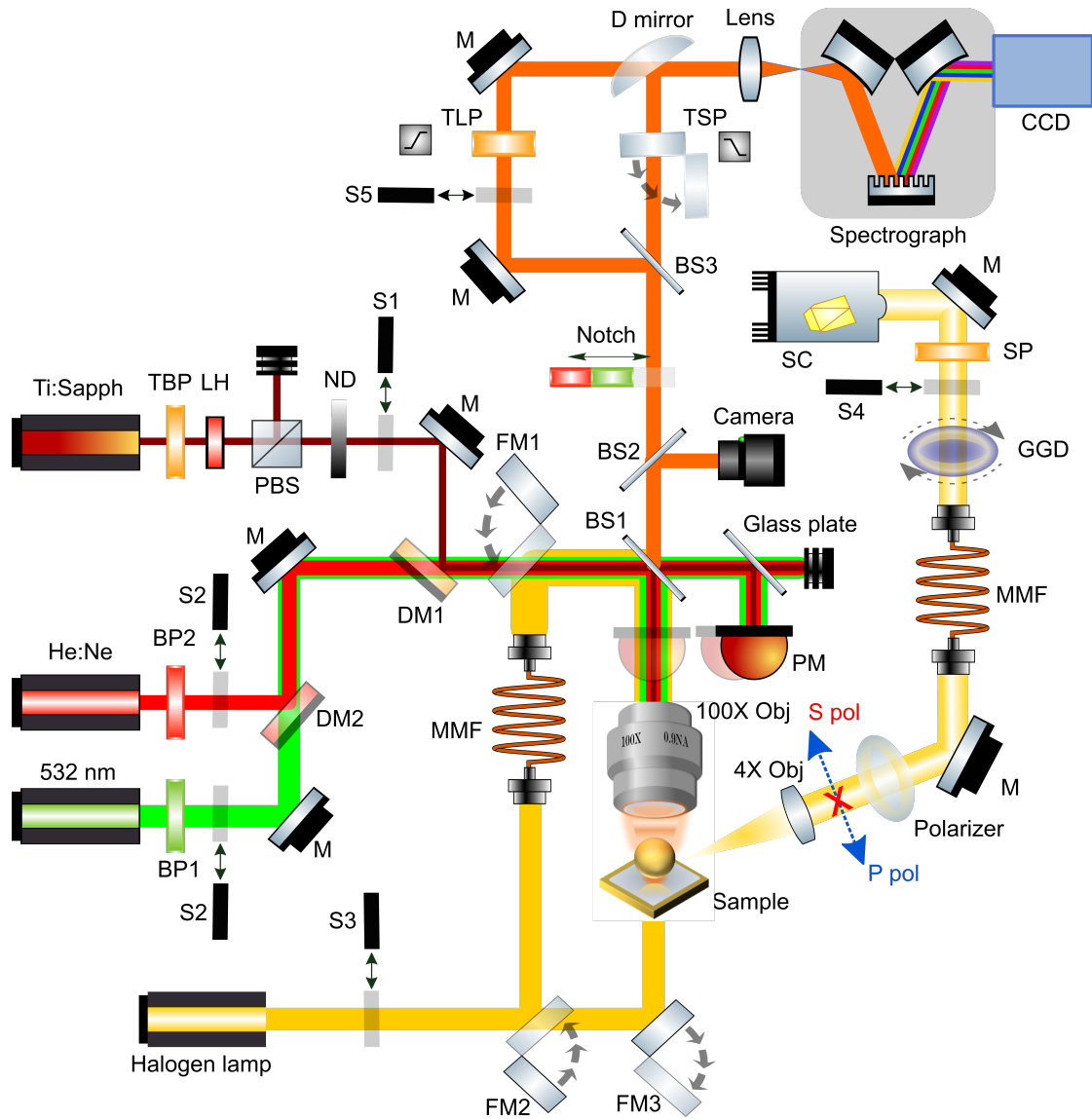


Figure 4.2: Schematic of the optical setup used for Raman and scattering spectroscopy.

performed remotely without interaction with the optical table. This gives complete freedom in designing complex measurement sequences and greatly enhances the stability of the setup allowing longer measurement duration without sample realignment. A simplified schematic of the setup highlighting the important components is presented in Figure 4.2.

Raman scattering spectroscopy is performed by illuminating the sample with continuous wave (CW) Titanium Sapphire (Ti:Sapph) laser from Spectra Physics (Model 3900). The gain media consists of titanium doped sapphire crystal pumped by focusing a frequency doubled diode laser at 532 nm (Spectra Physics Millennia) with 5 W power. Owing to the large bandwidth of the gain media, several modes may exist in the cavity. However, by using a set birefringent filters made of quartz the polarization of a single mode is kept linear while others are converted to elliptical

polarization. These elliptically polarized modes suffer extreme losses during each round trip and hence only the linearly polarized mode can lase. The output mode is adjusted by simply rotating the birefringent filters with a micrometer screw. The wavelength tuning mechanism was automated by connecting the filter rotation screw with a stepper motor and an encoder via belt drive (Figure 4.3 a, belt drive). The stepper and the encoder are connected to the computer and the motion of the stepper motor is then regulated by the encoder value in order to rotate the screw without exceeding the limits. To this end, a LabVIEW based virtual instrument (VI) is used to calibrate the stepper position by with the output wavelength of the Ti:Sapph (Figure 4.3 b). The slightly nonlinear trend in the curve indicates slackness of the belt, which is necessary to move the micrometer screw. With this apparatus, the wavelength of the laser can be tuned anywhere from 710 nm to 850 nm with a resolution of 2 nm.

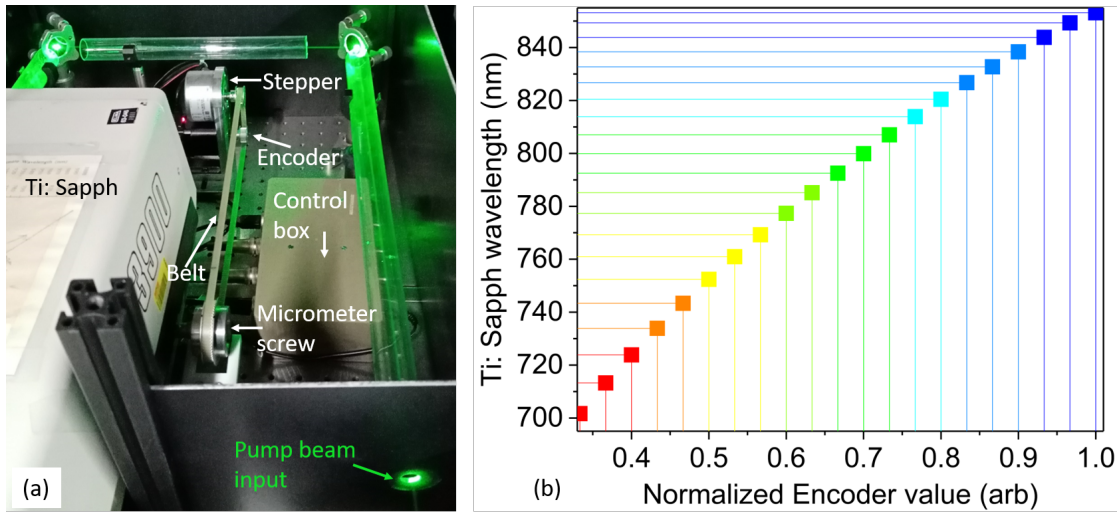


Figure 4.3: **(a)** Belt drive mounted on the micrometer screw. **(b)** Calibration curve for Ti:Sapph wavelength and the position of encoder.

In order to remove any residual fluorescence contaminating the laser spectrum the laser line is filtered using a tunable bandpass filter (TBP) (Figure 4.2). Due to the extensive tuning range of the Ti:Sapph wavelength, we combine two bandpass filters side by side (Figure 4.4 b) to completely cover the entire range. The transmission band of the filter can shift by changing the angle of incidence of light on the filter. For wavelengths below 785 nm and between 785 nm and 850 nm, TBP01-790/12 and TBP01-900/11 filters by Semrock are used respectively. Optical filters are generally evaluated by their optical density (OD) which refers to the amount of light that is removed by the filter at any particular wavelength. The higher the OD the lower the transmission. The transmission curves of both filters, as provided by the vendor, (Figure 4.4 a) show OD values larger than 6 for wavelengths outside the transmission window indicating extremely good performance. Moreover, the 10 nm wide pass bands allows the laser line to pass even with the 2 nm resolution of the wavelength regulation mechanism. In order to change to the transmission window corresponding to a specific laser wavelength the filters are mounted on rotation stages (ELL18/M, ThorLabs). The axis of rotation does not intersect with the laser line but is slightly

shifted, allowing variable angle of incidence (AOI) of the laser on the bandpass filters. Hence, depending on the selected wavelength the appropriate filter is rotated into place with the AOI corresponding to the passband at the select wavelength. During rotation the thickness of the filters (2 mm) results in minor deviations in the optical path length, leading to a shift of the spot when focused by a high numerical aperture (NA) objective. To prevent this, an equally thick glass plate with anti-reflective (AR) coating (49-643, Edmund Optics) is used for compensation. The glass plate is also mounted on a rotation stage (ELL18/M, ThorLabs) and aligned so as to form a mirror image of the filter. In doing so, any changes to optical path length caused by the bandpass filters are rectified by the glass compensator (Figure 4.4 c).

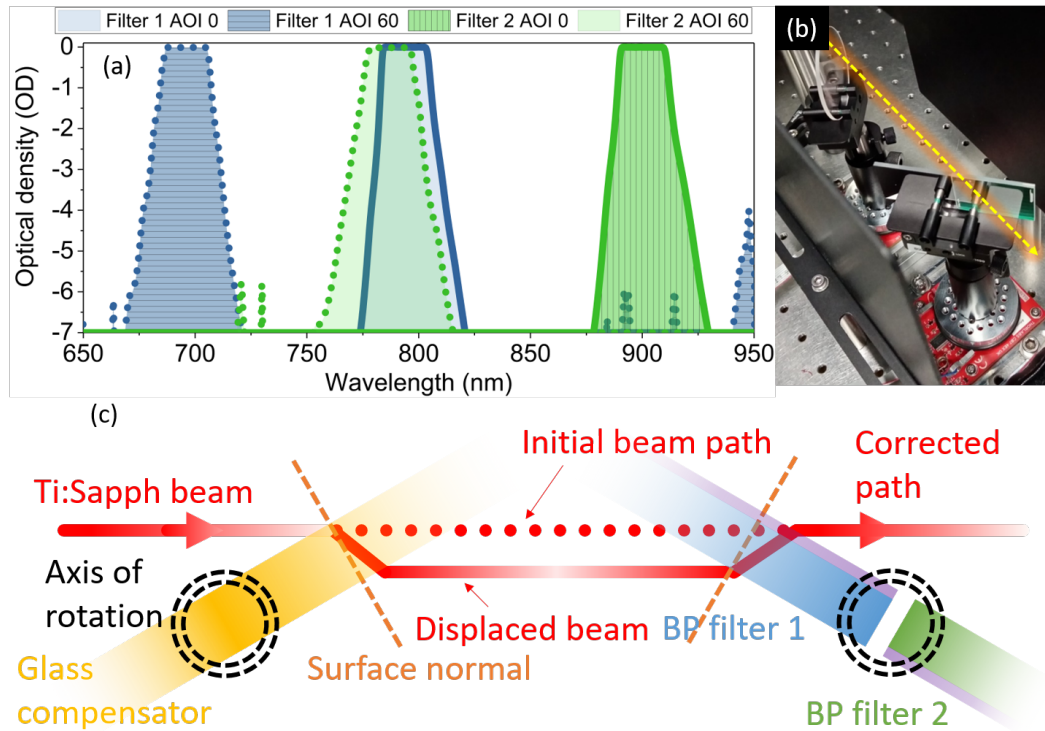


Figure 4.4: (a) The transmission curves of the tunable bandpass (TBP) filters used for cleaning the Ti:Sapph laser line. (b) The glass compensator and the TBP filters mounted on rotation stages. (c) Schematic view of the beam displacement compensation using glass plate of similar thickness.

Afterwards, a lambda-half plate (LH) (AHWP10M-600, ThorLabs) mounted on a rotatable stage (ELL14, ThorLabs) is used to turn the polarization of the laser beam (Figure 4.5 c). A polarizing beam-splitter (PBS) (PBS202, ThorLabs) is placed right after LH which allows p polarization (in plane of the optical table) to pass through but removes the s polarization (Figure 4.5 c). Hence the laser power can be efficiently controlled with the combination of LH and PBS; where the LH turns the polarization to some arbitrary angle and the PBS allows only the p component through while reflecting the s component to a beam block. The advantage of this scheme over the conventional neutral density (ND) filters is apparent by passing the laser beam at different powers through both and recording the optical power for 60 seconds. The Inconel coating used

in most commercially available reflective NDs is not intended for high intensity laser as it does absorb a small portion of the incident power. Exposure to the Ti:Sapph with beam diameter of approximately 1 mm results in heating and oxidation of the Inconel coating. This change in the coating causes a drift in the transmitted laser power during the course of the exposure (Figure 4.5 a) with up to 15% change. Contrary to this, the LH and PBS are not impacted at such laser intensities and the transmitted power shows no change (Figure 4.5 b). The experiments were carried out with Ti:Sapph at 785 nm but the results are similar other wavelengths are well. While the LH and PBS are used to control the Ti:Sapph power in large steps, a continuously variable ND filter (NDL-25C 4, ThorLabs) mounted on a motorized (LTA-HS, Newport) linear motion stage (M-UMR8.25, Newport) is used for finer control of the laser power. This system can therefore be used to regulate Ti:Sapph power over a broad dynamic range: from hundreds of mW down to sub- $\mu$ W, with negligible contribution to power drift. A shutter (S1) is also placed in the beam path to block the Ti:Sapph when needed 4.2.

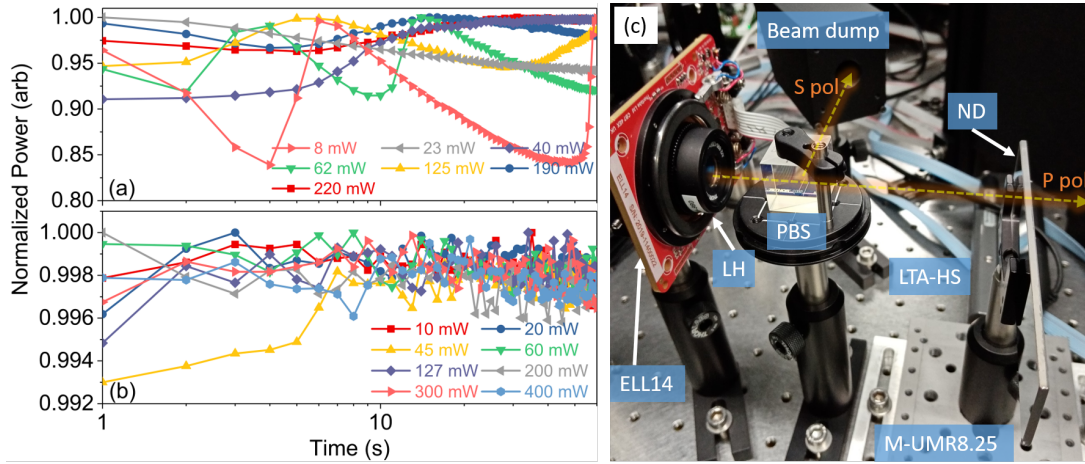


Figure 4.5: **(a)** Power drift of a typical neutral density filter within 60 second of exposure at different laser powers. **(b)** Power stability using a lambda half and a polarizing beamsplitter. **(c)** The power control setup.

The Ti:Sapph beam is then reflected by a dichroic mirror (DM1) (FF697-SDi01-25x36, Semrock) towards a pellicle beamsplitter (BS1) (39-482, Edmund Optics). The DM1 plays an important role in combing the Ti:Sapph with other lasers lines at lower wavelengths: 532 nm and 632 nm, permitting exposure of the sample to single or multiple lasers without moving any components. To obtain 532 nm laser line, a diode pumped solid state (DPSS) laser (CJ532-40, ThorLabs) mounted on a current and temperature regulated laser diode controller (LTC56B, ThorLabs) is used. The diode provides approximately 40 mW with 330 mA input current and a stable temperature at 22.5 °C. In the absence of a closed loop temperature control, large drift in output power may occur (Figure 4.6). The divergent output beam from the diode is collimated using an aspheric lens (C230TMD-A, ThorLabs) with 4.5 mm focal length. In order to improve the spatial beam profile of the collimated 532 nm beam, it is coupled into a single mode fiber (P3-460B-FC-1, ThorLabs) using an adjustable collimation package (CFC8-A, ThorLabs). The fiber is held in

place by clamps in order to prevent fluctuations in the output power. On the other end of the fiber, the beam is coupled out using a reflective parabolic coupler (RC04FC-P01, ThorLabs) in order to obtain an output beam diameter of 4 mm. The 532 nm beam is passed through a bandpass filter (BP1) (FL05532-1, ThorLabs), to clean the laser spectrum, and combined with a 632 nm laser line from a Helium: Neon (He:Ne) laser at a shortpass dichroic mirror (DM2) (DMLP550R, ThorLabs). These two beams can then be overlapped with the Ti:Sapph beam at DM1. A shutter (S2) is mounted in between 532 nm and the He:Ne such that it can either block both the beams or let them pass separately. A flip mirror (FM1) mounted after DM1 can be placed in the beam path to image the sample under bright field illumination from a fiber coupled halogen lamp.

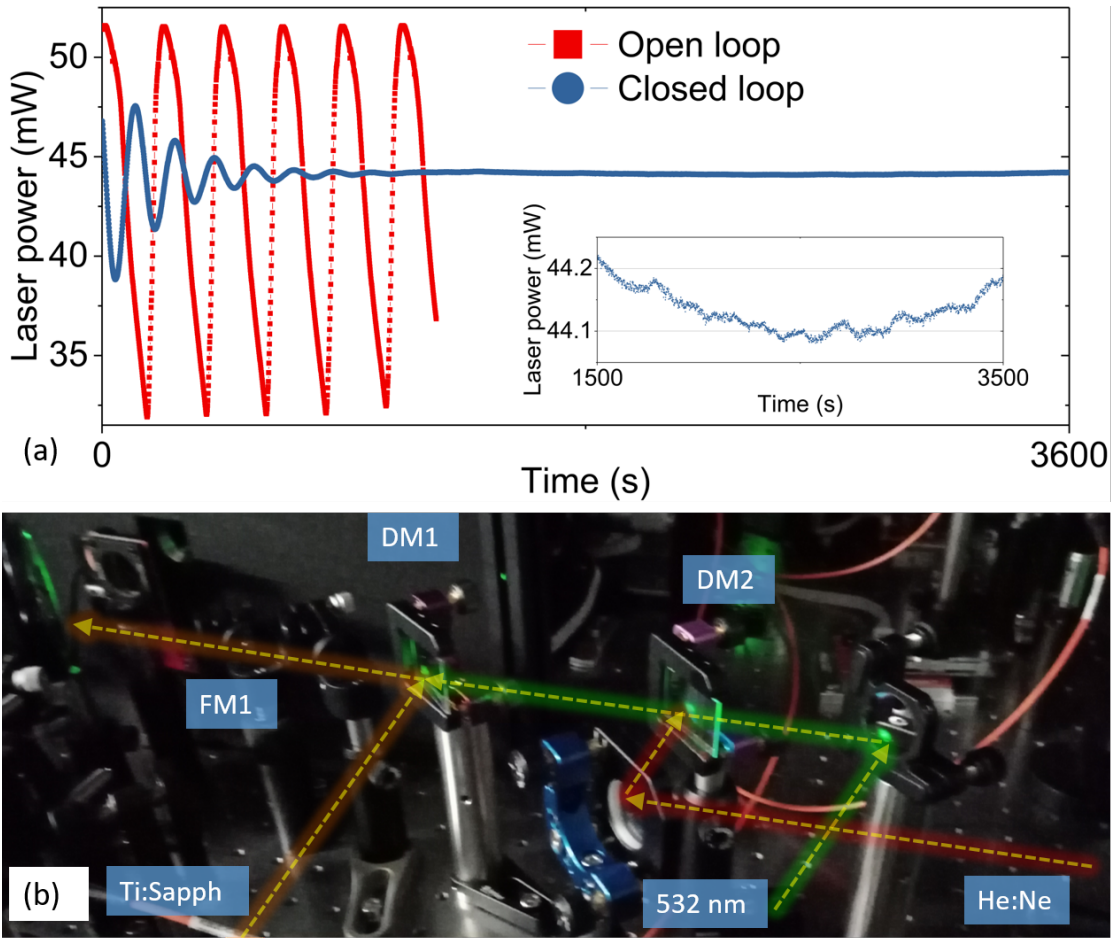


Figure 4.6: **(a)** Stability of 532nm laser diode with and without closed loop temperature regulation. Inset: Extremely low variation with temperature control. **(b)** Combination of Ti:Sapph with other lasers using dichroic mirrors.

Next, the BS1 splits the laser power by approximately 90:10 (transmission: reflection), the lesser of which is used to probe the sample. A pellicle beamsplitter is chosen over plate and cube beamsplitters to avoid ghosting and interference effects in the reflected beam that may lead to a non-symmetric laser spot under strong focusing conditions. Although wedged beamsplitter could



also remedy the above mentioned issues, they also remove a significant portion of the collected signal due to multiple internal reflections. The pellicle beamsplitters are not without demerits, being extremely fragile due to the microscale thickness of the nitrocellulose film. Moreover, the thickness of the film results in the formation of thin film interference effects and hence performing as a static Fabry-Perot resonator. This effect manifests as a wavelength dependent decrease in the reflected laser power (black dashed line Figure 4.7 a) when compared with the incoming laser power (gray region Figure 4.7 a). Each measurement is an average of 100 values of power measured at 1 Hz (inset Figure 4.7 a) and indicates the stability of the laser. The transmitted laser beam is split by a glass plate and the reflected portion is sent to a power meter (PM) (PM16-121, ThorLabs) while the transmitted light is blocked by beam dump (Figure 4.7 b). The PM is mounted on a motorized stage (ELL6, ThorLabs) that can be placed in between the BS1 and the 100X objective blocking the light from reaching the sample (Figure 4.7 c). This configuration is very advantageous as it allows two modes of operation: measurement of the laser power reflected by the BS1 and measurement of the laser power while irradiating the sample. The former is used to normalize the recorded signal by the input power while the latter serves to normalize the signal by any fluctuations of the power that may take place while the sample is being probed by the laser. Two values of the laser power are recorded during an experiment, one at the same rate as the measurement and the other at a constant rate of 0.01 Hz. The simultaneous recording of laser power is extremely beneficial as changes in the laser power are easily adjusted by normalization, and a complex feedback loop to regulate the laser power is not required.

The reflected laser beam from the BS1 can then be focused on the sample via a high NA objective (MPLFLN 100x 0.9NA, Olympus). The high NA allows to capture light from emitters with a collection cone angle of approximately  $60^\circ$ . The objective also has a reasonable transmission for laser wavelength from 532 nm to 850 nm however chromatic aberration leads to difference in the position of focused spot by  $2\text{ }\mu\text{m}$ . This difference can be calibrated by placing a nanoscale emitter in the focal spot and optimizing the position for each laser wavelength. The objective is fixed on a custom holder using a magnetic cage mount (Figure 4.8 a, b). Thus, the objective can be replaced by another objective, with comparable or different parfocal length, by simply replacing with a different magnetic mount. The repeatability of this mounting method is less than  $4\text{ }\mu\text{m}$ , as measured by comparing the image of a structure recorded before and after dismounting and remounting the objective. The transmission of the objective was calculated by recording the laser power before and after the objective using a power meter. The transmission was recorded at different wavelengths (Figure 4.8 c) and a decrease in transmitted power (approx. 20%) was observed as the wavelength transitioned (VIS) from visible to near infrared (NIR). The decrease can be attributed to the fact that this specific objective is not designed for NIR.

The sample is mounted vertically on a close-loop, three axis piezoelectric stage (Nano-3D200, Mad City Labs) for precise positioning. The stage is able to translate  $200\text{ }\mu\text{m}$  in three directions (X, Y in plane of the sample and Z towards or away from the objective) with a, vendor specified, resolution of 1 nm. The stage is connected to the computer via controller (Nano-Drive), which is also responsible for regulating the voltage to the piezo-actuators and calibrating voltage to position. Calibration of the controller is performed before at the start of a new measurement

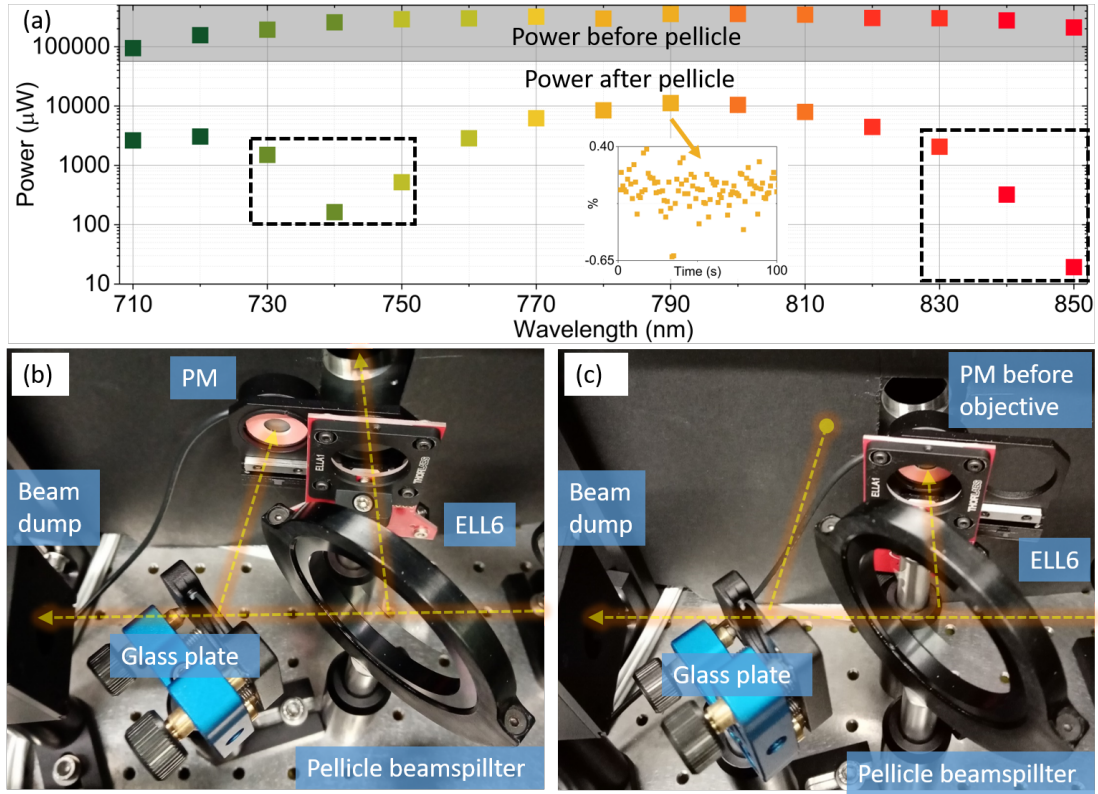


Figure 4.7: **(a)** Ti:Sapph power before and after pellicle beamsplitter. The decrease in power after the beamsplitter at certain wavelengths is due to the thin film interference effects in the pellicle film. Inset shows that each value of power is an average of 100 values. The power meter (PM) mounted on a stage can be moved out of the beam going to the objective **(b)** or can be moved into the beam **(c)**.

session since external factors such as sample mounting and variations in the ambient temperature can lead to deviation from the calibration. In order to increase the dynamic range for positioning the sample, the piezoelectric stage is coupled with an open loop stage, three axis stage (MMP3, Mad City Labs). This allows the sample to be coarsely moved 25 mm in X, Y, and Z direction with resolution of 5  $\mu\text{m}$ . The micro and nano positioners along with the objective holder are placed in an enclosure in order to decrease signal drift over time due to air currents over the optical table. This seemingly simple construct can lead to repeatable NPoM position over the course of several hours.

A charge coupled device (CCD) camera (mvBluefox, Matrix Vision) is placed immediately after BS1 in the path of the collected light, and helps in precise positioning of the sample and also to observe the laser spot (Figure 4.9 a). A glass plate (BS2) is used to reflect almost 10% of light to a 100 mm achromatic lens (AC254-100-B, ThorLabs) that focuses on the camera. The choice of the camera has a huge impact on the image quality, specifically for DF imaging of NPoMs. The camera was chosen after comparing with another commercially available CMOS



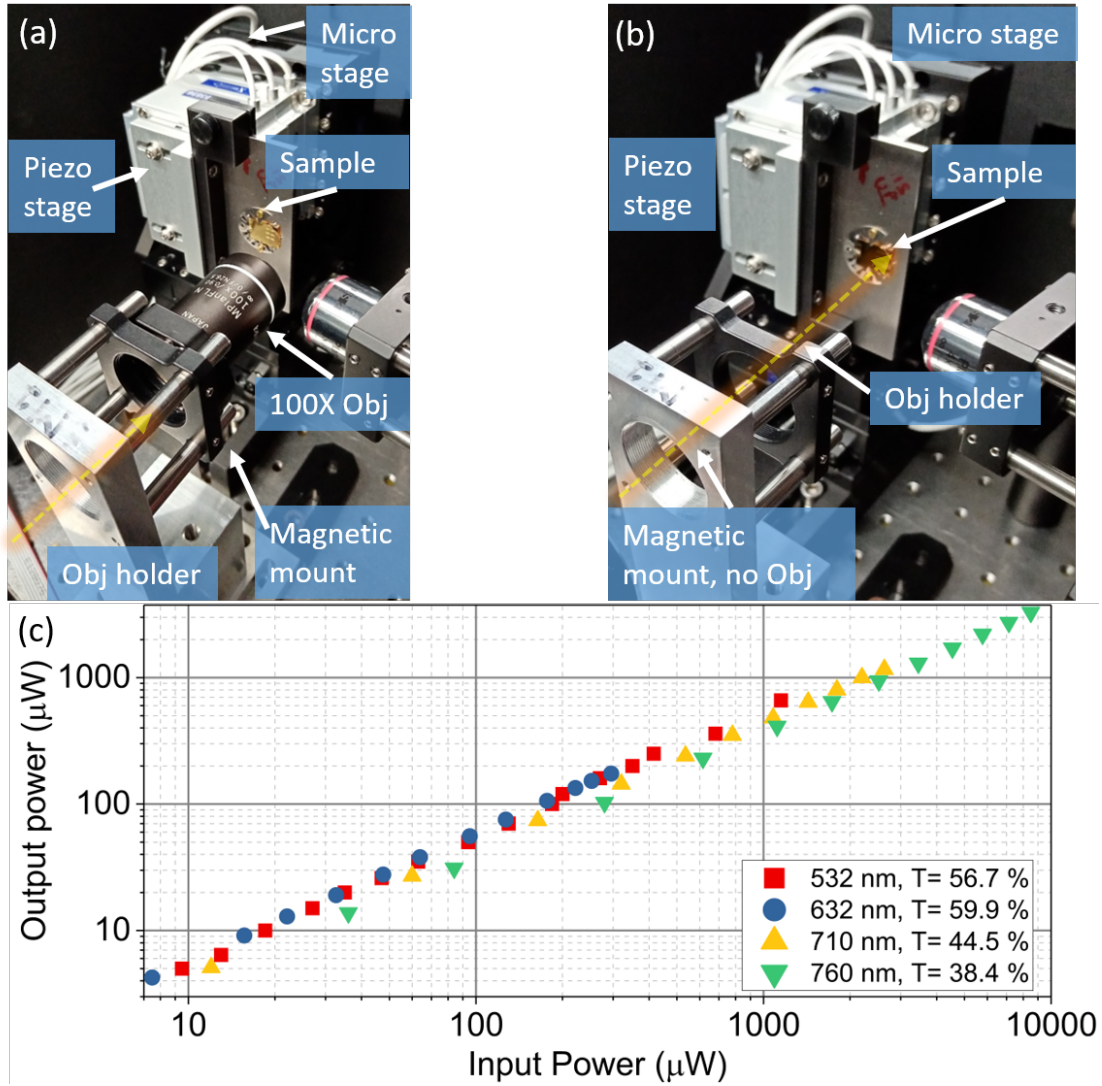


Figure 4.8: (a) A sample mounted in front of the 100X objective on the piezoelectric stage coupled to a micro stage. (b) The 100X objective is removed by simply detaching the magnetic mount. (c) Power recorded before and after the objective at different laser wavelengths.

camera (DCC1645C, ThorLabs) using DF image of a NPoM. The CCD camera shows a nice and clear image of the NPoM (Figure 4.9 b) and while with the CMOS camera the NPoM could be identified and suffered from interference effects (Figure 4.9 c). The position of the camera is also important as placing it too far ( $> 50$  cm) from the objective may lead to clipping of the field of view in the DF imaging mode.

In case of Raman and PL measurements, the laser line needs to be removed from the collected signal. For experiments involving fixed laser wavelengths, such as PL at 532 nm and Raman at 632 nm, notch filters (532 nm: NF533-17, 632 nm: NF633-25 ThorLabs) are mounted on a movable holder (ELL9, ThorLabs). A single to these notch filters have an OD between 4 and 5

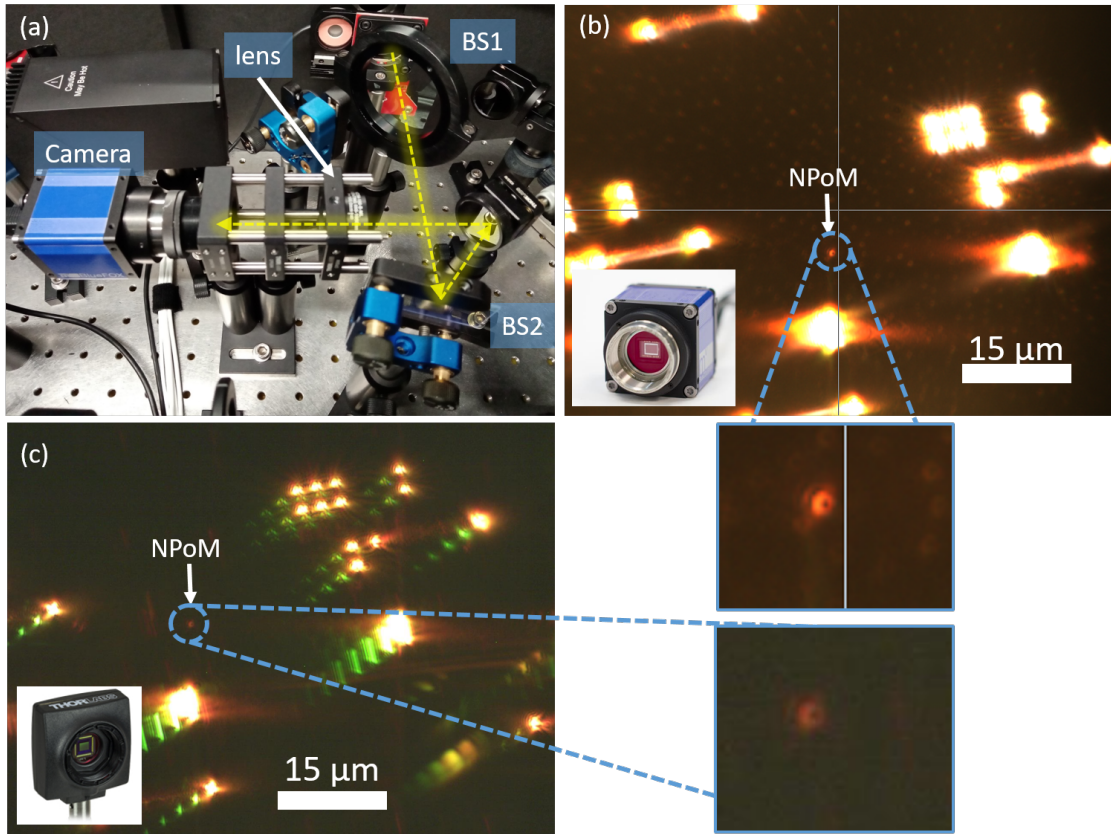


Figure 4.9: (a) The position of the camera in the setup with the yellow line showing the path of the collected signal. Comparison of the mvBluefox (b) and a CMOS camera (c) using DF illumination of patterned, template stripped Au with NPoM. A magnified view of the NPoM with each camera highlights the difference between the two cameras.

(as specified by the vendor) however this is not enough for high power measurements ( $>100 \mu\text{W}$ ). In order to achieve better extinction of the laser line two similar notch filters are stacked together. Either of the notch and can be placed in or moved out of the signal path (Figure 4.10 a). On the other hand, for Raman measurements with Ti:Sapph both the require a special technique in order to remove the laser line. This is due to the fact that for some laser wavelengths of the Ti:Sapph there are no commercially available notch filters. This issue is solved by splitting the collected signal by 90:10 (transmission: reflection) using a plate beamsplitter (BS3) (BSN11R, ThorLabs) and passing separately through tunable longpass (TLP) and short pass (TSP) filters. The transmitted portion (90%) is utilized to retrieve the anti-Stokes component and hence two TSP filters are placed in a manner similar to the TBP filters used earlier for cleaning the Ti:Sapph emission (Figure 4.10 b, blue glow). However, in this case similar shortpass filters to improve laser extinction while also compensating for beam displacement replace the glass compensator. For Ti:Sapph wavelength below (above) 785 nm, TSP01-790 (TSP01-887) from Semrock are moved into the beam. Both these filters have an OD of 7 and a transmission bandwidth of approximately 100 nm. The filters are mounted on rotation stages (ELL18/M, ThorLabs) and

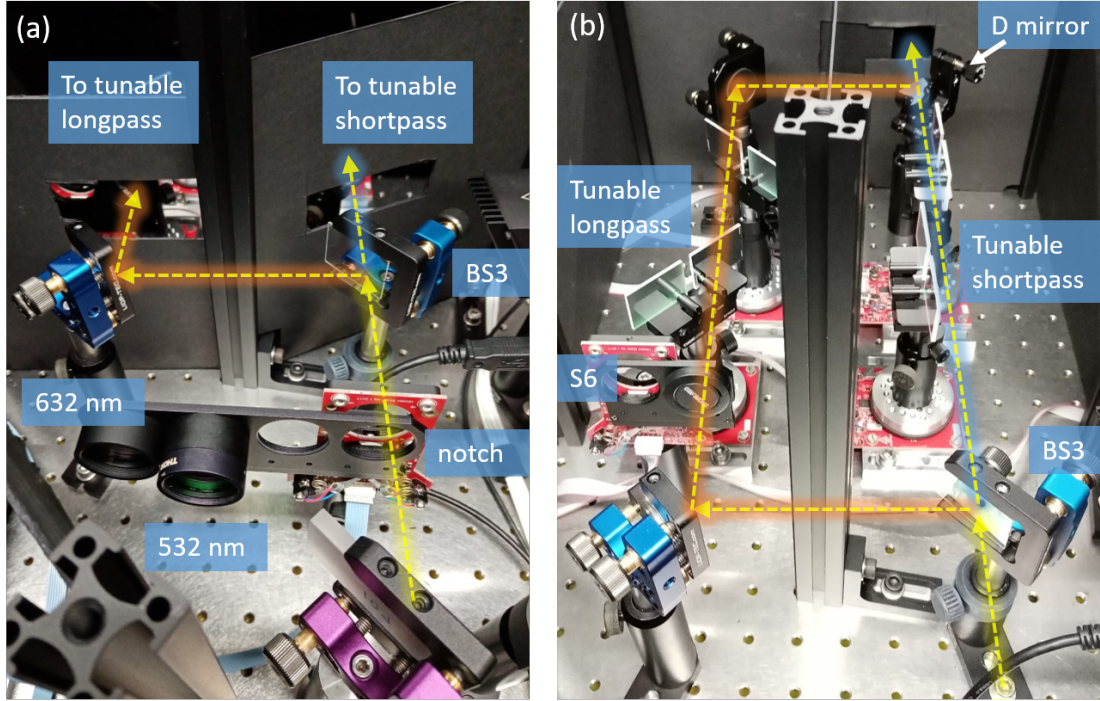


Figure 4.10: **(a)** The notch filters used to remove fixed laser wavelengths such as 532 nm and 632 nm. Each of these filters can be translated into the beam path (yellow line) when required. **(b)** The beam is then split by BS3 into 90 (blue), 10 (red) beams to pass through tunable shortpass (TSP) and longpass (TLP) filters to extract anti-Stokes and Stokes signals respectively. The anti-Stokes and the Stokes beam are finally combined at the D mirror.

are usually adjusted extremely close to the Ti:Sapph wavelength providing access to Raman shifts ranging from  $450 \text{ cm}^{-1}$  up to  $2000 \text{ cm}^{-1}$ . The signal reflected by BS3 (Figure 4.10 b, red glow) is similarly used to extract the Stokes part by using tunable longpass filters TLP01-790 and TLP01-887 from Semrock for laser wavelength below and above 785 nm respectively.

The beams after the longpass and shortpass are spatially aligned along the vertical direction using a D mirror (PFD10-03-P01, ThorLabs), with the anti-Stokes beam being above and parallel to the Stokes beam (Figure 4.11 a). The reason to adjust the anti-Stokes and the Stokes beams to be parallel vertically and not horizontally is to avoid clipping one or both beams by the lens used before the spectrograph (Figure 4.11 b). This lens focuses the incident light on the slit of the spectrograph, hence in case of horizontally parallel beams this would lead to horizontally shifted foci in front of the slit. The slit typically consist of two horizontally sliding blades where only the lateral spacing is controlled via micrometer screw while the height to the opening remains constant. In order to achieve the best resolution the slit is slightly opened hence one of the foci is likely to be blocked by the slit. Alternatively, due to the constant height of the slit, the foci from vertically parallel beams would not be blocked. The spectra are recorded using a spectrograph (Kymera 193i, Andor) with CCD (iDus 416, Andor). The CCD sensor is vacuum sealed and is cooled to  $-60 \text{ }^{\circ}\text{C}$ , using an in-built thermoelectric component, to lower the readout noise and



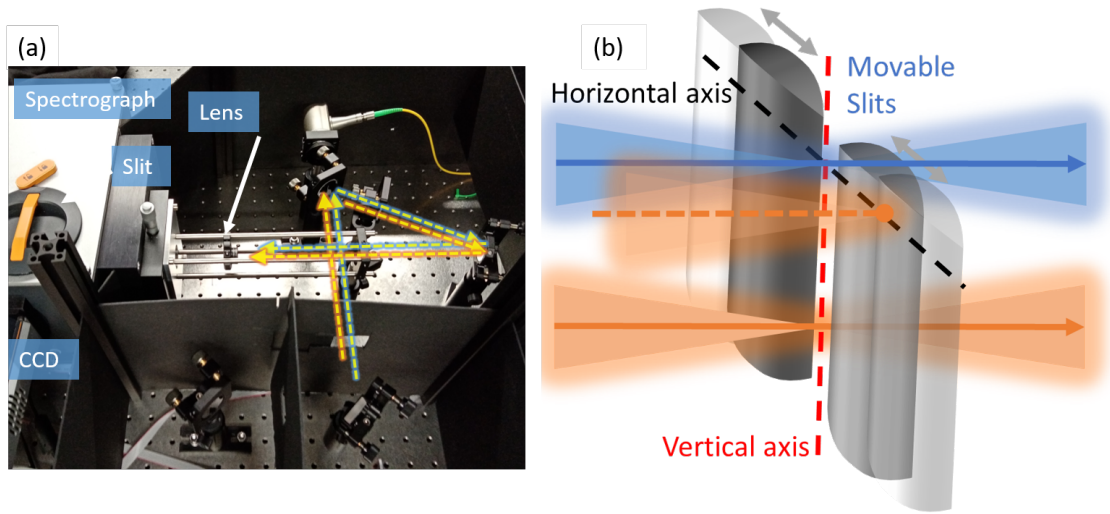


Figure 4.11: **(a)** The beams after combination on the D mirror are reflected towards the spectrograph. **(b)** Schematic view of beams focused by the lens on the slit of the spectrograph. When the anti-Stokes (blue) and the Stokes (red) beams are combined horizontally, one of them may be clipped off by the slit. Therefore, in the setup the beams are combined vertically.

increase the dynamic range. The 16 bit analog to digital converter allows at maximum of  $2^{16} = 65536$  counts in a single acquisition before saturating. A 235 lines per mm grating with 750 nm blaze, centered at 785 nm, is used within the spectrograph to allow acquisition over a broad spectral range. Hence, once centered, the grating needs not to be moved when switching from one technique to another. Once the anti-Stokes and the Stokes beams are aligned on the CCD, the Raman spectra are acquired by vertically binning only 25 pixels while no horizontal binning is performed. The measurements with 532 nm and 632 nm are performed with settings identical to Ti:Sapph.

The elastic scattering spectroscopy (DF) measurements are performed using a supercontinuum (SC) (NKT Photonics SuperK Compact) as a white light source with emission spectrum spanning from 400 nm to 2400 nm. In order to avoid unnecessary heating of the sample, the wavelengths above 1010 nm removed by transmitting the SC beam through a shortpass filter (SP) (FF01-1010/SP-25, Semrock). This leads to a decrease in the power of the SC by approximately 5 times. Contrary to halogen lamps where the spectral components are incoherent, SC sources have a rather finite coherence length similar to lasers. Hence, any form of imaging technique would result in speckles on the image due to interference between the incident and reflected light. Such effects also present as noise in the spectra acquired using a CCD and a spectrometer (Figure 4.13 a). On the other hand, the stability of SC sources over longer periods of time ( $> 24$  hours) is much better than the traditional halogen lamps and so this is the primary reason why SC source was chosen instead of a halogen lamp. In order to be used as an interference free white light source the spatial coherence length of the SC must be decreased. This is accomplished by the method suggested elsewhere [137]. The SC beam is focused by an achromatic lens (AC254-100-AB, ThorLabs), with 100 mm focal length, on 600 grit ground glass diffuser (GGD) (38-788,

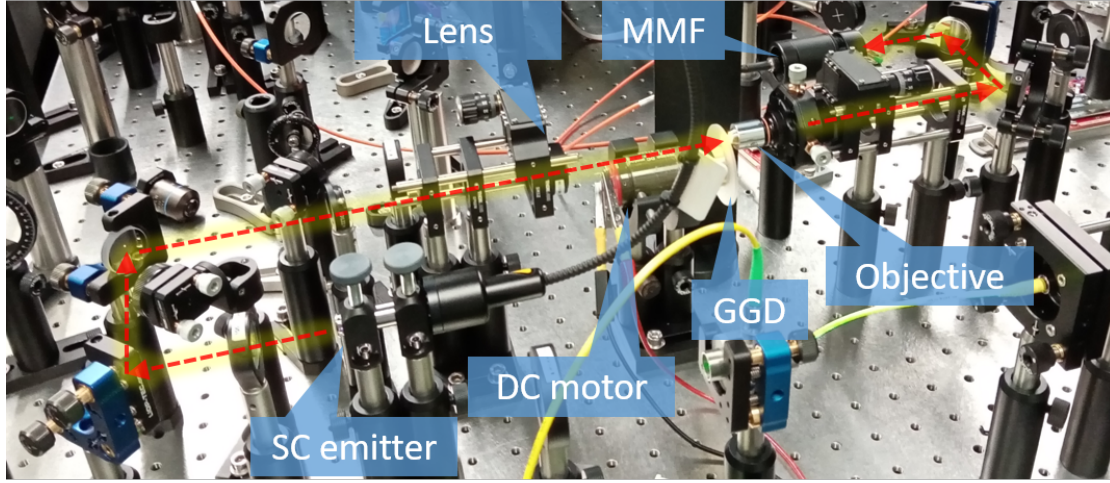


Figure 4.12: Setup to reduce the spatial coherence of supercontinuum source using a ground glass diffuser. The light collected after the diffuser is coupled to a multimode fiber to deliver to the DF illumination head.

Edmund Optics). A finely ground glass diffuser is preferred over a coarse one as the former reflects much less light. The diffuser is mounted on a DC motor and can be rotated with a speed of more than several thousand RPM. Due to the rotation of the GGD, the optical path length of different spectral components within the diffuser keeps changing and hence the spatial coherence of the components is distorted resulting in reduction of speckle noise in the spectrum (Figure 4.13 a). The light transmitted through the diffuser is collected by an objective and coupled into a multimode fiber (MMF) (M15L02, ThorLabs). An image of the above mentioned setup is presented in Figure 4.12 with the beam path highlighted (red dashed arrow)

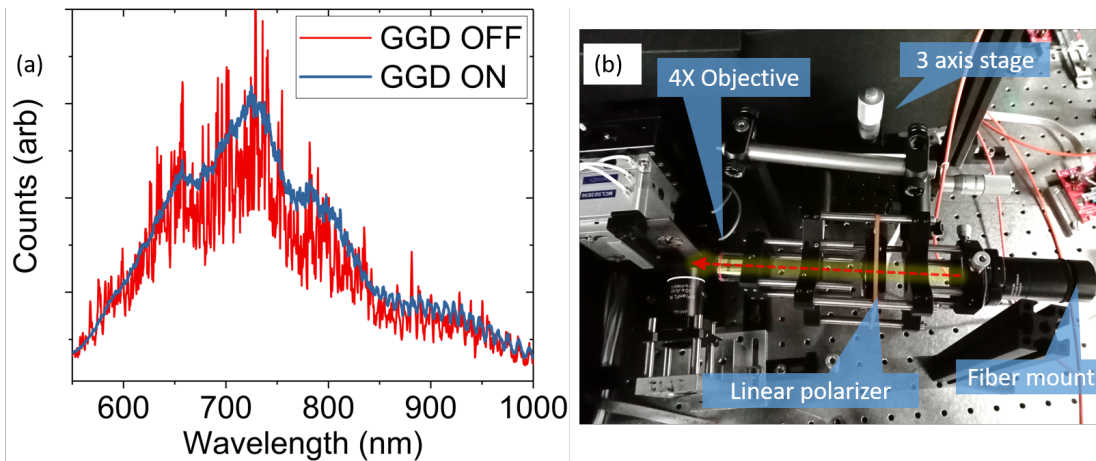


Figure 4.13: (a) The spectra of the supercontinuum with and without the ground glass diffuser. (b) The DF illumination head showing the fiber mount used to collimate the light output from the fiber along with linear polarizer and finally focused by a 4X objective.

At the other end of the fiber, the light is collimated using 40 mm focal length achromatic lens (AC254-40- AB, ThorLabs) in an optical tube. The tube is connected to a magnetic mount with the other end fixed on a cage system. On the cage system the next element is a linear polarizer (LPNIR100, ThorLabs) mounted on a motorized rotation stage (ELL14, ThorLabs) which can be used to control the polarization of light on the sample. In order to enhance the intensity of light on the sample, after the polarizer a secondary objective (PlanN 4x 0.1NA, Olympus) is used to weakly focus the light on the sample. The entire cage assembly is mounted on a three axis stage (PT3/M, ThorLabs) which is aligned at  $82^\circ$  with respect to the normal of the sample surface (Figure 4.13 b). The scattering light is captured by the 100X objective resulting in a DF image on the camera. To acquire the scattering spectra, the fixed and the tunable notch filters are removed from the beam path. The fixed notch filters are removed by simply translating the stage on which the notch filters are mounted. To remove the tunable filters, the TSP are rotated out of the beam (Figure 4.10 b) while a shutter (S5) is used to block the beam reflected by BS3. Blocking the light before TLP has no impact as 90% of the signal passes through the TSP path. In order to acquire the scattered spectra from a small collection region ( $<4 \mu\text{m} \times 4 \mu\text{m}$ ) on the sample the binning region on the CCD is reduced to 2 pixels acting as a virtual spatial filter.

## 4.4 Setup calibration

As it can be noted from the discussion above that a number of optical components are present in the path of the collected signals, each having a distinct transmission and reflection curve. These components may cause significant alteration of the original signal and need to be compensated differently depending on the type of measurement. The Raman measurements, either with Ti:Sapph or He:Ne, need to be normalized by the spectral response function of the optical setup, while for elastic spectroscopy measurements normalization by the SC spectra is required. In the former case, the response is computed by placing a calibrated halogen lamp (SLS201L ThorLabs) in front of the 100X objective without using any refractive elements and recording the spectra from the anti-Stokes (blue) and Stokes (red) paths separately (Figure 4.14 a) after moving the TSP and TLP from the beam path. For each path, 100 spectra are acquired at 1 Hz and averaged to improve the noise level. A spectrum in the absence of light is also acquired to serve as a baseline (yellow region, Figure 4.14 a), and reveals the noise floor of the detector. The spectrum of the halogen lamp (red region, Figure 4.14 b), as provided by vendor, does not have the same x-axis as our spectra and hence interpolation is performed to obtain the source spectrum with a similar wavelength axis (blue region, Figure 4.14 b). The acquired spectra for anti-Stokes and Stokes path (Figure 4.14 a), after baseline subtraction, are divided by the interpolated spectrum of the source (Figure 4.14 b) and normalized by the maximum value of the anti-Stokes spectrum yielding a normalized calibration curve for each path (Figure 4.14 c). The Raman signal calibration curves need to be combined at the Ti:Sapph wavelength with the anti-Stokes part at the lower wavelengths and the Stokes part at the wavelengths higher than the Ti:Sapph. An example of such a combination of the calibration curve assuming laser wavelength of 780 nm is shown in Figure 4.14 d. The gray regions denote the transmission window (100 nm) of the TLP and TSP

filters. This combined calibration curve is then divided from the acquired spectrum to obtain the true spectrum. To calibrate the spectrum for measurements with 532 nm and He:Ne, the acquired spectra are simply divided by the anti-Stokes curve. This configuration with the halogen lamp can also be used to perform transmission measurements on certain samples.

For the DF measurements the calibration of the spectral response of the system was carried out by replacing the sample with a silver mirror. The mirror was tilted at an angle of approximately  $41^\circ$  with respect to the optical axis of the high NA objective. This arrangement reflected the incident white light directly to the high NA objective which is then collected and set to the spectrometer. As mentioned earlier, only the TSP path is used with the filters moved out off the beam while the TLP path is blocked. The intensity of the collected light is controlled by a neutral density filter to avoid saturation of the CCD. The acquisition is performed at 1 Hz and 100 spectra are acquired separately for two specific polarizations of the white light: p (s) when the polarization is in plane (out of plane) with the incident and reflected beam. The binning region over the CCD was set as mentioned earlier. The acquired spectra are averaged to reduce the noise and then smoothed by adjacent averaging over 10 data points. The spectral response is estimated by normalization of the curves by division with the maximum value (Figure 4.15 a). The fringes observed in the s pol curve are due to the thin film interference effects in the pellicle beamsplitter (BS1). The actual DF spectra can be obtained by first adjusting the baseline in the recorded spectra and dividing by the estimated response curve.

To enhance the visibility of the LSPR resonances in the PL spectra of Au based NPoM, the acquired PL spectra are not divided by the anti-Stokes calibration curve but rather by the PL of bulk Au. To this end, 500 spectra are acquired at 1 Hz while illuminating template stripped Au film with approximately 600  $\mu\text{W}$  at 532 nm. Such high power is used to improve the signal to noise ratio (SNR) of the signal. Afterwards, the spectra are averaged to reduce noise and normalized by division with the maximum value (Figure 4.15 b). This curve is not divided by the anti-Stokes response curve and hence contains the PL from bulk Au along with the spectral response. The PL signals acquired from the Au NPoM structures are then divided by the normalized bulk PL. As example consider the spectrum acquired from an NPoM by illuminating it with approximately 10  $\mu\text{W}$  (Figure 4.15 c). After subtracting the background and dividing by the normalized bulk PL, the LSPR mode at approximately 850 nm become very visible along with other modes at lower wavelengths (Figure 4.15 d). The SNR of the PL spectra is poor as a very low laser power is used to avoid damage to the NPoM structure during measurement.

### 4.5 Repeatability

Once the calibration is complete, the wavelength repeatability of the Ti:Sapph system is tested by varying the laser wavelength and recording the spectrum. It is important to characterize any variations in the wavelength tuning as these would effect the calibration of TBP, TLP and TSP filters leading to malfunction of the setup. The Ti:Sapph at 780 nm is focused on a template stripped Au surface and the reflection is sent to the spectrometer. In order to avoid saturation of



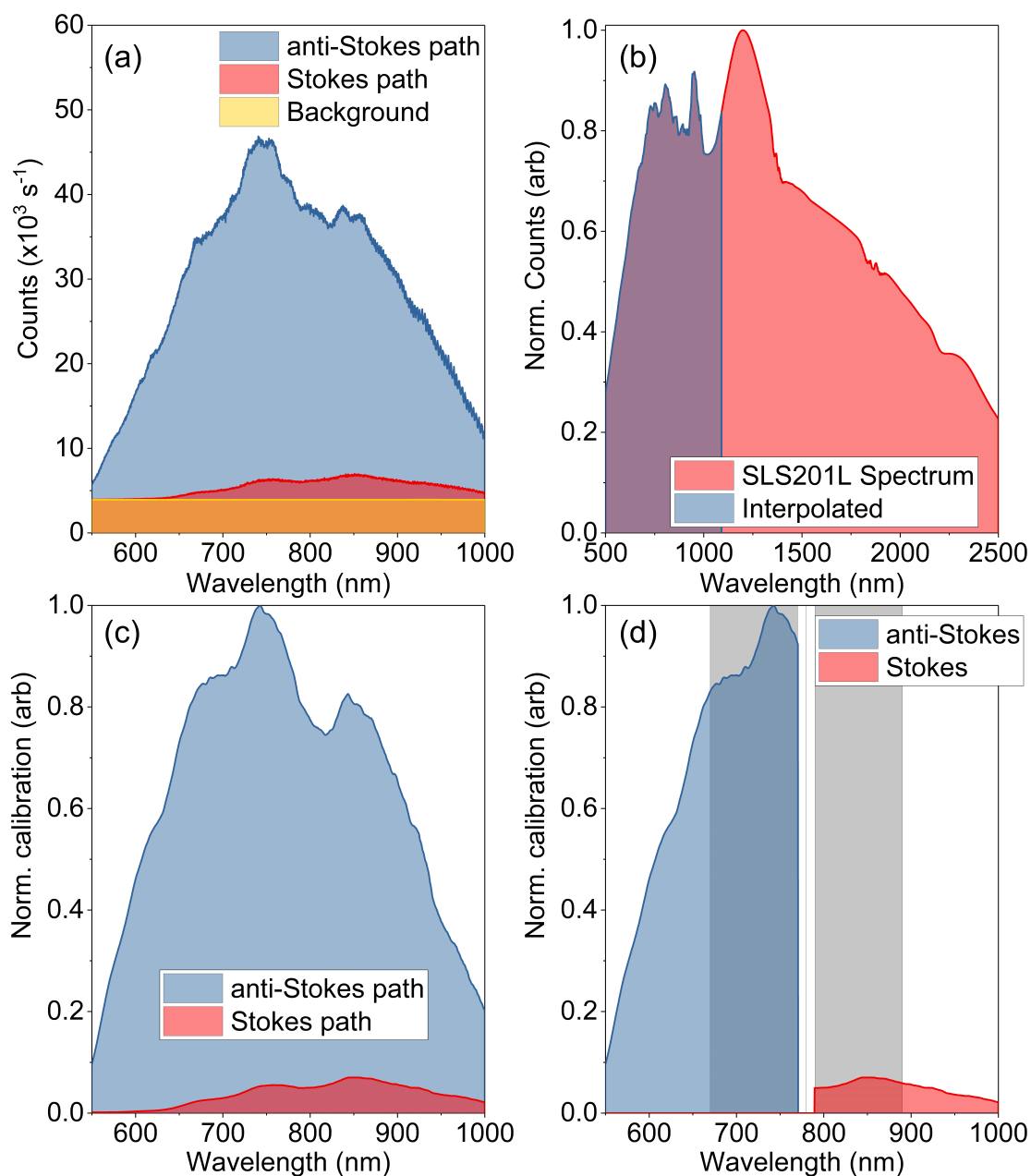


Figure 4.14: **(a)** The spectrum of halogen lamp recorded from anti-Stokes (blue) and Stokes (red) path. **(b)** The source spectrum provided by the vendor (red) and the interpolated curve (blue) used for normalization. **(c)** Response spectrum of the anti Stokes and Stokes paths normalized by anti-Stokes maxima. **(d)** Example of combining anti-Stokes and Stokes response curve assuming laser at 780 nm. Gray region mark the transmission bandwidth of the tunable longpass and short pass filters.

the CCD, the TSP path is block and only the TLP path is used after removing the filters from the beam path. The collected light is also attenuated by placing additional NDs in the collection path. After acquisition of the spectrum at 780 nm the laser is tuned towards shorter wavelength

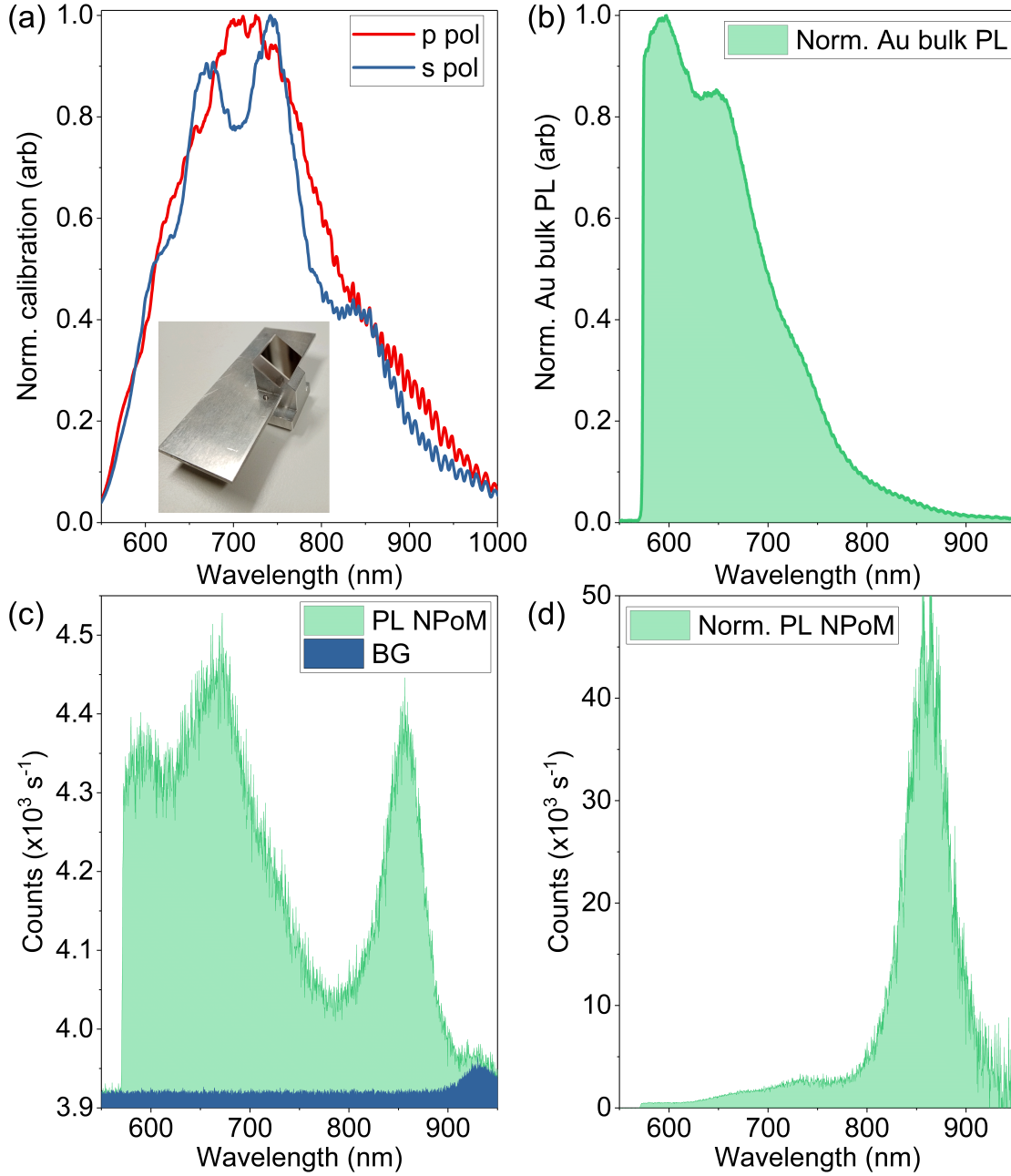


Figure 4.15: **(a)** Normalized response curve for s and p polarized DF illumination. The inset shows a silver mirror mounted on a  $41^\circ$  mount used to record the DF spectrum. **(b)** PL on bulk Au as measured without normalizing the spectral response. **(c)** PL of an Au NPoM structure using  $10 \mu\text{W}$  laser power. **(d)** Normalizing the PL from Au NPoM by dividing by the PL of Au bulk results in a clearer view of the LSPR modes.

in constant steps of 10 nm as indicated by the encoder calibration. Two important observation can be made from Figure 4.16: one, the laser wavelength indicated by the encoder is slightly more than the actual wavelength ( $< 3 \text{ nm}$ ), two, the repeatability of the Ti:Sapph wavelength

depends on tuning direction. The play in the belt drive leads to difference when a wavelength is approached from lower or higher wavelength. In order confirm this effect, repeatability test was performed by tuning the Ti:Sapph from 710 nm to 850 nm and back to 710 nm. The laser spectrum was acquired each time at 780nm and hence by repeating multiple times it is observed that the laser wavelength is very repeatable if it is approached from the same direction (ascending (red) or descending (blue) order) (Figure 4.16 b). Similar measurement was also performed again at 780 nm but by tuning the laser between 770 nm and 790 nm (Figure 4.16 c). The results are similar to those observed earlier and hence the tuning range has no impact of repeatability.

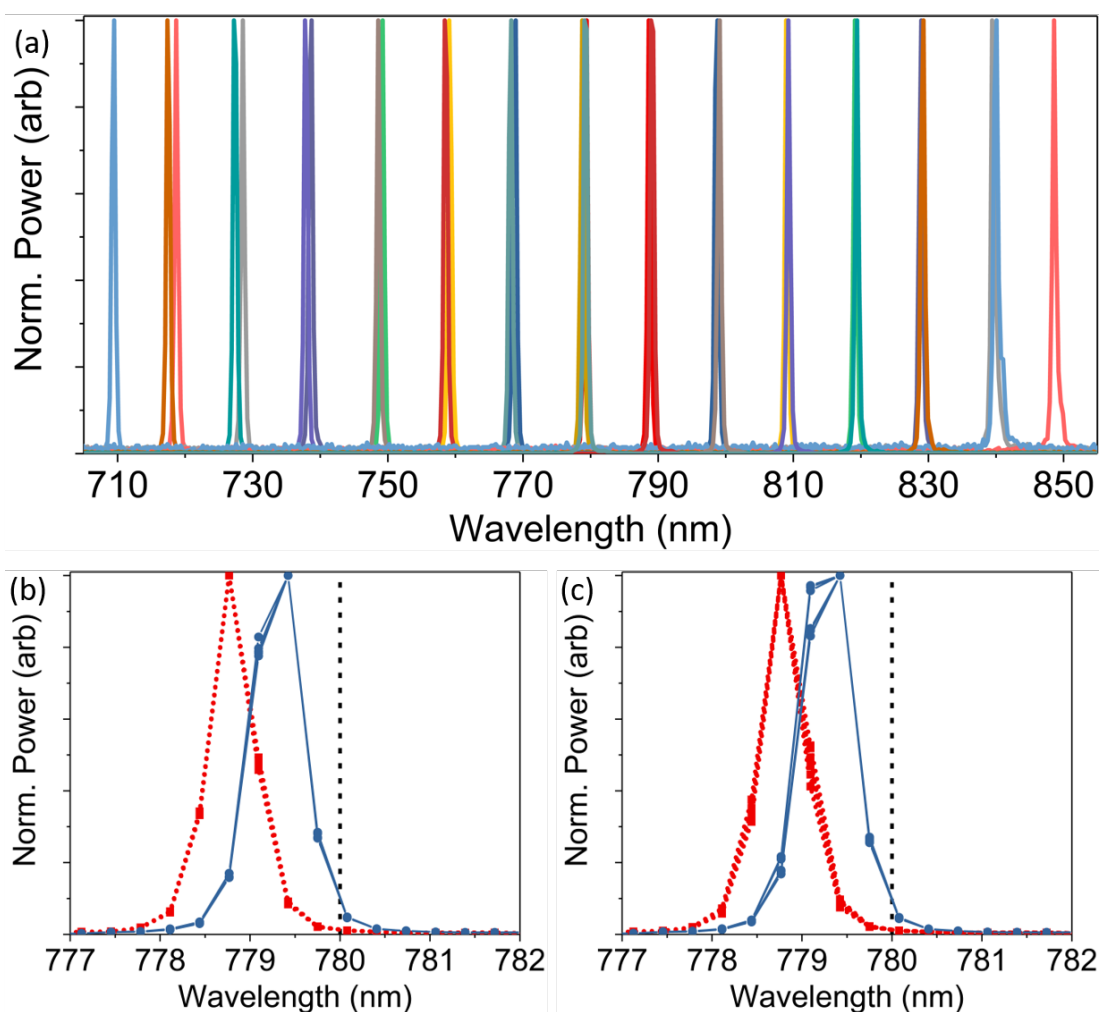


Figure 4.16: **(a)** Shifting the emission of the Ti:Sapph by the belt drive. **b, c)** Repeatability test performed with laser at 780 nm showing that the emission has a slight offset from the encoder value and is dependent if the laser line is approached from lower or higher wavelength.

The repeatability and the drift of the sample stage was investigated using DF measurements on NPoM. Once the sample is mounted on the stage, the setup is left unperturbed for 1 hour to ensure that the temperature within the setup enclosure is stable and the vibrations caused by physical interaction with the stage have been dissipated. Afterwards, the DF signal from an NPoM is

optimized by moving only the piezo stage. Next, a custom built VI is used to record the position of the piezo stage and acquire 10 DF spectra. The stage is then displaced to another position away from the NPoM and a second value for the position is recorded. The displacement can be freely chosen however to mimic experimental settings, all the three axis are displaced by  $3\ \mu\text{m}$ . After waiting 7 minutes, the piezo stage is moved again to the first position and the DF spectra are recorded. This procedure is repeated over the course of several hours with DF measurement after every 7 minutes. Once the experiment is complete, the data is analyzed by observing the changes in the peak height (Figure 4.17 a) and peak position (Figure 4.17 b) of the LSPR modes over time. The results indicate a very steep change in the peak counts but not in peak position suggesting point towards the drift of the stage rather than the change in NPoM. Therefore, typical measurement time are limited to less than 3 hours to keep the effects of position repeatability below 5% of the signal peak (green regions). These measurements can also be performed with Raman spectra however the laser illumination, even at low powers, may results in irreversible changes in the NPoM and is hence not used.

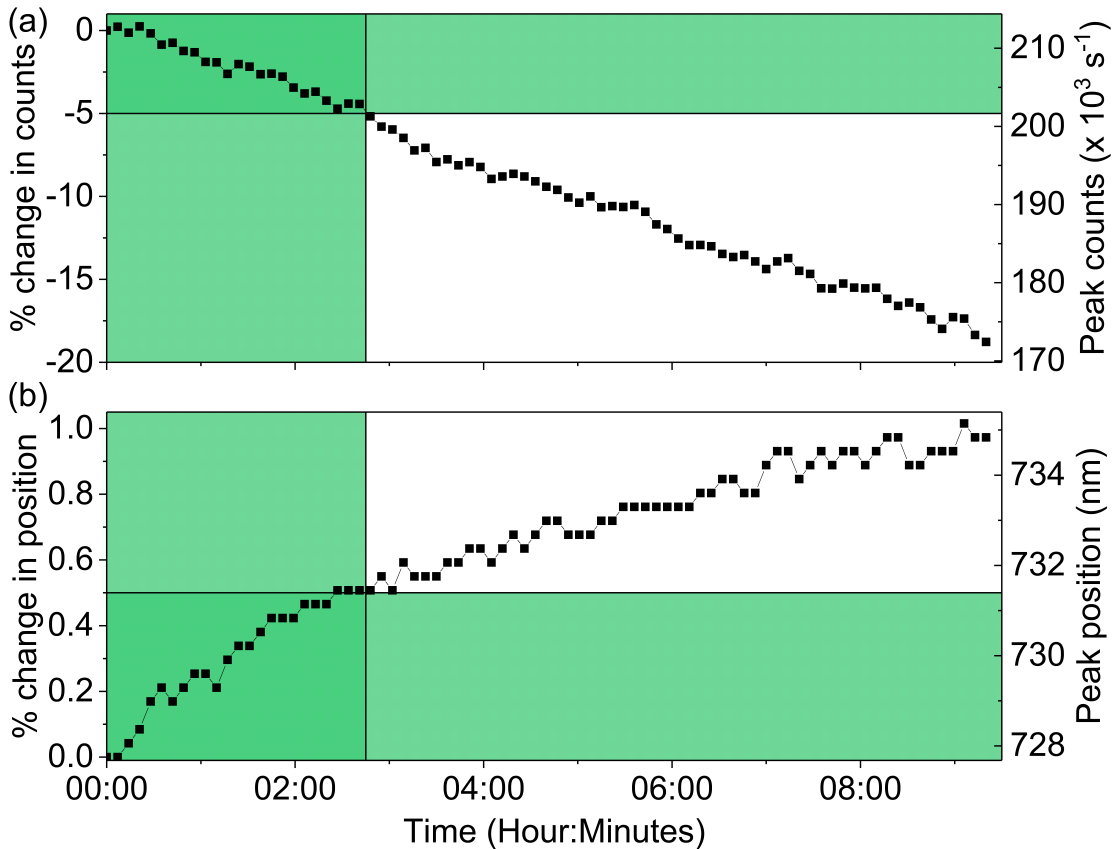


Figure 4.17: Positioning stability of the sample stage measured by the change in peak height (a) and peak position (b) of the DF spectrum over time. The dark green region indicates the time period for which measurements can be performed with 5% change in peak height due to sample drift. For this case, measurement can be performed for almost 3 hours.

The drift of the stage is extremely dependent on the calibration of the stage. In the aforementioned

case, the calibration of the stage was performed before conducting the experiments. Also important is the sample mounting. By mounting the sample slight loose and performing the repeatability test it was observed that the sample moved away from the optimized position in a very short time (20 minutes for 5% loss of signal, 4.18). This is crucial to have an estimate of such parameters, so as to find appropriate means to mitigate these effects on measurements performed with NPoM samples.

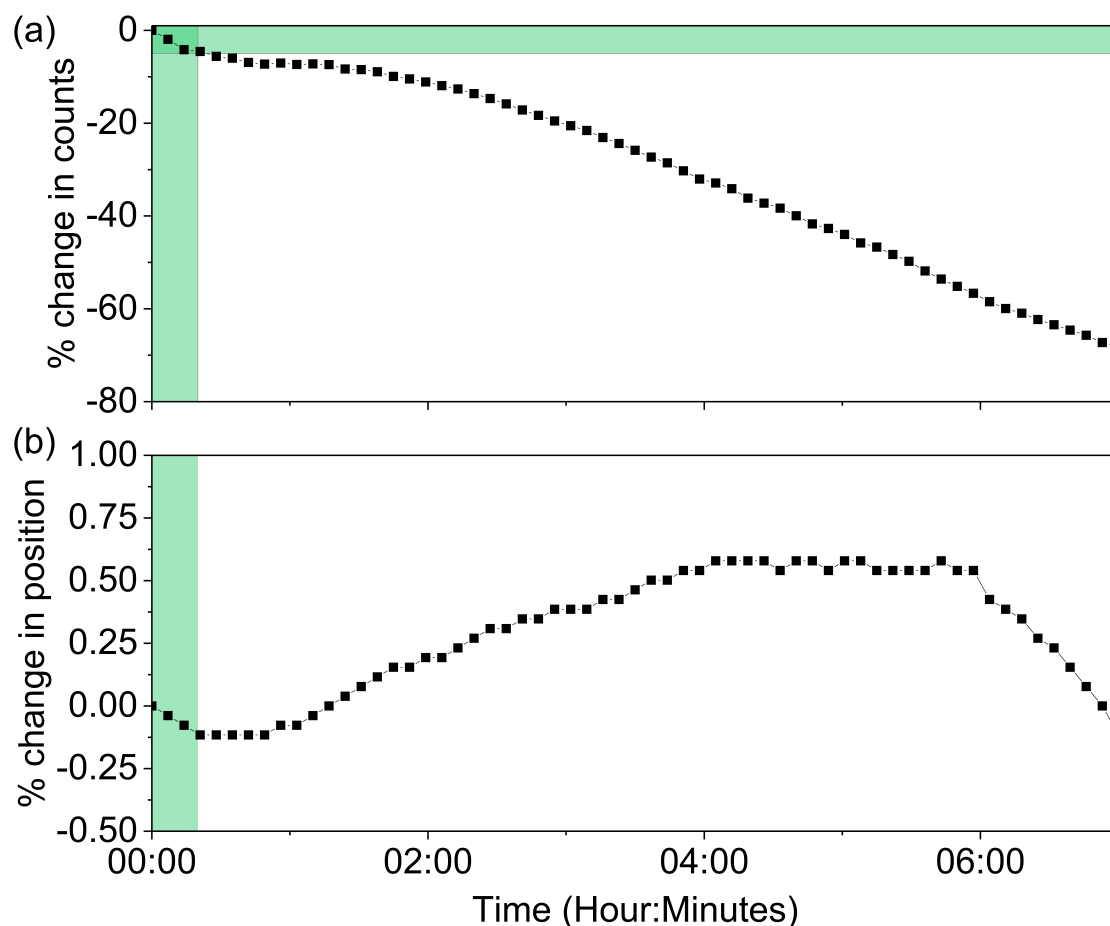


Figure 4.18: Positioning stability of the sample stage measured by the change in peak height (a) and peak position (b) of the DF spectrum over time. The dark green region indicates the time period for which measurements can be performed with 5% change in peak height due to sample drift. As the sample mounting was Imperfect, the peak height decreases steeply. Even still, measurements can be performed for 20 minutes.

## 4.6 Automation

The optical setup described above can be used to perform measurements in an automatic manner. The motivation to automate the setup arises when measurement have to be performed over the course of hours and in some cases days. Moreover, automation also enhances the stability of

## Chapter 4. Experimental methods

the optical setup by minimizing physical interactions with the optical table. Also, automation enables relaxed measurement schedule since all the components can be monitored and controlled remotely. This is achieved by mounting all the key components needed for the different types of measurements on appropriate actuators. The most commonly used actuator in the optical setup are the Elliptec motors (ThorLabs). While these motors are used for different purposes depending on the actuation type (rotation, translation), all of them are connected to a single circuit board (Figure 4.19) and are interfaced with the computer using a single universal serial bus (USB). The motors are assigned distinct addresses and can be individually controlled using a LabVIEW VI that is used to select a particular motor and send the appropriate commands. The commands syntax typically consists of the motor address followed by a string specifying the operation to be performed. The automation of the entire optical is based on LabVIEW as it provides multi-threaded, real-time control over the actuator with exceptional GUI interface.

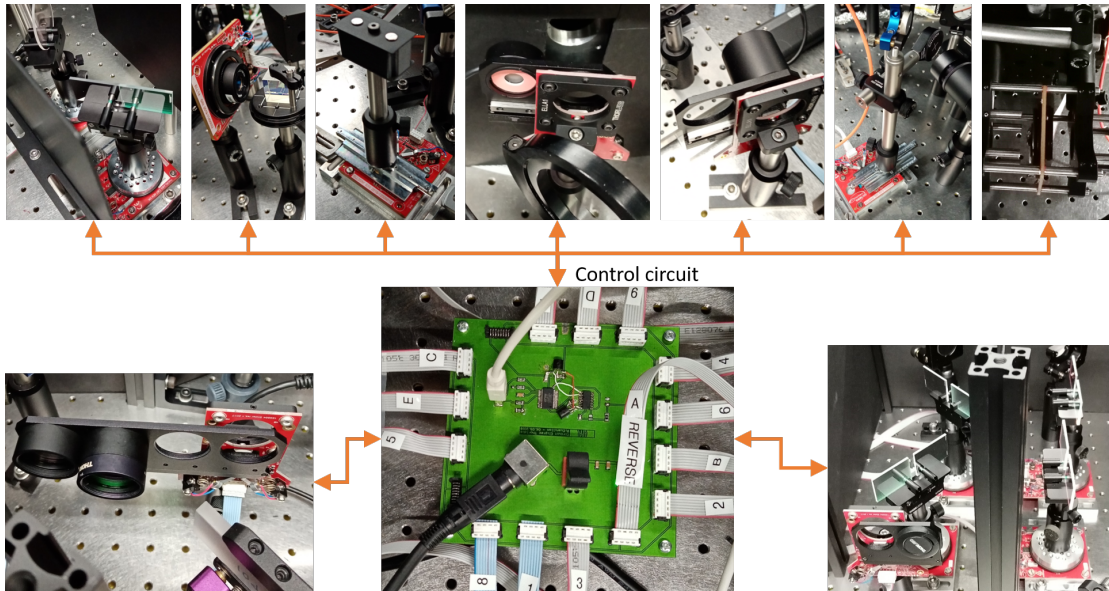


Figure 4.19: An image of the circuit board used to interface the Elliptec motors with the computer.

Separate VI's are designed to control other devices in the setup such as micro and nano-positioners, CCD operations, Ti:Sapph wavelength tuning, image acquisition from the camera, and power measurement with PM. These VIs directly regulate the functions of a physical component in the optical setup and are therefore called base functions or base VIs. The system is designed in a manner which allows to use each of the above described base VI's individually (Figure 4.20 a) or in combination with other VI's by using so called master VI that may simultaneously govern all the base functions (Figure 4.20 b). This program architecture makes the system extremely flexible in terms of usage as new modes of operation can be simply added by designing a new master VIs. One case where such a combination is very valuable is mapping: a point by point acquisition of spectra and projection of the strength of a particular spectral feature in a plane (or even in a volume for 3D mapping). A crude representation of the mapping algorithm using master VI approach is presented in Figure 4.20 c. The colors are representative of the base functionalities

as shown in Figure 4.20 a, b and mark the control flow. The master VI takes the user inputs for the mapping parameter and computes the list of coordinates for a raster scan and with the total number of points. The control is then transferred to the sample positioning VI to move to the first position on the list. Then the laser shutter is opened and the power is recorded using the actuator control VI. The spectral acquisition is performed by the CCD and the laser shutter is closed. The master VI then checks to confirm if this was the last point on the list. If not, then the stage is moved to the next point and the process is repeated. If yes, then the measurement is finished. More complex algorithms employing the base functions in more intricate manner may be developed in order to characterize NPoMs or other samples.

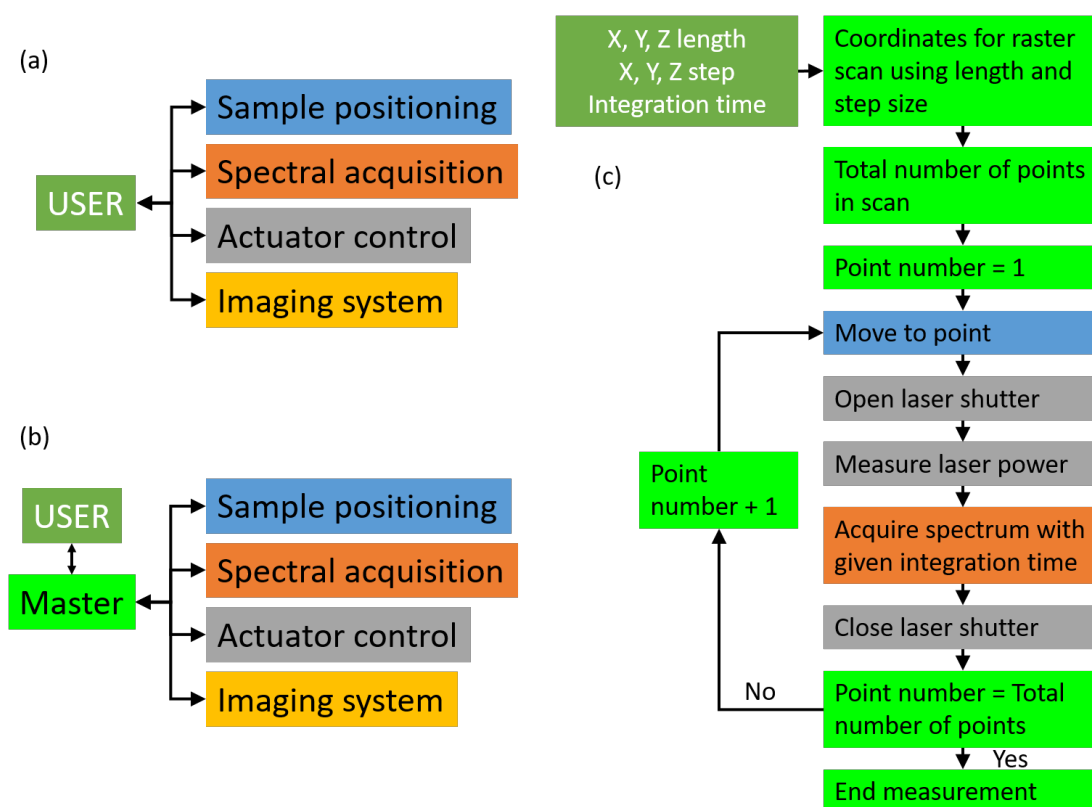


Figure 4.20: **(a)** Direct user interaction with base functions. **(b)** Control of base functions using a master VI. **(c)** Flow chart showing control flow for a mapping algorithm.





## 5 Experiments and Results

In this chapter the Raman measurements on silicon and diamond are discussed along with anti-Stokes/Stokes thermometry. Similar measurements cannot be performed on NPoMs due the change in the plasmonic resonances of the structures during exposure. In order to understand the underlying reason for this instability, the orientation and packing of SAM molecules was evaluated using EC characterization and STM. The instability of the NPoM structures and its dependence on the SAM orientation and nanoparticle shape was also investigated using repeated exposures to constant as well as increasing laser powers. NPoMs prepared with 2 hours of incubation in ethanol solution were found to be more stable than those prepared with 24 hours under similar conditions. Moreover, the nanoparticle shape was found to drastically impact this behavior by changing the field distribution within the gap.

### 5.1 Raman measurement on silicon and diamond

In order to establish a baseline for wavelength dependent measurements on NPoM structures, Raman scattering was first measured on single crystal silicon (Si) and diamond. The choice of these two samples stems from their closeness to the Raman modes of BPT and immediate availability. While neither Si nor diamond degrade in ambient conditions, contaminants may deposit on the surfaces over time. Therefore, each sample was cleaned thoroughly prior to Raman measurements by sonication in acetone, then ethanol and finally in DI water for 5 minutes each. The sample was mounted on the setup after drying under nitrogen. The wavelength of the Ti:Sapph was tuned from 710 nm up to 850 nm in increments of 10 nm and Raman measurements were performed at constant power of approximately 400  $\mu$ W on the sample. The sample position was manually optimized for each wavelength to obtain the highest possible signal. All the acquired spectra were calibrated for the spectral response of the optical setup as described in the last chapter and also normalized by the integration time of the CCD and the laser power.

Scattering spectra of Si recorded using different wavelengths of Ti:Sapph shows a gradual red-shift of the anti-Stokes (blue) and the Stokes (red) peak of Si as the laser wavelength was increased

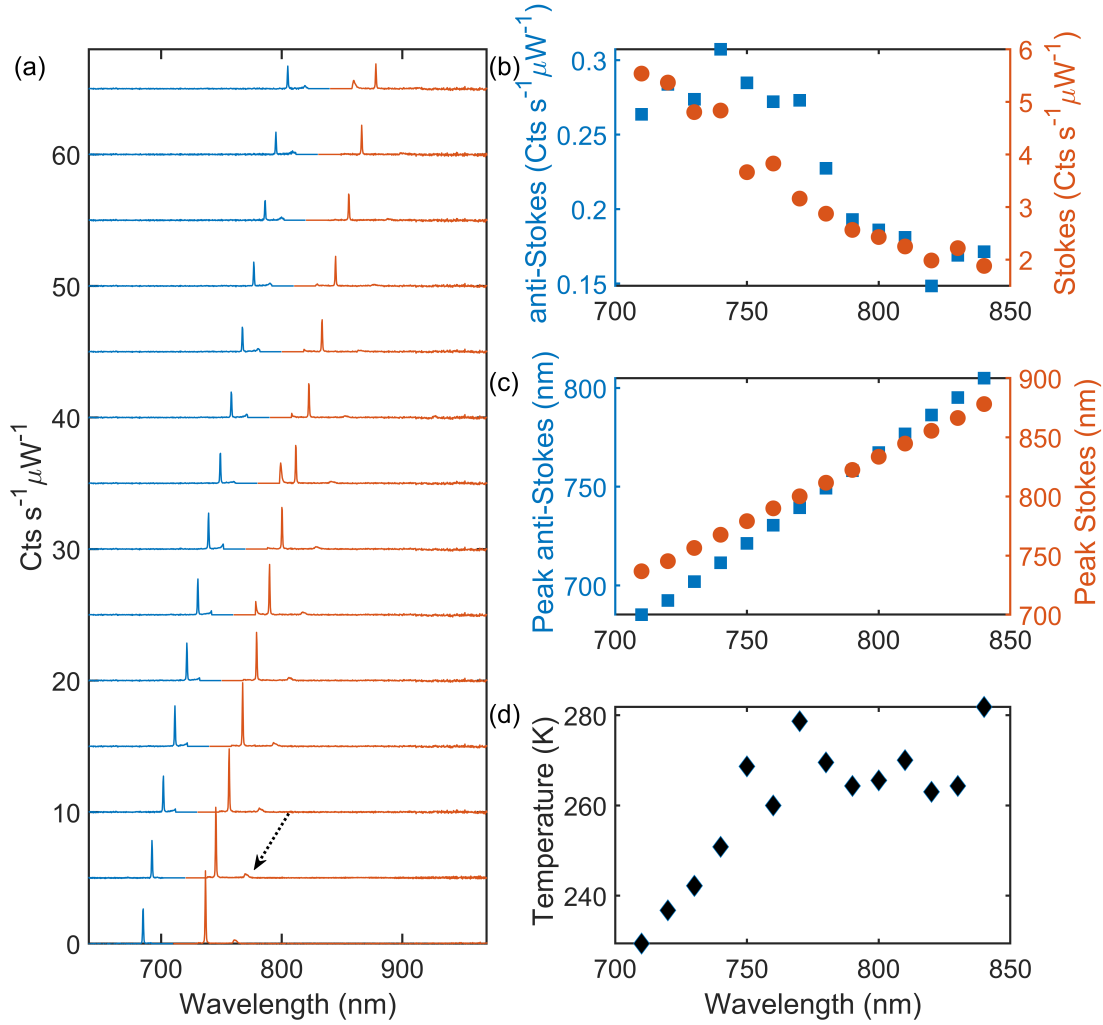


Figure 5.1: **(a)** Raman spectra of Si recorded by different emission wavelength of Ti:Sapph at 400  $\mu\text{W}$ . The anti-Stokes (blue) and Stokes (red) Raman peaks of Si at  $\pm 520\text{ cm}^{-1}$  shift with the laser wavelength. The anti-Stokes sideband has been multiplied by 10 in order to make it more prominent. The change in the intensity of the anti-Stokes and the Stokes peaks **(b)** and the peak position **(c)** shows quantitatively the changes in the Raman peaks as the Ti:Sapph wavelength is tuned. **(d)** The absolute temperature computed using 5.1 with the parameter extracted in **b, c**.

(Figure 5.1 a). The anti-Stokes sideband was multiplied by a factor of 10 to increase visibility (Figure 5.1 a). Apart from the Raman mode of Si at  $521\text{ cm}^{-1}$ , a smaller Raman peak is also observed at approximately  $950\text{ cm}^{-1}$  due to the OH molecules adsorbed on Si surface (Figure 5.1 a, black arrow). The amplitudes of the anti-Stokes (blue square) and Stokes (red circle) peak as well as their peak positions were extracted from the Raman spectra and are presented as a function of the Ti:Sapph wavelength (fig 5.1 b,c). As Raman scattering intensity is proportional to the 4<sup>th</sup> power of the incident frequency [138], therefore increasing the Ti:Sapph wavelength results in the decrease of the Stokes and the anti-Stokes as observed (Figure 5.1 b). The gap between the anti-Stokes and the Stokes peak also increased due to the inverse relation between the

Raman shift and wavelength. While the anti-Stokes as well as the Stokes peak positions linearly redshift with the Ti:Sapph wavelength, the slope is different due to change in gap between the anti-Stokes and Stokes peak. The molecular temperature was also estimated using the ratio of anti-Stokes to Stokes intensity ( $I_{as}/I_s$ ):

$$T[K] = \frac{-\tilde{\nu} * 1.439[K.cm]}{\ln(I_{as}/I_s) * (\lambda_{as}/\lambda_s)^3} \quad (5.1)$$

where  $T$  is the absolute temperature in kelvin (K),  $\tilde{\nu}$  is the Raman shift in  $cm^{-1}$  while  $\lambda_{as}$  and  $\lambda_s$  are the peak positions of anti-Stokes and Stokes peaks on the wavelength axis. The term,  $(\lambda_{as}/\lambda_s)^3$  accounts for the difference between the cross-section of anti-Stokes and Stokes scattering. The exponent is chosen to be 3 since the CCD is essentially a photon counter and not an energy sensor [139]. The value 1.439 [K.cm] is derived from  $hc/k_b$ , where  $h$  is the Planck's constant,  $c$  is speed of light in vacuum,  $k_b$  is the Boltzmann's constant. As all experiments were carried out at room temperature, the calculated temperature is not very accurate but reasonably close. The deviations can be attributed to a combined effect of sample heating under highly focused beam and the response function of the setup which was calibrated using unpolarized light source while the Raman signals are polarized.

The measurements performed on diamond lead to similar trends in Raman scattering as observed earlier for Si (Figure 5.2). Comparing the Raman signal of Si and diamond, the signal in the anti-Stokes sideband was approximately 20 times lower than with Si while the intensity of the Stokes sideband was similar for both samples. The anti-Stokes signal (blue) has been multiplied by 200 to increase visibility in Figure 5.2 a. The decrease in the anti-Stokes intensity is attributed to the higher energy of the vibrational mode (large Raman shift) of diamond which leads to lower phonon population compared to Si. The contribution of ambient temperature to phonon population is higher at lower Raman energies and so in case of Si this results in a larger phonon population and a higher anti-Stokes signal. The ratio of anti-Stokes to Stokes peaks from diamond provide more realistic values of absolute temperature. And hence, the temperature is greatly dependent on the Raman modes of the samples.

Power dependent measurements were also performed in Si using Ti:Sapph at 710 nm. The laser power was increased from approximately 10  $\mu$ W to 12 mW in irregular steps and the Raman spectra were recorded at each step along with the laser (Figure 5.3 a). Beginning with the lowest laser power, the sample position was manually adjusted to obtain the highest Raman signal. The laser power was gradually increased by turning the LH (Figure 5.2). Prior to excitation of the sample, the laser power was measured by the PM before the objective. Next, the sample was excited by the laser and 30 Raman spectra were then acquired at 0.1 Hz. The measurement of laser power and the acquisition of the corresponding Raman spectra was performed in an autonomous fashion after the initial positioning of the sample. Similar to wavelength dependent measurements, the peak amplitude and the peak position were recorded for anti-Stokes and

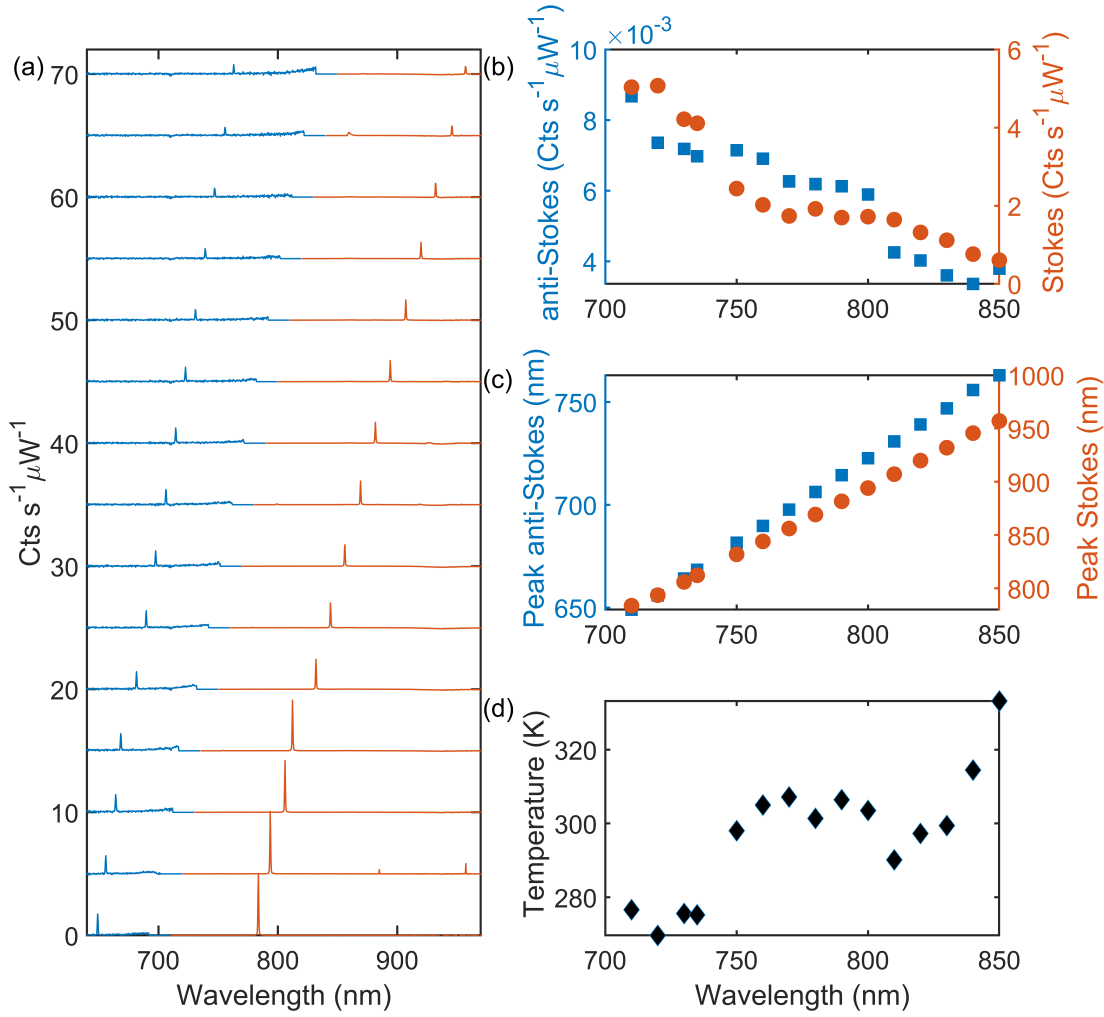


Figure 5.2: **(a)** Raman spectra of diamond recorded by different emission wavelength of Ti:Sapph at 400  $\mu$ W. The anti-Stokes (blue) and Stokes (red) Raman peaks of Si at  $\pm 1332$   $\text{cm}^{-1}$  shift with the laser wavelength. The anti-Stokes sideband has been multiplied by 200 in order to make it more prominent. The change in the intensity of the anti-Stokes and the Stokes peaks **(b)** and the peak position **(c)** shows quantitatively the changes in the Raman peaks as the Ti:Sapph wavelength is tuned. **(d)** The absolute temperature computed using Equation 5.1 with the parameter extracted in **b**, **c**).

Stokes sidebands (Figure 5.3 b, c). The peak counts observed for Stokes were slightly higher in this experiment which could be due to replacement of the CCD and realignment of the setup. A sudden change in both the anti-Stokes and the Stokes is observed which is attributed to shift in the sample position in between measurements (Figure 5.3 b). No change is observed in the peak position of the Raman peaks which is also indicative of negligible change in temperature on the sample surface due to laser irradiation (Figure 5.3 c). The absolute temperature is also computed using Equation 5.1 with the ratio of anti-Stokes to Stokes intensity. However, the calculated values are much lower due to higher Stokes intensity. Despite having an offset of 100 K for room

temperature, the relative variation of the calculated temperature did not change significantly, as the laser power was increased.

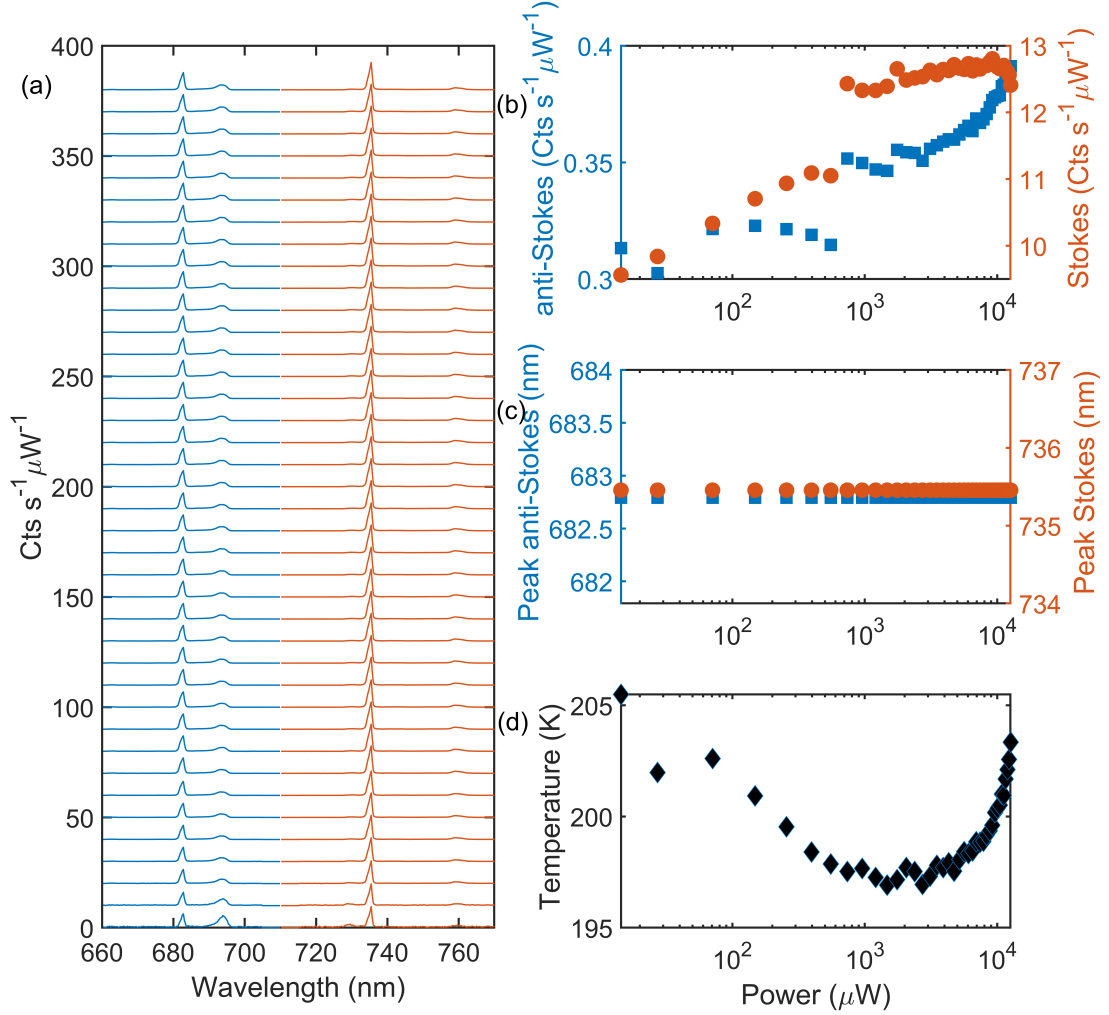


Figure 5.3: **(a)** Raman spectra of Si recorded with Ti:Sapph at 710 nm and gradually increasing power. The anti-Stokes (blue) and Stokes (red) Raman peaks of Si at  $\pm 520\text{cm}^{-1}$  when normalized by the laser power remain almost the same. The anti-Stokes sideband has been multiplied by 10 in order to make it more prominent. Negligible change in the intensity of the anti-Stokes and the Stokes peaks **(b)** and the peak position **(c)** was observed as the laser power was tuned. **(d)** The absolute temperature computed using Equation 5.1 with the parameter extracted in **b, c)**. The extracted temperature shows much less fluctuations than those observed during wavelength dependent measurements.

## 5.2 Effect of incubation time on NPoM

Although, both the wavelength and power dependent measurement can be performed easily on Si and diamond, doing the same on NPoMs is far from trivial. The NPoMs with SAM as spacer

are particularly sensitive to laser power and wavelength, hence tremendous care is required to avoid damaging the NPoM during measurement. Unraveling the impact of laser excitation on SAM based NPoM structures and the principles that govern it is immensely valuable to design better nanocavities. By combining the Raman (Figure 5.4 a) and DF (Figure 5.4 c) measurements, a comprehensive estimate of the optical response of NPoM and the state of SAM molecules within can be derived. While Raman scattering provides information regarding the integrity and vibrational state of molecules within the SAM (Figure 5.4 b), DF spectroscopy is also used to measure any changes in the LSPR modes of the nanocavity (Figure 5.4 d). The EM enhancement of these modes renders them extremely sensitive to the dielectric environment and the structural parameters of the NPoM [140, 32, 141]. Although a large number of studies have treated the kinetics of self-assembly of thiols on noble metals [142, 143], there is a profound lack of literature regarding effect of molecular organization on the optical properties of NPoM. To bridge this gap in understanding, NPoM structures with distinct molecular orientation and packing of the BPT SAM layer were prepared and studied using Raman and DF measurements. The molecular organization is varied by incubating the sample in the thiol solution for different duration. The experiment was limited to two incubation times, 2 hours (labeled S2) and 24 hours (labeled S24), which lead to distinct SAM orientations as confirmed later by STM and EC characterization. These differences in SAM were extensively investigated using electrochemical (EC) characterization and scanning tunneling microscopy (STM).

### 5.3 EC and STM characterization of SAM

The difference between S2 and S24 in terms of molecular orientation and packing were also confirmed via EC characterization and STM. In the former method, the molecular ordering of BPT SAMs is detected using reductive desorption ( $\text{Au} - \text{S} - \text{C}_6\text{H}_4 - \text{C}_6\text{H}_5 + \text{e}^- \rightarrow \text{Au}_0 + \text{S} - \text{C}_6\text{H}_4 - \text{C}_6\text{H}_5$ ) with the specific signature being cathodic waves. The peak positions, i.e. potential of the reductive desorption, strongly depend on the lateral interactions between BPT molecules [127, 144] and are indirectly related to the density of the SAM packing. The desorption peak of densely packed SAMs is thus shifted to the more negative potentials (Figure 5.5). The peak width and the area under the peak depend on the number of the thiol molecules desorbing from the Au surface at a given potential. Broad desorption peaks are thus related to the ill-defined SAMs of low-packing density. It is imperative to note that EC characterization is a global characterization technique where SAM desorbs over the whole sample surface. It provides information on the molecular ordering over the macroscopic scale. (The text in this paragraph is extracted from [81].)

Cyclic voltammograms of S24 and S2 prepared on glass/Cr/Au substrate show the distinct configuration of molecules within the SAM (Figure 5.5 a). Cathodic peaks at -0.88 V and -0.85 V versus Ag/AgCl reference electrode correspond to reductive SAM desorption on S24 and S2, respectively. Since desorption of highly-ordered SAM proceeds at more negative potentials, the shift of approximately -30 mV for S24 suggests a high degree of SAM ordering. Moreover, broad desorption peak on S2, with the center slightly shifted towards positive potentials, implies



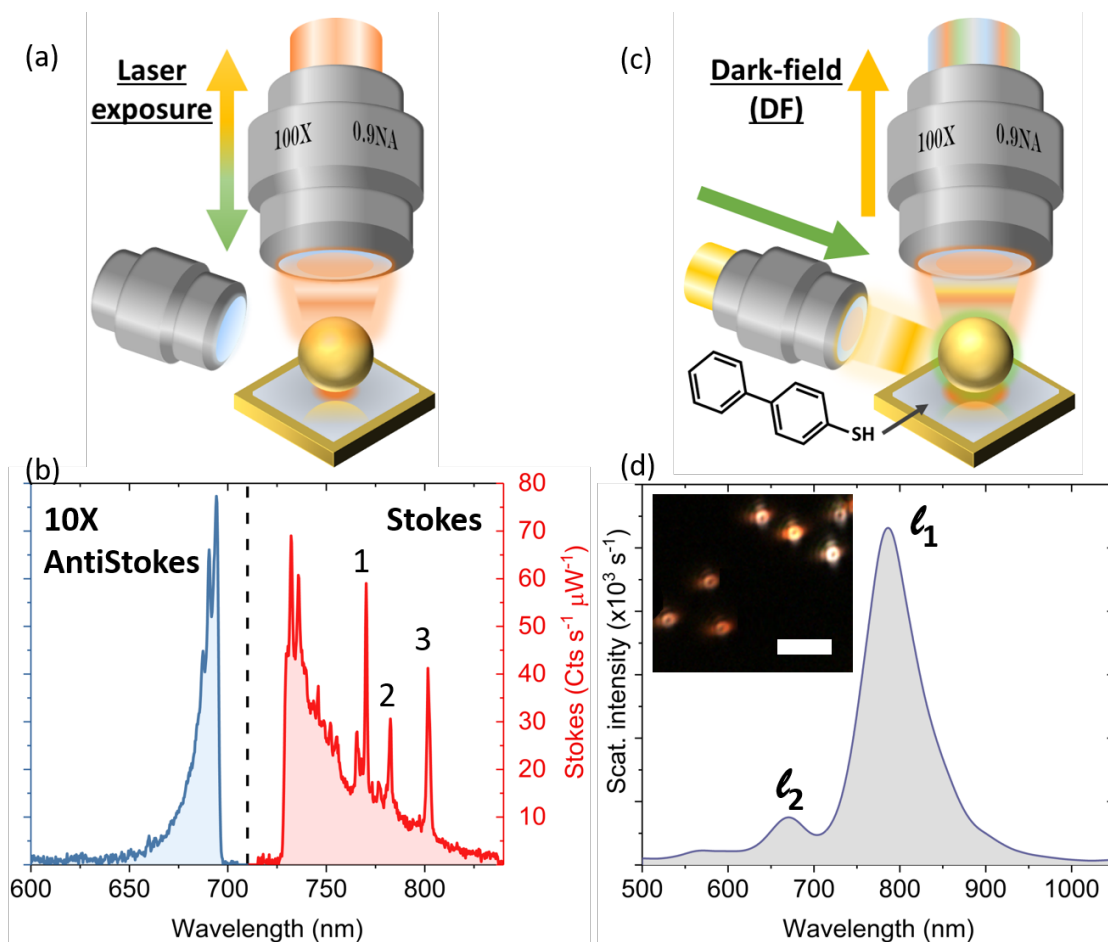


Figure 5.4: **(a)** For the Raman measurements, light is focused on the NPoM and the Raman signal collected through the same objective. **(b)** Example of Raman spectrum. The dashed line represents the laser wavelength at 710 nm. The Raman modes of BPT are clearly visible on the Stokes (red line) side where 1, 2, and 3 symbolize the main Raman peaks for BPT at 1079, 1281 and 1586  $\text{cm}^{-1}$  respectively. For the anti-Stokes (blue color), the electronic Raman background is dominant, and can be used to estimate the electronic temperature. **(c)** Schematics for dark-field (DF) scattering spectroscopy. White light is used to illuminate the NPoM from the side (green arrow), while the scattered light is collected (yellow arrow) via a 0.9 NA objective. **(d)** Example of DF spectrum showing bonding dipole plasmon  $l_1$  mode and a higher order dipole mode  $l_2$ . The inset is a DF image of the sample showing multiple NPoMs. Scale bar is 1  $\mu\text{m}$ . (Figure and caption adapted from [81].)

that BPT SAM on S2 is globally in ill-defined phase. We also note the fine structure in the S2 voltammetric wave (Figure 5.5 b). The shoulder observed in S2 voltammogram, shifted to the negative potentials with respect to the main peak, might arise from the presence of small ( $< 50 \text{ nm}^2$ ), densely-packed SAM domains. Therefore, a closer investigation of the SAM structure is performed using STM. (The text in this paragraph is extracted from [81].)

STM characterization was performed on the mirror substrate (i.e. template stripped Au) following

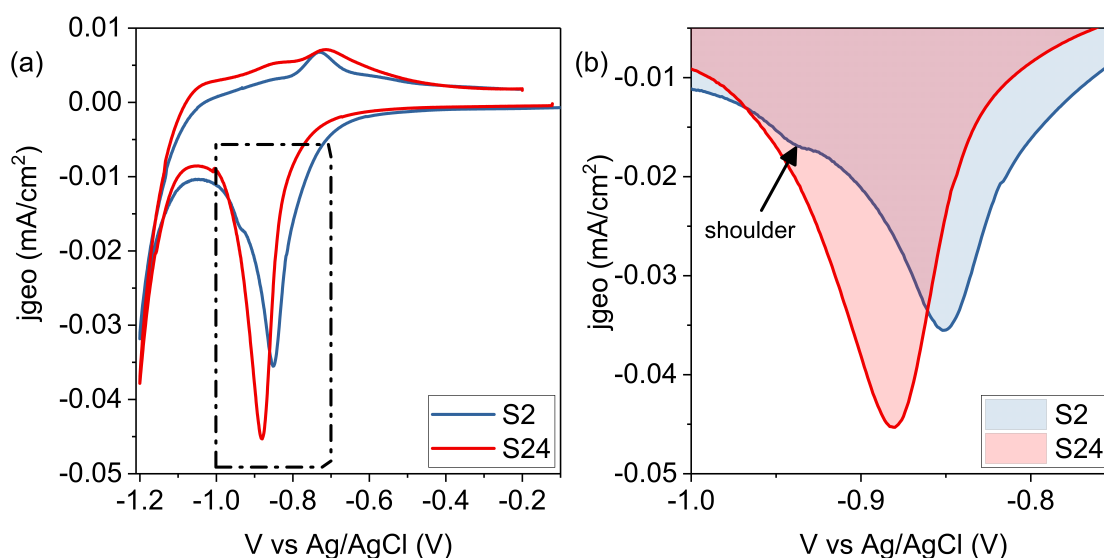


Figure 5.5: Cyclic voltammograms showing the reductive desorption (oxidative adsorption) in the negative (positive) direction of BPT SAM prepared upon incubation of glass/Cr/Au substrates during 24 hours (S24, red solid line) or 2 hours (S2, blue solid lines). **(b)** shows an enlarged view of the desorption SAM peaks (dot dashed line). Data acquired and analyzed by Karla Banjac. (Figure and caption adapted from [81].)

the same procedure as for NPoM preparation. As discussed earlier, SAM characterization on the mirror substrate is of great importance since molecular ordering depends on surface crystallinity, the size of the terraces, and the presence of surface defects. The STM images of S24 (Figure 5.6 a) and S2 (Figure 5.6 b) over  $45\text{ nm} \times 45\text{ nm}$  Au surface functionalized with SAMs show clear differences both in the morphologies of Au surface and in SAM ordering. High-resolution STM images of SAM layer on S24 show regular patterns characteristic for the densely-packed phase where the thiol molecules are in up-right conformation [134] as illustrated on the scheme under (Figure 5.6 c). This assignment agrees with UHV-STM studies reporting densely packed BPT SAMs in up-right conformation prepared upon long incubation [106, 145]. STM images of BPT SAM on S2 show corrugations in the angstrom range without a well-defined pattern observed on S24 (Figure 5.6 d). Large scale STM images appear fuzzy: while the SAM layer fully covers the surface, the fuzziness is related to the mobility of BPT molecules. The absence of a periodic pattern suggests that the SAM on S2 is less-densely packed than the SAM on S24. Both sparser packing and higher mobility of the molecules suggest that the SAM on S2 are mostly in the lying-down phase, with the principal molecular axis making a large angle with respect to the surface normal. To the best of our knowledge, this is the first STM observation of the lying-down phase of BPT SAM at the liquid/solid interface. (The text in this paragraph is extracted from [81].)

The importance of the crystalline structure of the mirror is highlighted by STM scans that reveal the co-existence of at least two distinct, densely-packed SAM phases with the molecules in the up-right conformation on neighboring Au facets (Figure 5.7). STM images show significant

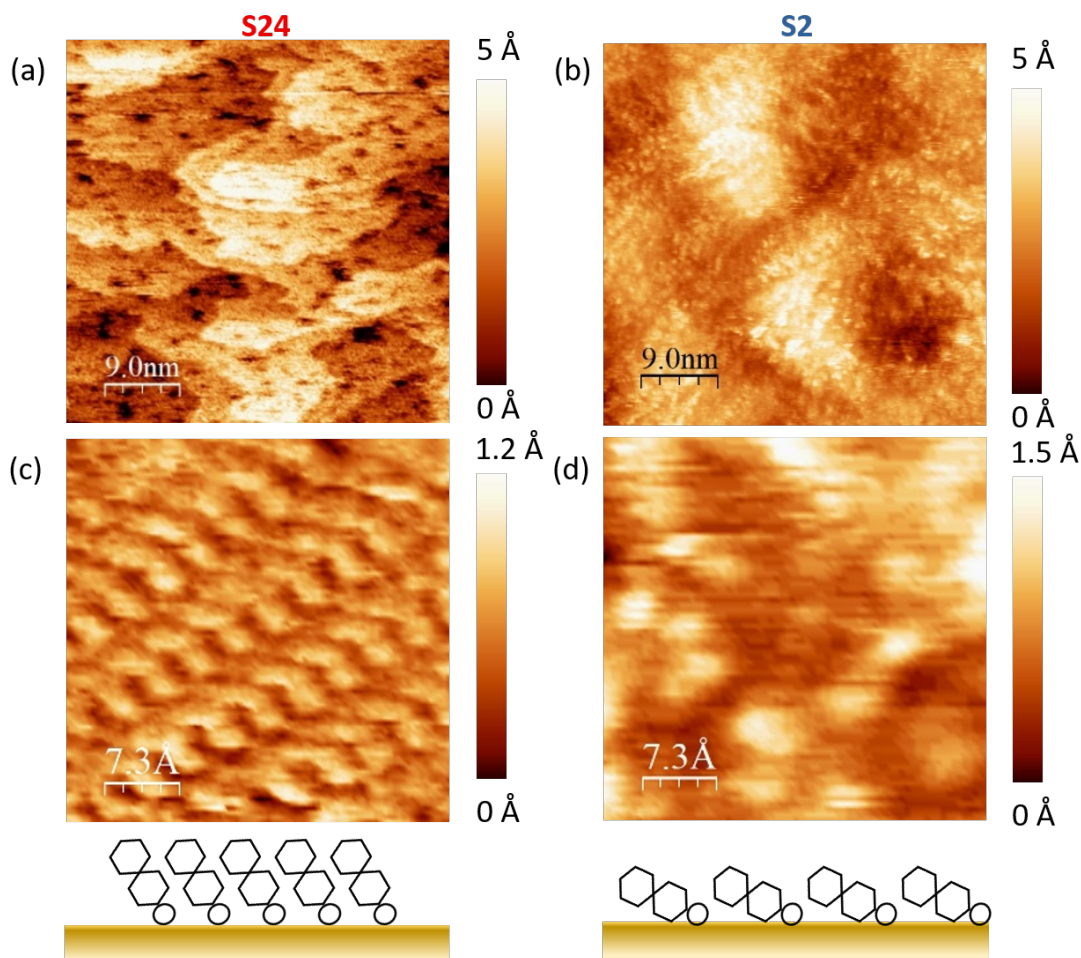


Figure 5.6: **(a, c)** STM images of BPT SAM on S24. The large scale STM image **(a)** shows the terraces and the pits formed upon Au surface reconstruction. Small scale STM image **(c)** shows the pattern characteristic for the densely packed BPT SAM phase illustrated in the schematics below. **(b, c)** STM images of BPT SAM on S2. Large scale STM image **(b)** shows a corrugated Au surface with randomly disturbed dot-like features. Small scale STM image **(d)** shows the dot-like features appearing fuzzy. Scanning parameters for bias voltage ( $V_{\text{bias}}$ ) and tunneling current ( $I$ ): **(a, c)**  $V_{\text{bias}} = 200$  mV,  $I = 338.2$  pA and  $V_{\text{bias}} = -336$  mV,  $I = 420$  pA, **(b, d)**  $V_{\text{bias}} = 586$  mV,  $I = 567.6$  pA and  $V_{\text{bias}} = 532$  mV,  $I = 482.1$  pA. Data acquired and analyzed by Karla Banjac. (Figure and caption adapted from [81].)

differences between the two upper facets and the lower facet. Two upper facets appear nanostructured due to a few angstrom-large protrusions; yet, no periodic arrangement is observed. The lower facet appears nanostructured due to the curved terraces (lateral size  $> 10$  nm) and dark, round features (i.e. pits formed upon reconstruction). These differences in the appearance of the crystalline facets imply that different SAM phases co-exist along S24. Heterogeneities in BPT SAM ordering on the samples prepared upon prolonged incubation in ethanoic solutions is in agreement with earlier reports [106, 134]. We speculate that BPT SAMs on adjacent Au

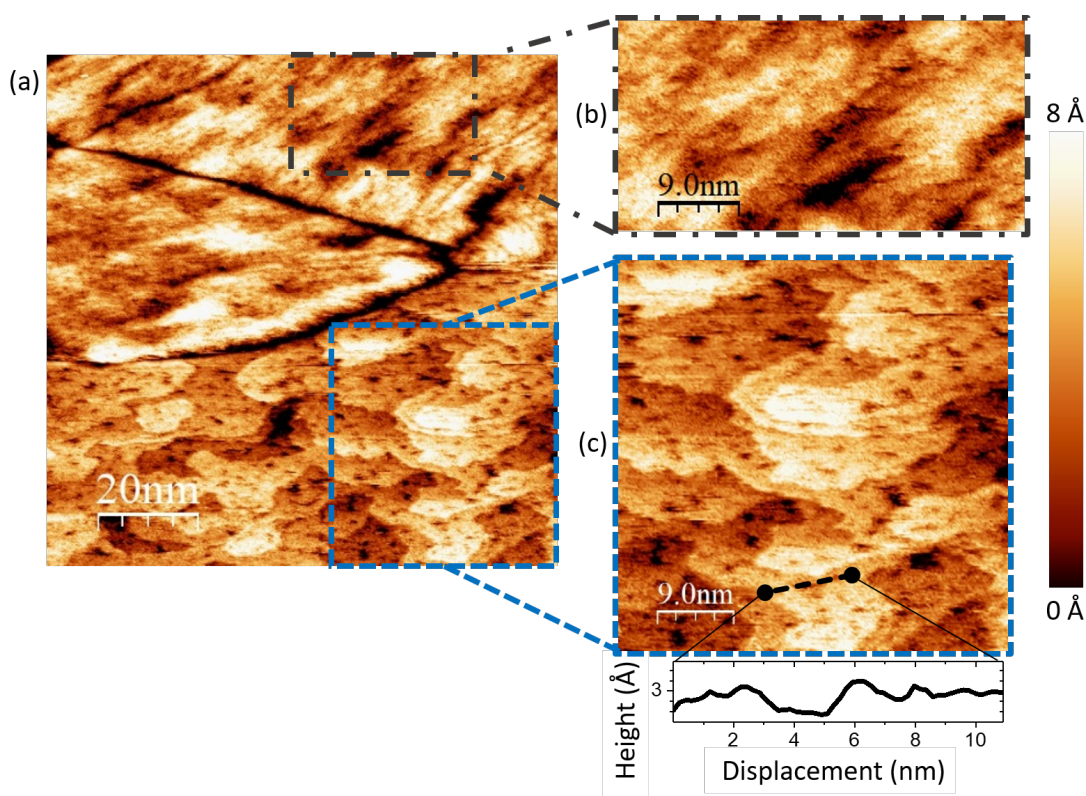


Figure 5.7: STM characterization of the BPT SAM molecular ordering on S24. **(a)** Large scale STM image showing different BPT phases on three adjacent Au facets. **(b)** Magnified STM image of the upper facet shown in **(a)**. No periodic arrangement, visible on STM images as the regular patterns, suggests that the degree of the molecular ordering is lower than for phase shown in **(c)**. **(c)** Magnified STM image of the lower facet shown in **(a)**. The presence of the curved terraces (lateral size  $> 10$  nm) and dark, Au vacancy islands (pits) randomly distributed along them are morphological features characteristic for the surface reconstruction that proceeds parallel to the SAM re-organization [106]. All images were obtained at the air/solid interface. Scanning parameters:  $V_{\text{bias}} = -200$  mV,  $I = 338.2$  pA. Data acquired and analyzed by Karla Banjac. (Figure and caption adapted from [81].)

facets are in densely-packed phases with the small tilt angles between the principal molecular axis and the surface normal, as expected for SAMs prepared upon long immersion [106]. The template stripped Au (i.e., the mirror in NPoM) is a polycrystalline surface with mostly (111) crystalline facets - it contains (100) and (110) facets. Each of these facets may support a different SAM structure (in term of the molecular configuration); domains with weakly adsorbed double layers or even multilayer structures are also possible, as recently reported for similar system [128]. The direct consequence of the heterogeneities in S24 BPT SAM ordering is evident in DF measurement as shown later. Each NPoM on S24, prepared upon drop-casting AuNPs on the S24 BPT SAM-functionalized mirror, has a different gap height, as evident from the deviations in the peak position of the dipole mode. These deviations are found to be more profound for S2 due to the high mobility of the BPT molecules in lying-down phase. The NPoMs on a single sample



may also have different gap heights due to the presence of different SAM domains.

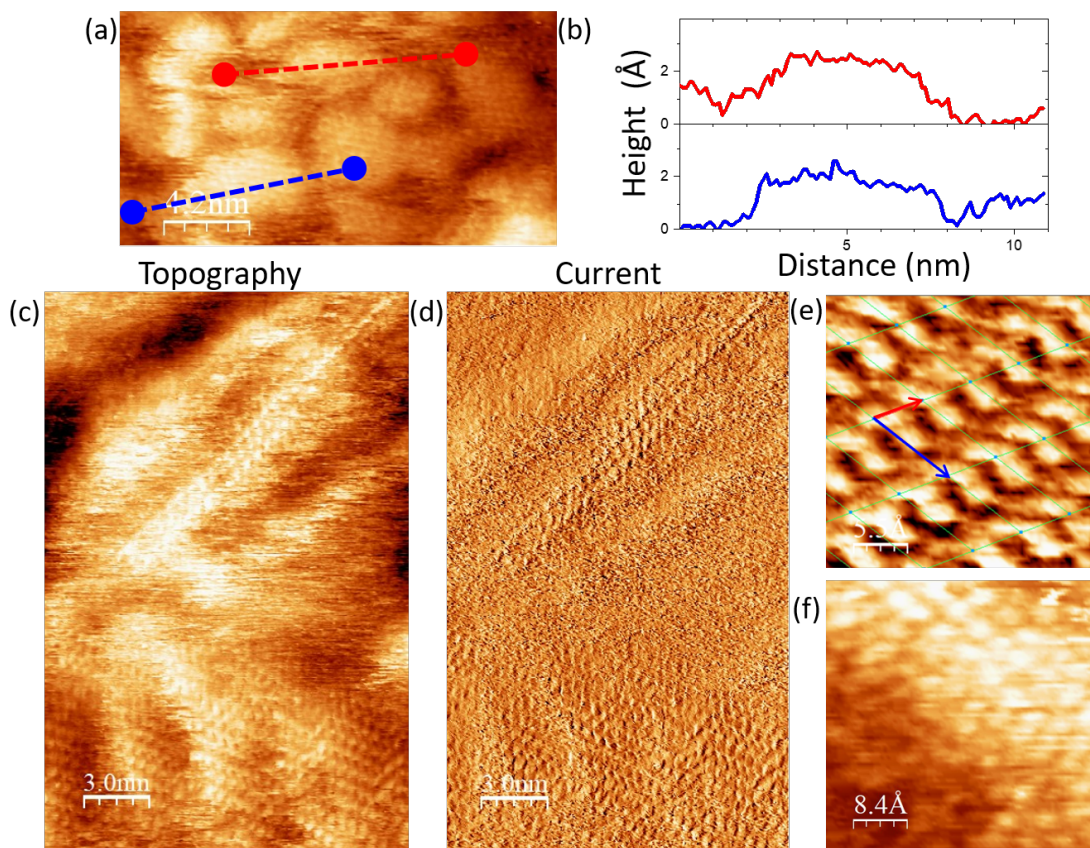


Figure 5.8: **(a)** STM image of S24 showing Au islands formed upon surface reconstruction. The apparent height and width of islands are approximately 2.4 Å and 5 nm respectively, as shown in height profiles in **(b)**. Note that the herringbone pattern of the BPT SAM is visible on the islands' tops: this suggests that these islands are formed upon motion of the thiolate-Au adatom moieties. The formation of these islands is closely related to the formation of the vacancy depressions shown in (Figure 5.7 a). This image was obtained at the nonanoic acid/solid interface. Scanning parameters:  $V_{bias} = -200$  mV,  $I = 338.2$  pA. STM topography **(c)** and current **(d)** images showing the same Au terraces on S24. Note the herringbone pattern extending over the terraces. This suggests that the SAM domains are not confined by the step edges of the terraces (or the small islands shown in Figure S2). Single SAM domain extends over, at least, 10 nm; however, multiple SAM domains are present along the single Au crystalline domain regardless of its orientation or lateral size. **(e)** Herringbone pattern of BPT SAM on S24 together with the superimposed lattice  $2\sqrt{3}rt \times \sqrt{3}rt$  unit cell. **(f)** STM topography image showing the domains with densely packed BPT SAM on S2. Scanning parameters:  $V_{bias} = -573$  mV,  $I = 494$  pA. Data acquired and analyzed by Karla Banjac. (Figure and caption adapted from [81].)

Atomic scale reconstruction of the Au facets was also observed for samples prepared with longer incubation time. STM images of S24 reveal the presence of Au adatom islands and pits formed upon lifting Au reconstruction (Figure 5.8 a). The profile of the islands extracted from the STM data suggests a height and width of 2.4 Å and 5 nm respectively (Figure 5.8 b). The SAM

morphology on such reconstructed facets was also found to be in a densely-packed phase with up-right conformation. The topography (Figure 5.8 c) and the current (Figure 5.8 d) measured on the restructured Au terraces show the herringbone pattern in Au (111) along with the SAM. Multiple domain are also found to coexist even on the single Au crystals. The molecular orientation on the Au surface can be found by imposing the Au (111) lattice on SAM (Figure 5.8 e). The SAM induced reconstruction found on S24 was absent in samples with low incubation time. However, small highly ordered SAM domain were found to be present (Figure 5.8 e). This is in agreement with the shoulder observed in S2 desorption peak during EC characterization (Figure 5.5 b).

Properties	S2	S24
Potential versus Ag/AgCl (V)	-0.85	-0.88
<i>FWHM</i> (V)	0.07	0.08
<i>Q</i> ( $\mu\text{C}/\text{cm}^2$ )	65	72

Table 5.1: Position, full-width at half-maximum (*FWHM*), and charge density (*Q*) of the peaks in the voltammograms of Figure 5.5. Data analyzed by Karla Banjac. (Adapted from [81].)

The results of the EC characterization and STM for the two sample S2 and S24 are summarized as follows. The parameters for the reductive desorption peaks shown in Figure 5.5 are listed in Table 5.1. The main differences in the integrated charge density being  $65.2 \mu\text{C}/\text{cm}^2$  for S2 and  $72.4 \mu\text{C}/\text{cm}^2$  for S24 imply less dense BPT SAM layer on S2 comparing to the BPT SAM layer on S24. These estimates on integrated charge are not directly comparable to the literature on electrochemical characterization of aromatic thiol SAMs [107, 146] as the glass/Cr/Au (mirror) used in this work were not flame annealed. Nonetheless, formation of the less dense phase on S2 is in agreement with literature on characterization of similar systems prepared upon immersion in thiol solutions [106, 134] or evaporation [145]. Interpretation of reductive desorption, disclosing differences in the BPT SAM ordering on global scale, is not straight forward due to the fact that several BPT SAM phases coexist on the neighbouring crystalline facets (Figure 5.7). BPT SAM heterogeneity is especially important for interpretation of the optical measurements on single NPoM mostly likely due to the differences in SAM heights for each NPoM. We thus evaluate the molecular ordering on S24 and S2 from STM images revealing the presence of the highly ordered BPT SAMs across several hundred nanometers over the single crystalline facet on S24 and confined to the domains with the lateral dimensions  $< 10 \text{ nm}$  on S2 together with disordered BPT SAM on S2. The distances between protrusions on S24, as-measured from the height profiles superimposed on the molecular rows in Figure 5.6 c, are  $8.90 \pm 0.9 \text{ \AA}$  along the single row and  $4.2 \pm 1.0 \text{ \AA}$  across two rows implying on the square lattice close to the  $2\sqrt{3} \times \sqrt{3}$  structure (Figure 5.8 e). This finding is in excellent agreement with the findings of Azzam et al. [106] and Leung et al. [134] reporting on formation of SAMs with  $2\sqrt{3} \times \sqrt{3}$  structure and small domains upon long immersion in ethanolic solutions at room temperature. The phase with  $2\sqrt{3} \times \sqrt{3}$  structure, denoted as  $\epsilon$  phase by Azzam et al. [106], is characterized by a tilt angle between the molecular axis and the surface normal  $< 20^\circ$  [134, 147] and islands formed upon surface reconstruction (Figure 5.8 a). Highly ordered BPT SAMs domains on S2, having lateral size  $< 10 \text{ nm}$ , co-exists



with disordered phase shown in Figure 5.6 b, d. Interestingly, poor resolution of the disordered phase is in full agreement with references [106, 134] reporting on poor quality of STM images of the BPT adlayers.

## 5.4 SAM dependent optical stability of NPoM

The scattering spectra collected from 25 single NPoMs on each, S24 (Figure 5.9 a) and S2 (Figure 5.9 b), sample indicate the distinction between the two gap layers. The NPoMs were formed using 80 nm diameter Au nanospheres (AuNS). In case of S2 NPoMs the BDP mode is redshifted by approximately 100 nm when compared to S24 hinting at a lower spacer thickness of S2 NPoMs. This hypothesis is further supported by the smaller amplitude of the BDP mode observed on S2 NPoMs. The decrease in the gap height leads to increased tunneling of charges between the Au nanospheres and the mirror thus reducing the amplitude of BDP mode [82]. The observed DF spectra in each case can be matched to scattering spectra obtained by varying the gap height in boundary element method (BEM) simulations (Figure 5.9 dashed line) [29]. For the simulations the NPoM is modelled by considering SAM as a dielectric layer, with refractive index of 1.4, between 80 nm diameter Au nanosphere and infinite Au mirror. A round facet with a 30 nm diameter is assumed on the bottom of the Au nanosphere. The simulations assign a gap height of 0.8 nm and 1.4 nm to S2 and S24 respectively.

The NPoMs formed using the two types of SAM were optically probed by irradiating with a constant laser power for 5 minutes while measuring the scattered Raman signal. The scattering spectra of the NPoMs was recorded before as well as after the laser exposure. The Raman and DF measurements were repeated several times in order to observe the evolution of the NPoM with continued laser exposure. The integration time for the Raman measurement was altered however the total duration of laser exposure was kept constant. The laser induced modification of NPoMs was measured by analyzing the amplitude and spectral position the BDP mode in the DF spectra. An example of laser induced effect on the plasmonic modes is present in Figure 5.10. The initial spectrum before laser exposure is labelled as Start. In this case, the position of the BDP mode has increased by 20nm (from approximately 800 nm to approx. 820 nm) and the amplitude has decreased by 1/3 (from approx..  $30 \times 10^4$  to approx.  $20 \times 10^4$ ) with respect to the initial values. The position and the amplitude of the higher order dipole mode are also drastically modified during the exposure, with peak position shifting from approx. 650 nm to approx. 680 nm and the peak height decreasing from approx..  $25 \times 10^3$  to approx.  $50 \times 10^3$ . Hence, plasmonic modes other than the dipole mode may also be investigated to assess the effects of the SAM layer. However, these modes are weakly scattering in comparison to the dipole mode; they may couple to the dipole mode forming hybrid modes and hence it is not trivial to determine their respective locations and amplitudes. Therefore, for this study we limit ourselves only to the behavior of the dominant dipole mode.

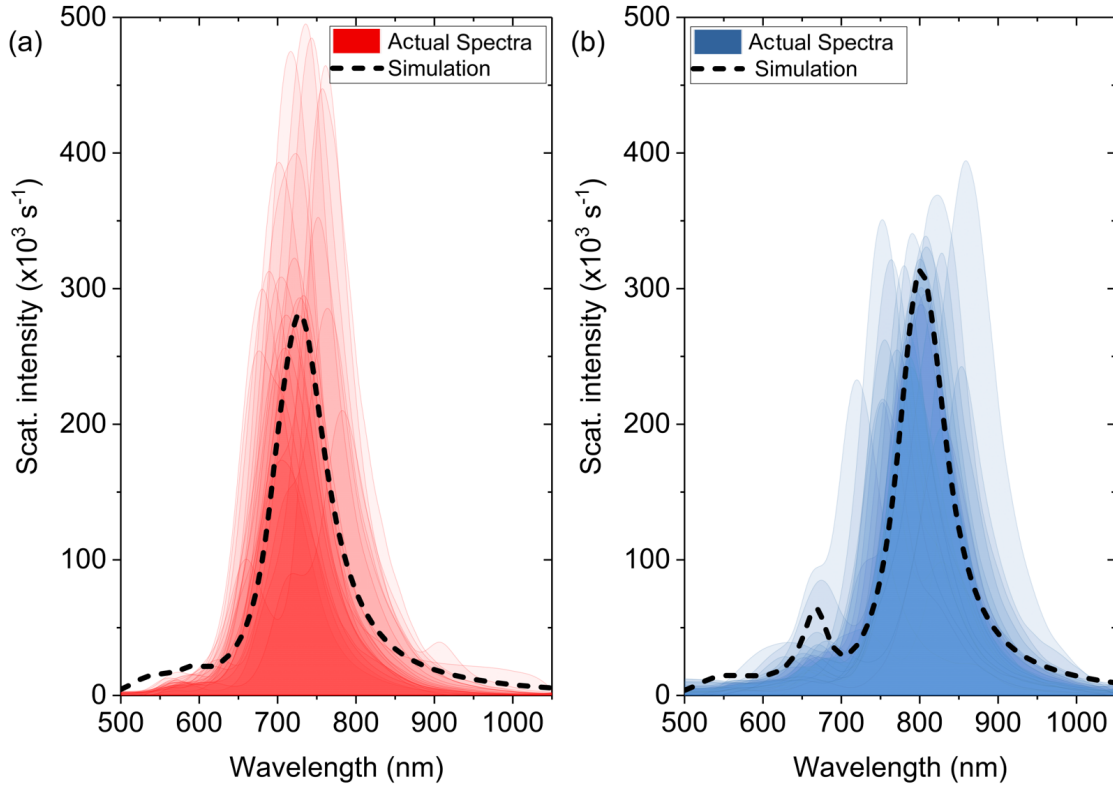


Figure 5.9: DF spectra from all NPoMs measured across S24 (a) and S2 (b). All the spectra are smoothed by moving average of 20 points. The black dashed lines indicate the simulated scattering spectra obtained with a gap height of 1.4 nm in (a) and 0.8 nm in (b); for both the refractive index of the gap and AuNS facet size were 1.4 and 30 nm, respectively. They were computed by boundary element method (BEM) using MNPBEM MatLab package [29] and arbitrarily rescaled in amplitude to fit in the figure. (Figure and caption adapted from [81].)

### 5.5 Measurements with constant laser power

The Raman and DF measurement were first performed using a constant laser during laser exposures. This helps to distinguish between the changes in the BDP caused due to repeated laser exposure at constant power from those caused by the increase in the laser power. The Ti:Sapph power and wavelength for these measurement were kept at 12  $\mu\text{W}$  and 710 nm respectively, to ensure negligible laser damage and to be sufficiently detuned from the BDP mode of the NPoMs. These measurements were performed on 5 NPoMs with each type of SAM and the results are summarized in Figure 5.11. The S2 NPoMs ( $\circ$ ) show a larger variation in terms of the initial resonance of the dipole mode while the S24 NPoMs ( $\square$ ) have a much lower spread. This is consistent with the properties of the SAM layers in both cases as discussed before. The behavior of all the S2 and S24 NPoMs is averaged with respect to the incubation time to better observe the differences between them. The average of S2 NPoMs ( $\bullet$ ) indicates that the initial position (Figure 5.11 a) and peak amplitude (Figure 5.11 b) of the BDP mode are redshifted and slightly lower, respectively when compared to the average S24 NPoMs ( $\blacksquare$ ). Over the course of repeated laser

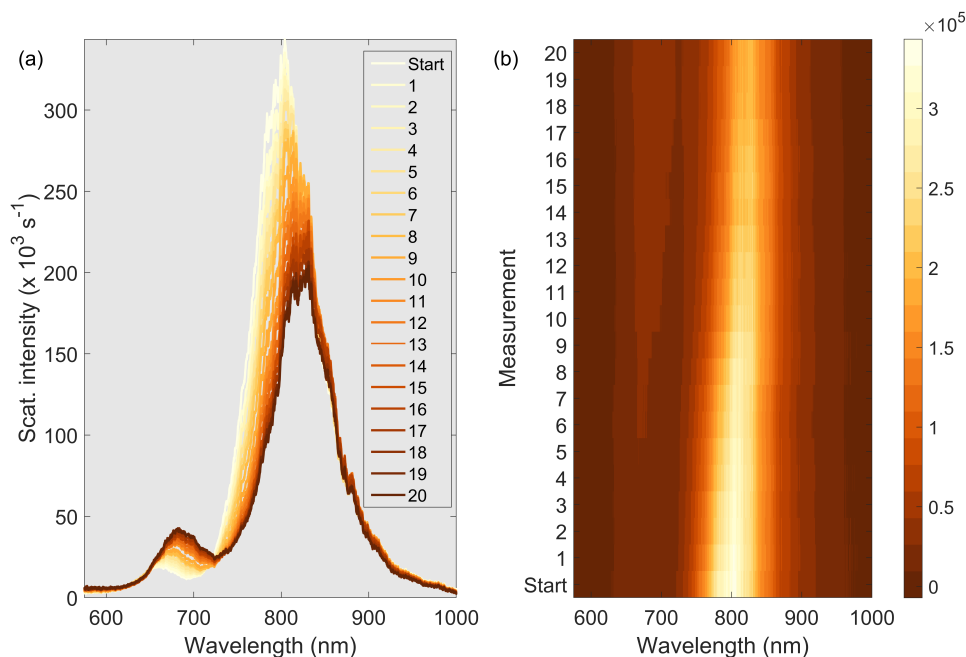


Figure 5.10: **(a)** DF spectra after multiple exposures to laser. The shift from the initial spectrum (Start) is quite evident. **(b)** The same DF spectra but stacked such that the y axis represent the number of 5 minute exposure while the colorbar depicts the scattering intensity.

exposures, the NPoMs on the two SAMs respond very differently. A redshift in peak position along with a decrease in peak amplitude are observed for both SAMs, however the magnitude of these changes is found to be more prominent in S24 NPoMs. A clearer representation of these modifications can be found by observing the percentage of change with respect to the initial value (Figure 5.11 c, d). The change in the position of the BDP mode is comparable between the two SAMs however the S24 NPoM show a much faster decrease in the peak of the BDP mode. The change in peak amplitude is much larger than that estimated to occur due to sample drift over the duration of the measurements. Hence, the differences in the molecular ordering do have a profound influence on the optical response of NPoM. In order to understand the optical parameters responsible for these effects two other experiments were carried out. First, laser exposure at another wavelength (632nm) with constant laser powers to quantify the contributions of laser wavelength. Second, laser exposure with 710 nm and with increasing laser power to discover the damage threshold for each type of SAM.

The exposures at constant power (12  $\mu\text{W}$ ) with 632 nm were performed on different NPoMs then the ones used above but on the same samples. The initial positions and amplitude of the BDP mode are reasonably close comparing to the NPoMs used in the previous experiment. Repeated exposure of S2 and S24 NPoMs using 632 nm results in rapid modifications of the nanocavities. Looking at the trend of the average position of the dipole mode, a change of almost a 80 nm occurs when S24 NPoMs were irradiated with 632 nm (Figure 5.12 a) compared to 20 nm previously

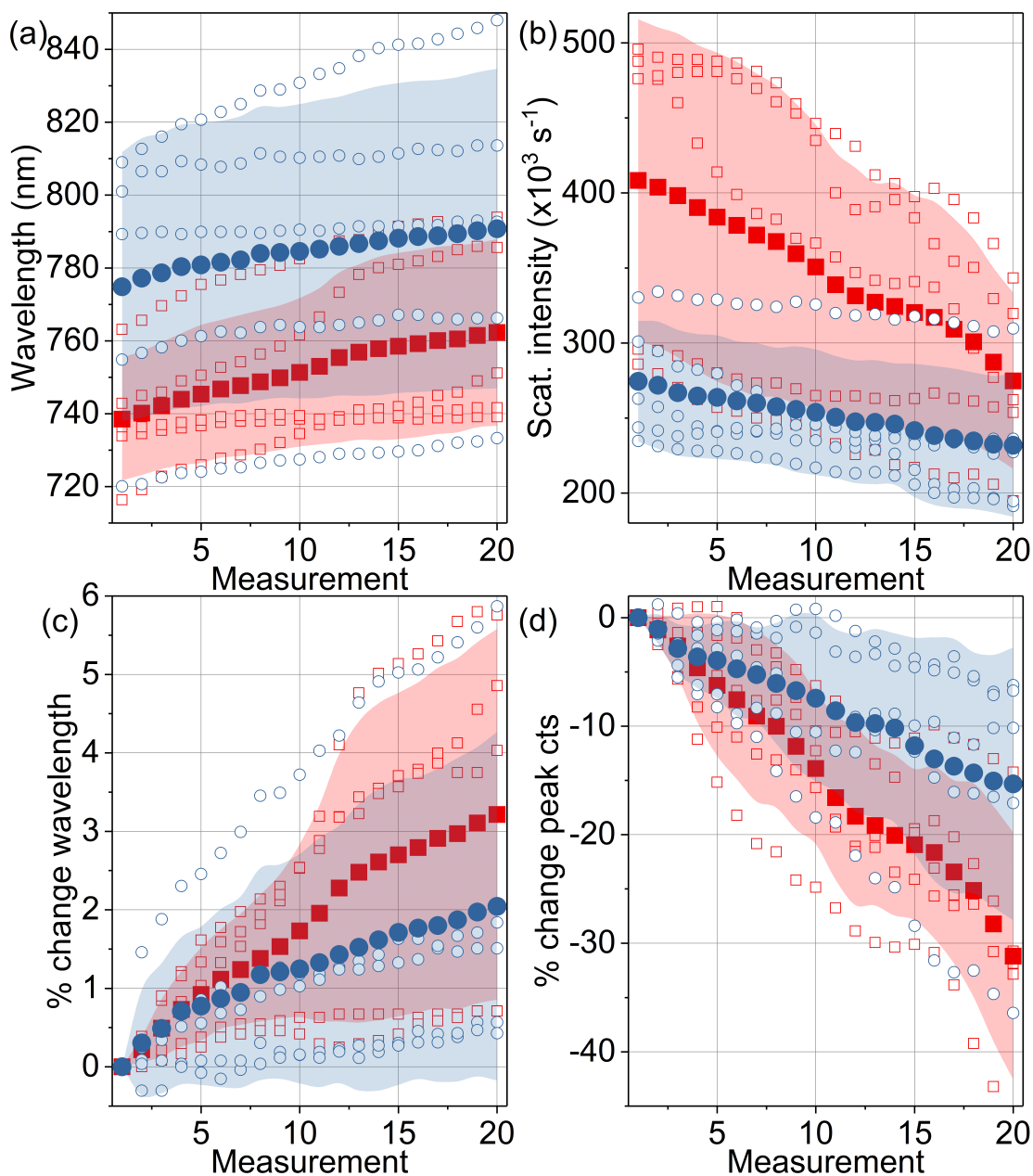


Figure 5.11: Repetitive exposure of multiple S2 (red) and S24 (blue) NPoMs with constant laser power  $12 \mu\text{W}$  at  $710 \text{ nm}$ . The repeated exposures cause a redshift in the peak wavelength of the dipole mode **(b)** along with a decrease in the scattering intensity **(b)**. The percentage of the relative change in the position **(c)** and intensity **(d)** compared to the initial values are also depicted. The measured values are presented using unfilled symbols, while the average and the standard deviation are shown with filled symbols and the shaded regions respectively. The two different SAM layers were prepared by incubating the mirror substrates for 2 (S2) and 24 hours (S24) in BPT solution.

seen with 710 nm. The S2 NPoMs faired slightly well, nonetheless exposure to 632 nm resulted in a steep increase in the position of the dipole mode along with an equally steep decrease in peak amplitude (Figure 5.12 b). The slope of the induced changes in peak position and amplitude for S2 NPoMs stagnates around the 10<sup>th</sup> measurement and becomes flat (Figure 5.12 c,d). This feature is not found during the excitation of S2 NPoMs by 710 nm further supporting that the modification induced by 632 nm occur at much faster rate than with 710 nm. The S24 NPoMs also show a similar behavior however continue to evolve at a much faster rate than that observed for S2 NPoMs. As 632 nm is significantly detuned from the average position of the dipole mode in unexposed NPoMs on both S2 and S24, the expected modification should have been lower than that observed for 710 nm. The contradiction between the observed and the expected results could be attributed to the increased Raman activity of molecules when excited with 632 nm compared 710 nm. Thus, the laser wavelength has an impact on the NPoM structure only due to the increased vibrational activity within the SAM and not due to the EM field enhancement within the nanocavity.

## 5.6 Measurements with increasing laser power

Once again, the power dependence experiments were carried out on pristine NPoMs on the same samples. After the measurement of the initial DF spectrum, each NPoM was illuminated with a tightly focused laser beam tuned at 710 nm and the Raman spectrum from BPT was measured after filtering the laser line, in order to probe the integrity of the molecules. The laser power was first set to the lowest value of approximately 8  $\mu$ W and the NPoM was exposed to the laser for 5 minutes, during which the Raman signal from BPT is recorded. Here also the integration time per frame of the CCD and the number of frames per measurement were adapted depending on the strength of the Raman signal, while keeping the total laser exposure to 5 minutes for each power. After laser exposure, the DF spectrum is measured, and the cycle is repeated after an increase of the laser power. Examples of typical changes to the DF spectra upon laser exposure for the two different samples are shown in Figure 5.13 and Figure 5.14. (The text in this paragraph is extracted from [81].)

For S24 the dipole mode appears to redshift already after first laser exposure with 8  $\mu$ W, without significant change in the peak scattering intensity (Figure 5.13 a). The DF spectra measured after each exposure show that the dipole mode (peak maxima marked by red dots) continues to redshift along with declining peak intensity as the laser is ramped to higher powers (Figure 5.13 a, black line). After the fifth exposure with about 170  $\mu$ W, the dipole mode has shifted beyond 800 nm and the intensity has dropped noticeably compared to the initial value, so much so that it is barely visible. Hence, the DF spectra are only analyzed up to the power where the intensity of the BDP mode becomes extremely low (Figure 5.13 a, green dot). Comparing the initial and the final spectra, the laser induced change becomes evident (Figure 5.13 a, bottom panel). The higher order dipole mode has also red shifted to 650 nm with an increase in peak intensity. Upon further increase of laser power the spectrum suddenly blueshifts (above 270  $\mu$ W), indicating the formation of a localized conductive bridge between the AuNS and the mirror underneath.

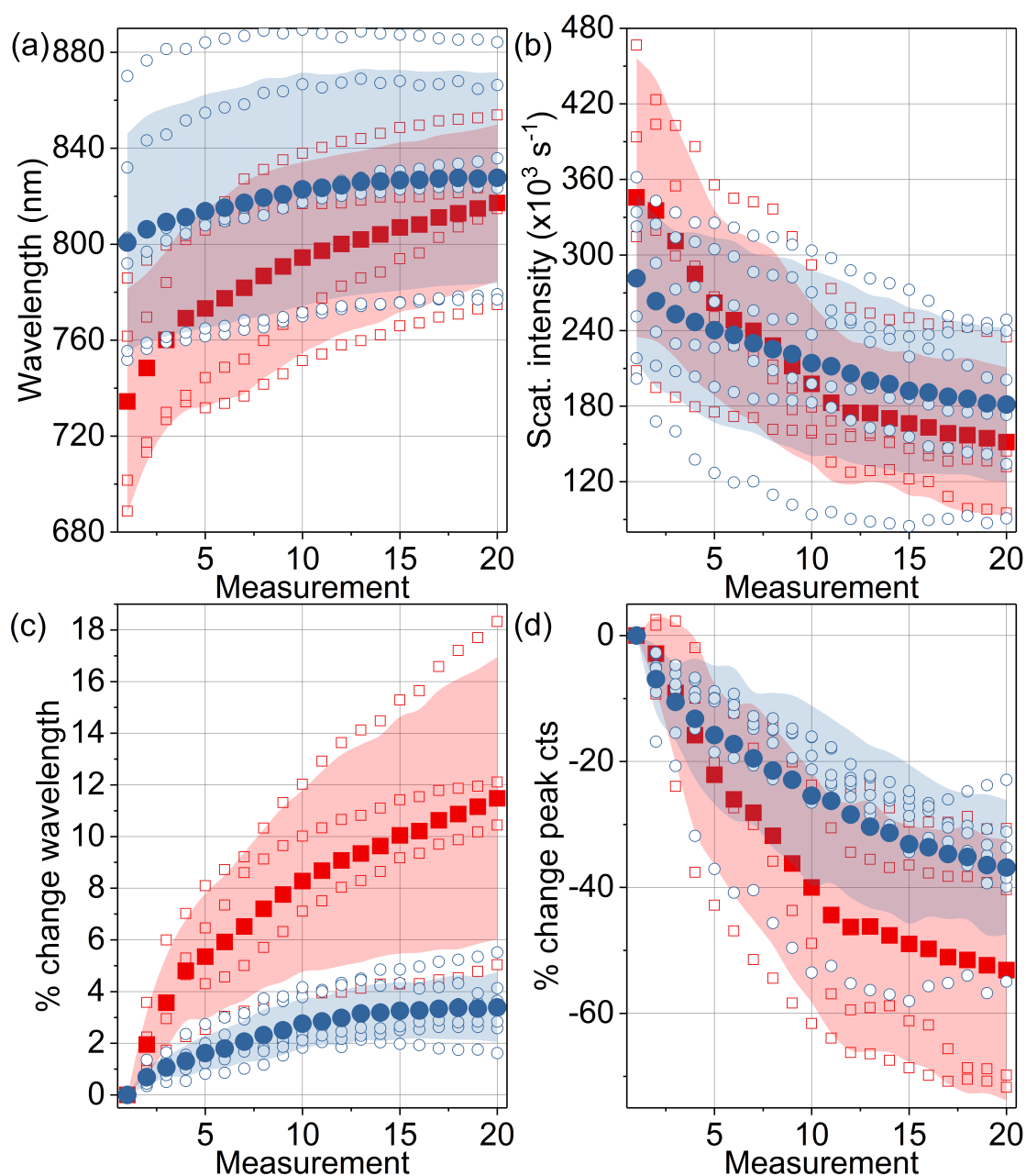


Figure 5.12: Repetitive exposure of multiple S2 (red) and S24 (blue) NPoMs with constant laser power  $12 \mu\text{W}$  at  $632 \text{ nm}$ . The repeated exposures cause a redshift in the peak wavelength of the dipole mode (**b**) along with a decrease in the scattering intensity (**b**). The percentage of the relative change in the position (**c**) and intensity (**d**) compared to the initial values are also depicted. The measured values are presented using unfilled symbols, while the average and the standard deviation are shown with filled symbols and the shaded regions respectively. The two different SAM layers were prepared by incubating the mirror substrates for 2 (S2) and 24 hours (S24) in BPT solution.



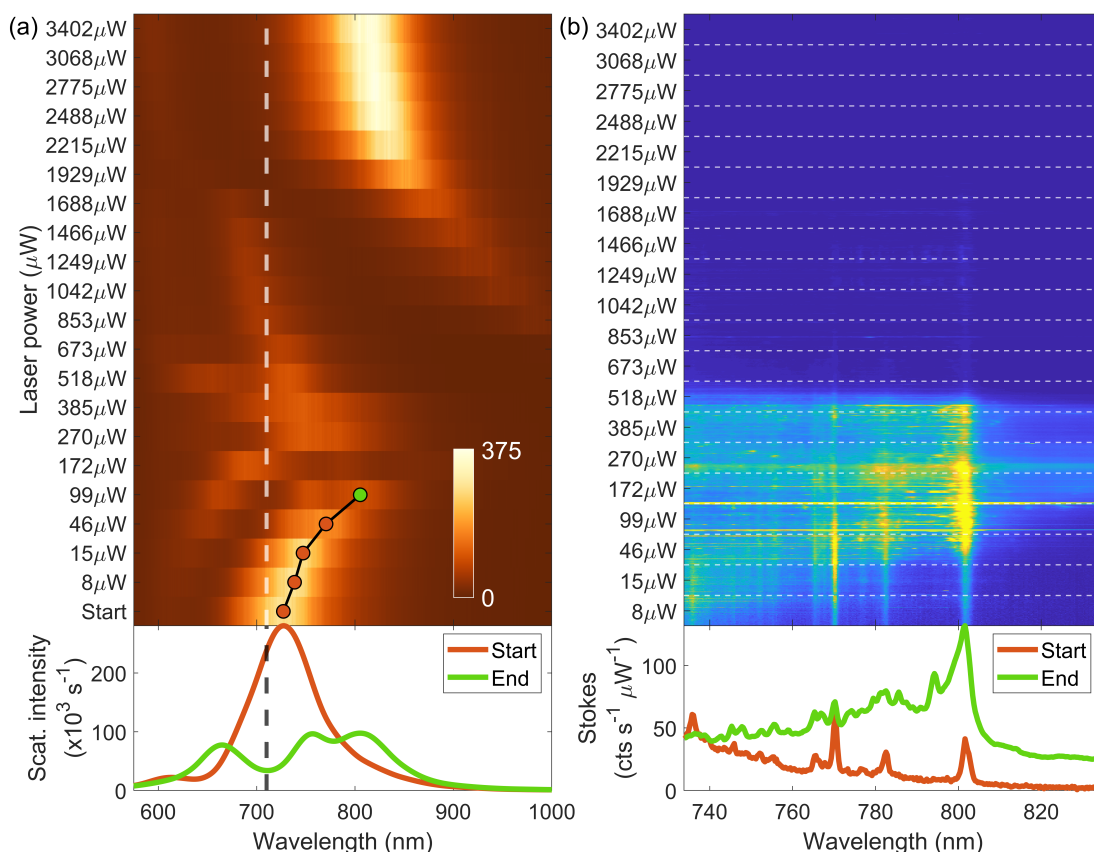


Figure 5.13: **(a)** The colorplot shows the evolution of S24 NPoM DF spectra as the laser power is increased. The laser line at 710 nm is indicated by the dashed white line. The peak position and the redshift of the dipole mode are indicated by a red dot and a black line respectively. The green dot indicates the last power for which the DF spectrum was easily observed before blueshifting. The DF spectrum at this point is compared to the initial DF spectrum in the bottom panel showing that the dipole mode has shifted to approx. 820 nm from approx. 720 nm with a significant decrease in amplitude. The high order dipole mode initially at approx. 600 nm also redshifted to approx. 680 nm with an increase in intensity. At high laser powers the dipole mode is found to blueshift indicating the formation of bridge between AuNS and the mirror and finally fusing together. **(b)** The colorplot shows the Stokes sideband of the Raman signal. The dashed white line indicate the transition from one laser power to the other. The Raman spectra are highly unstable with large shifts to the background as well as the Raman peaks however the signal disappears after the bridging of the gap. The average initial and final (99  $\mu\text{W}$ ) Raman spectra indicate the degradation in the molecular structure during exposure.

Finally, the molecules within the nanogap are completely removed and the AuNS is completely fused with the mirror [148]. The Stoke sideband of the Raman spectra also varies as BDP mode redshifts (Figure 5.13 b). This can be observed by analyzing the background the Raman peaks. Other exotic effects such as flares [149]; sudden increase in the overall Raman background, and picocavities [11]; increase in Raman peaks along with emergence of new Raman lines, also occur especially when the BDP overlaps with the Stokes peaks. The formation of the bridge

between the AuNS and the mirror drastically decreases the Raman signal. However, it is only after the complete fusion of the AuNS and the mirror that no Raman signal could be observed. The average Raman signal at 8  $\mu\text{W}$  (red) and 99  $\mu\text{W}$  (green) show deterioration of the molecules in the SAM (Figure 5.13 b, bottom panel). (The text in this paragraph is extracted from [81].)

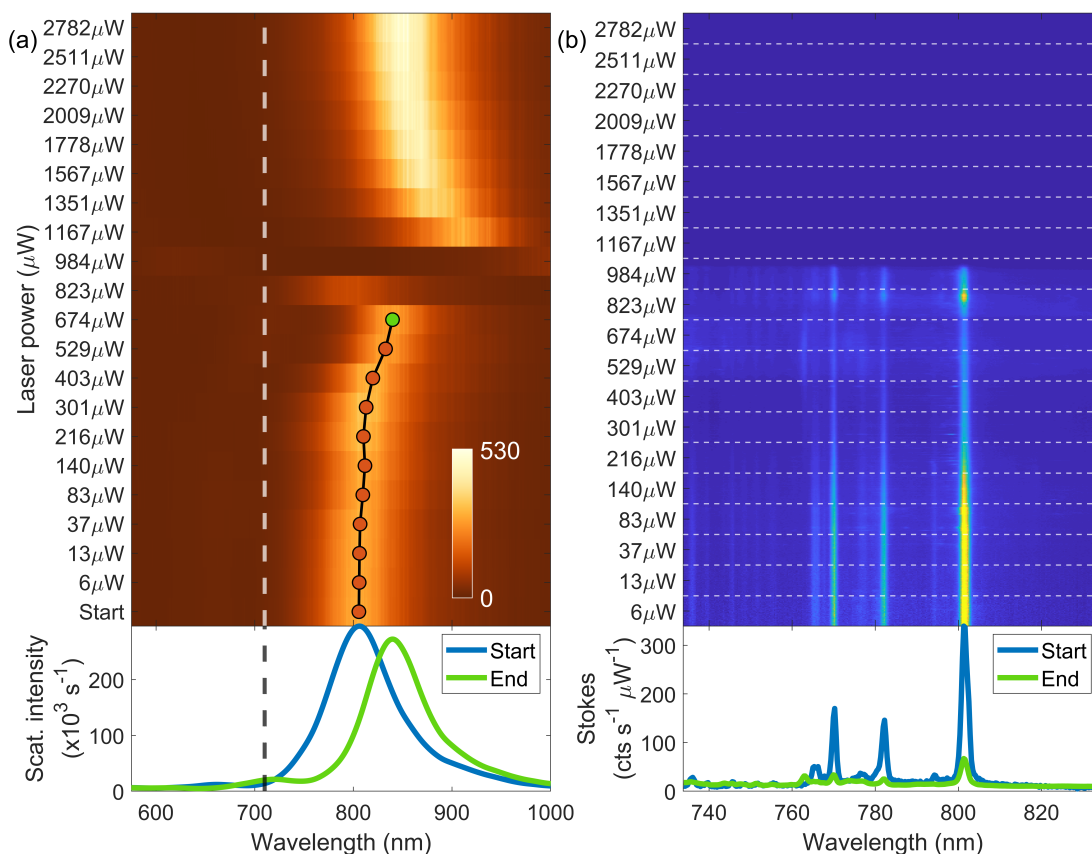


Figure 5.14: **(a)** The colorplot shows the evolution of S2 NPoM DF spectra as the laser power is increased. The laser line at 710 nm is indicated by the dashed white line. The peak position and the redshift of the dipole mode are indicated by a red dot and a black line respectively. The green dot indicates the last power for which the DF spectrum was easily observed before blueshifting. The DF spectrum at this point is compared to the initial DF spectrum in the bottom panel showing that the dipole mode has shifted to approx. 830 nm from approx. 790 nm with no significant decrease in amplitude. The high order dipole mode initially at approx. 650 nm also redshifted to approx. 700 nm with a small increase in intensity. At high laser powers the dipole mode is found to blueshift indicating the formation of bridge between AuNS and the mirror and finally fusing together. **(b)** The colorplot shows the Stokes sideband of the Raman signal. The dashed white line indicate the transition from one laser power to the other. The Raman spectra are very stable and disappears after the bridging of the gap. The average initial and final (674  $\mu\text{W}$ ) Raman spectra indicate the no degradation in the molecular structure during exposure.

The evolution is quite different for the NPoMs on S2, which is the sample with disordered SAM with lying-down molecules. In the example shown in 5.14 a, the dipole mode is initially located around 800 nm (blue line in lower panel) and does not appear to red shift as readily as observed for

S24 when the laser power is increased. The peak intensity also remains unchanged as measured after each exposure. It is only after laser powers greater than 400  $\mu\text{W}$  that a significant redshift and a decrease in intensity of the dipole mode are observed. Bridge formation followed by fusion of AuNS to the mirror similar to that observed for S24 occurs at even higher powers. The Raman spectra show a stable signal without any flare or picocavities. The overall strength of the Raman signal was found to be higher than that on S24. This could be attributed to the overlap of the dipole mode with the Raman lines. The decrease in the Raman signal occurs at a much smaller laser power than the shift of the dipole mode. As the gap between the AuNS and the mirror is bridged and finally filled, the Raman signal is lost as well. The average Stokes peaks (Figure 5.14 b, bottom panel) at the start (6  $\mu\text{W}$ : blue) and the end (674  $\mu\text{W}$ : green), show only decrease of the Raman signal without any degradation. (The text in this paragraph is extracted from [81].)

Multiple NPoMs across S24 and S2 studied with the same procedure disclose the distinct and layer dependent evolution of the dipole mode with increasing laser power, as presented in Figure 5.15. The unfilled red squares (blue circles) indicate individual NPoMs on S24 (S2) while the red (blue) shaded region shows the spread of the standard deviation centered at the mean (shaded blue circle and shaded red square). The initial value are higher by the yellow region. Differences in the SAM ordering across the substrate result in inhomogeneous layer height and contribute to the spread in resonance position, together with the distribution of shape and size of the nanoparticles. As the laser power is progressively increased, the NPoMs on S24 show a prompt redshift of the dipole mode while the NPoMs on S2 are stable up to powers above 300  $\mu\text{W}$ , after which they display a significant redshift too (Figure 5.15 a). In term of intensity of the dipole mode, the S24 NPoMs show a quick drop while S2 NPoMs remain stable (Figure 5.15 b). Thus it is evident that the NPoM cavities formed on top of a disordered and loosely packed SAM, obtained with short incubation time (S2), retain their pristine optical and plasmonic properties for laser powers that are an order of magnitude larger than what NPoMs formed on a more ordered and densely packed monolayer (S24) can sustain. A clearer representation of the difference between the two SAMs is achieved by visualizing the percentage difference from initial values (Figure 5.15 c, d). This observation is a central result, which was not anticipated and should become a precious guide for future optimization of plasmonic nanocavities in view of their diverse applications. (The text in this paragraph is extracted from [81].)

The quantitative analysis of the Raman signals was not performed as it would require understanding the interplay between the position and amplitude of the BDP mode, the EM field enhancement and the Raman spectra. In this work, the objective is to investigate the cause of this difference between the two SAMs and using the Raman only to check the state of the molecules.

## 5.7 Measurements on NPoMs with functionalized nanoparticles

The behavior of NPoMs on S2 and S24 observed during the previous experiments at constant powers and power sweep were bench marked against several other test samples. First, in order to understand the effect of Au adatoms and restructuring of the mirror surface during incubation,

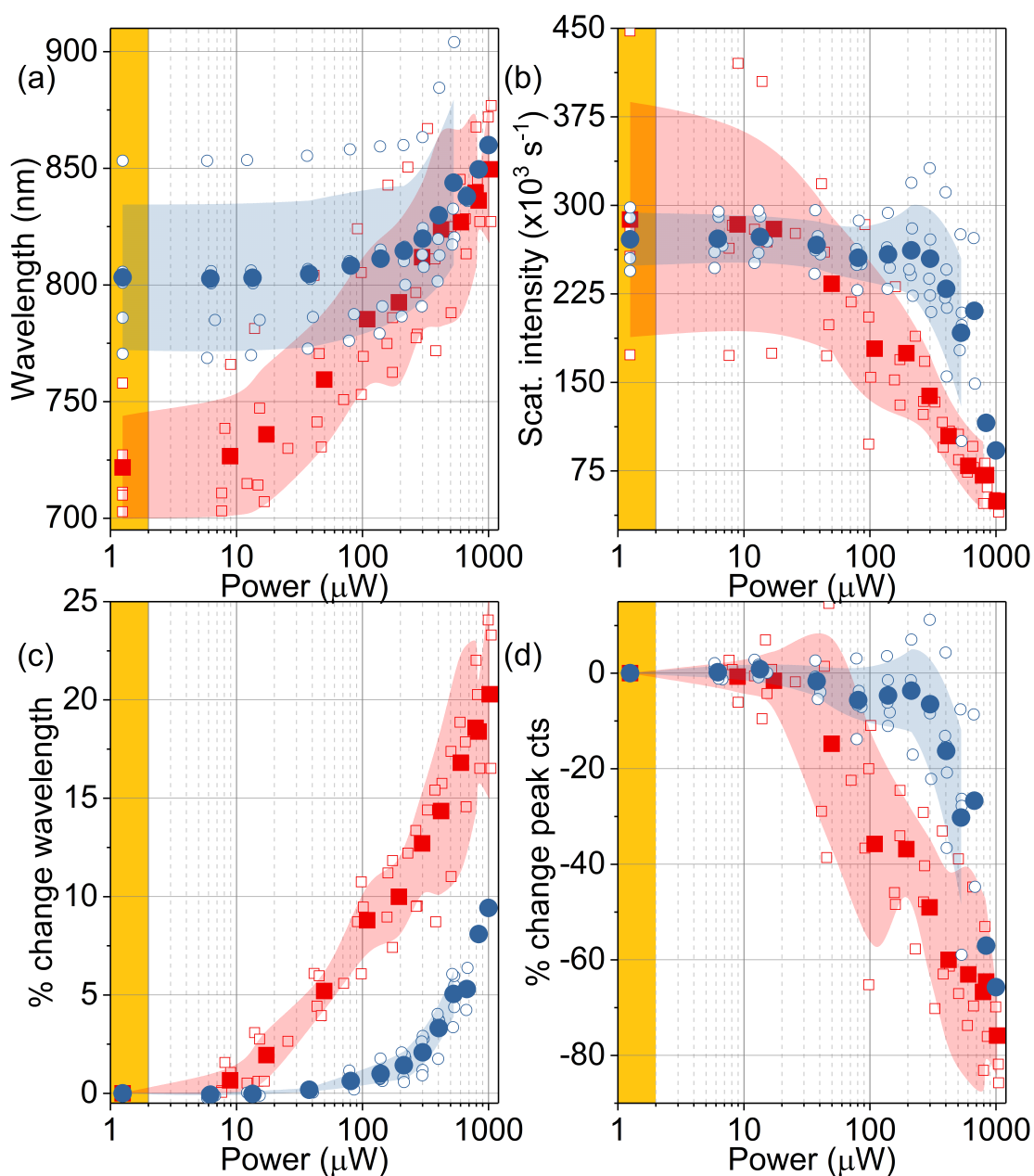


Figure 5.15: Exposure of multiple S2 (red) and S24 (blue) NPoMs with increasing laser power at 710 nm. The exposures cause a redshift in the peak wavelength of the dipole mode **(a)** along with a decrease in the scattering intensity **(b)**, however the S2 appears to withstand larger power than S24. The percentage of the relative change in the position **(c)** and intensity **(d)** compared to the initial values are also depicted. The measured values are presented using unfilled symbols, while the average and the standard deviation are shown with filled symbols and the shaded regions respectively. The two different SAM layers were prepared by incubating the mirror substrates for 2 (S2) and 24 hours (S24) in BPT solution.

AuNS functionalized with BPT were used to form NPoMs by simply drop-casting on the mirror (see Chapter 3). The experimental conditions for measurements on these NPoMs were kept similar to the previous experiments. The results from experiments with constant laser powers using 632 nm and 710 nm are shown together in Figure (5.16). The initial position of resonance of all the NPoMs is greater than 700 nm indicating the absence of multiple molecular layer; which if present would have increased the gap between the AuNS and the mirror resulting in blueshift of the dipole mode below 700 nm. The initial spread of mode position however indicates significant variation of the molecular orientation on the surface of the AuNS. The change in the location is almost half while the change in height of the dipole mode of the NPoMs repeatedly exposed to 632 nm (violet, square) is almost similar that obtained earlier with 632nm on S24 NPoMs. The exposures to 710 nm (orange, circle) at constant power yield surprising results with almost no change in the height or position of the dipole mode.

The power dependence on these NPoMs was measured along with two other. The first sample was prepared with unfunctionalized AuNS over the mirror with approximately 1nm thick layer of alumina ( $\text{Al}_2\text{O}_3$ ) in between (ALD-NPoMs). The alumina layer was deposited on patterned, template stripped Au substrates via atomic layer deposition (ALD) using tri-methyl aluminum (TMA) and water ( $\text{H}_2\text{O}$ ) as precursor. The extremely stable nature of such layer makes ALD based NPoMs ideal to quantify the effects of laser exposure on the nanoparticle shape and morphology. Moreover, the effect of citrate molecules, typically present on the surface of commercial nanoparticle to avoid agglomeration, can be observed. The second sample is also based on an ALD gap but in this case, the surface of AuNS is functionalized with BPT (BPT-ALD-NPoMs). This sample would mimic similar geometry as the first but with BPT instead of citrate.

The results from power dependence experiments highlight the individual response of the three samples. The initial positions of the dipole mode for ALD-NPoMs ( $\circ$ ) and BPT-ALD-NPoMs ( $\square$ ) are comparable to those observed using SAM based NPoMs with longer incubation time, evidencing the similarity in gap height (Figure 5.17 a). On the other hand, the NPoMs with functionalized AuNS without ALD have a redshifted dipole mode ( $\triangle$ ). The initial scattering intensity is quite different for the three samples with the sample with no ALD scattering less than those prepared with ALD (Figure 5.17 b). This difference can be attributed to the insulating nature of alumina, which stops the charges from tunneling through the gap. The slightly higher intensity observed for BPT-ALD-NPoMs compared to ALD-NPoMs could be due to a slight increase in gap height by BPT SAM on AuNS. Another plausible explanation could be that the impedance of citrate molecules at optical frequencies is lower than that of BPT, hence increasing the tunneling of charges and decreasing the scattering intensity. The power dependence measurements induce very small changes in NPoMs with ALD compared to those without. The dipole mode in ALD-NPoMs and BPT-ALD-NPoMs show a small redshift (Figure 5.17 c) at laser power exceeding 100  $\mu\text{W}$ , with the former shifting a bit further than the latter. This along with the corresponding changes in peak amplitude suggest molecular reorganization. Most commercial nanoparticles, such as the ones used here, are covered with citrates to prevent agglomeration. The citrate are weakly bound to the surface of AuNS and easily displaced when the nanoparticle is placed in the vicinity

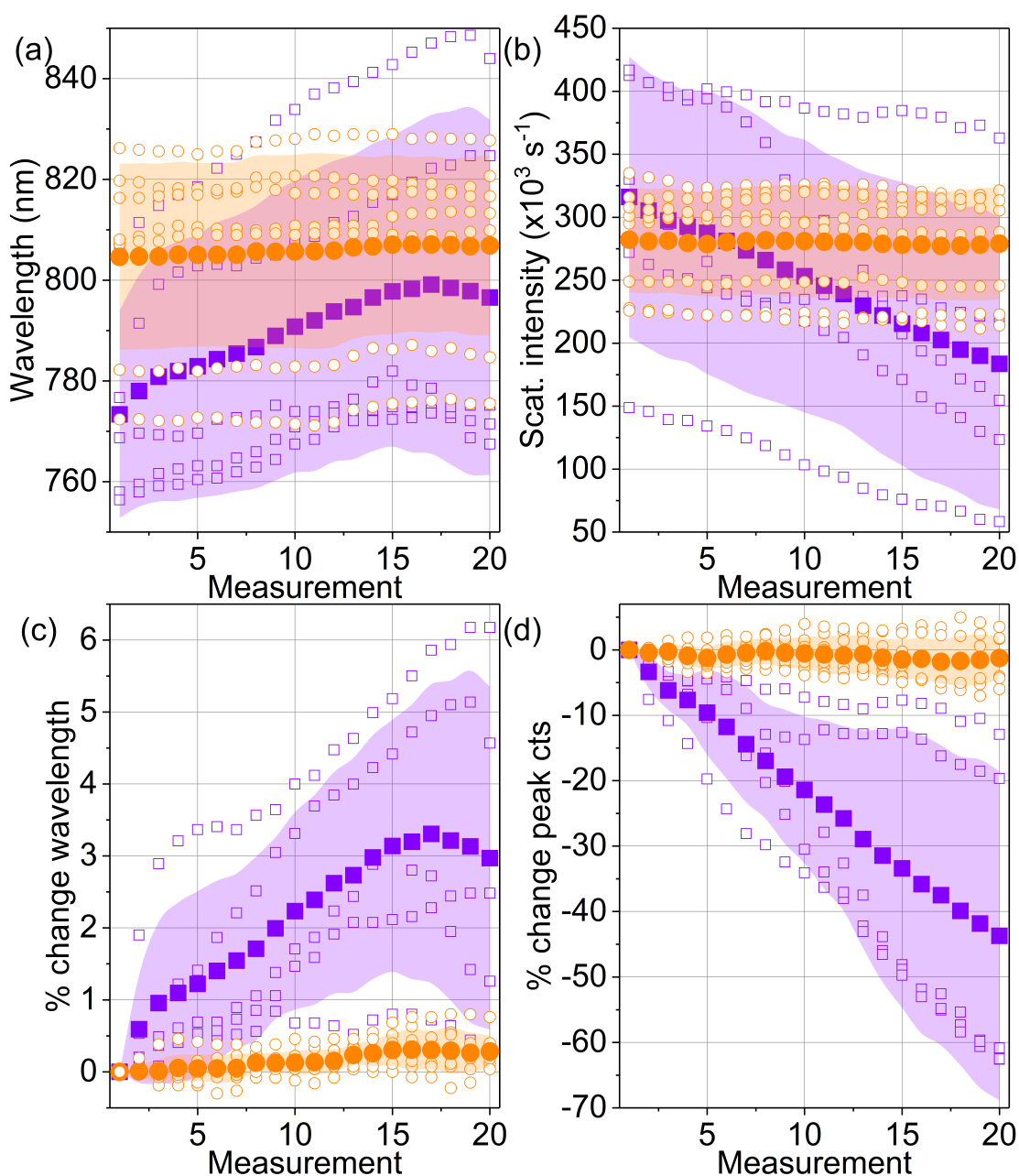


Figure 5.16: Multiple exposures of BPT functionalized AuNS with constant laser power  $12 \mu\text{W}$  at 632 nm (violet) and 710 nm (orange). The peak wavelength of the dipole mode (b) along with the scattering intensity (b) showing a stronger change with 632 nm. The percentage of the relative change in the position (c) and intensity (d) compared to the initial values are also depicted. The measured values are presented using unfilled symbols, while the average and the standard deviation are shown with filled symbols and the shaded regions respectively.

of other molecules especially thiol. An in ALD-NPoM samples there are no thiol molecules, the optically induced heating results in changes in citrate coverage, thus changing the gap and the



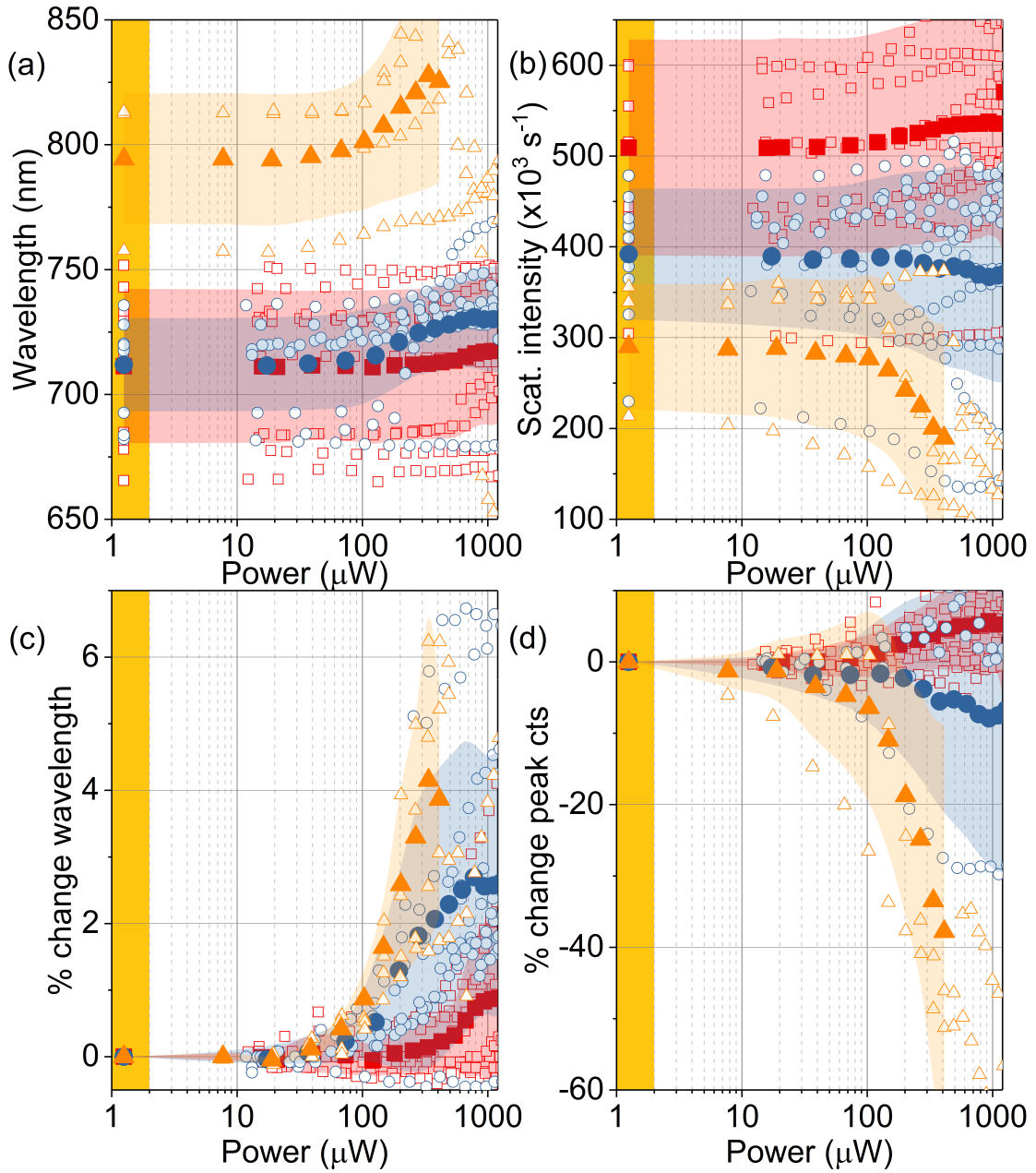


Figure 5.17: 710 nm AuNS func (yellow), ALD-NPoM (blue), ALD-BPT-NPoM (red). Exposure of multiple NPoMs with increasing laser power 12  $\mu\text{W}$  at 710 nm. The different NPoMs used consist of functionalized AuNS (yellow), ALD-NPoM (blue), ALD-BPT-NPoM (red). The exposures cause a redshift in the peak wavelength of the dipole mode **(b)** along with a decrease in the scattering intensity **(b)**. The percentage of the relative change in the position **(c)** and intensity **(d)** compared to the initial values are also depicted. The measured values are presented using unfilled symbols, while the average and the standard deviation are shown with filled symbols and the shaded regions respectively.

BDP mode. This effect is supported by the large fluctuation of the citrate Raman signal during exposure (Appendix A.1). In case of BPT-ALD-NPoMs, the BPT molecules are covalently bonded to the Au atoms and are hard to desorb. While thermally driven rearrangement of thiols may occur leading to different phases [150], unfortunately these have not been characterized on nanoparticles surfaces. In comparison to the ALD samples, the evolution peak position in NPoMs without ALD with functionalized AuNS is quite similar to that observed for S2 (Figure 5.17) although the peak amplitude is quite different. Thus far, it is clear that the adatoms moieties that would be present in abundance during the self-assembly of BPT on mirror surface do not contribute significantly to the difference observed between the two incubation times.

### 5.8 Measurements on NPoMs with conductive spacer

The charge tunneling behavior of the SAM layers was also investigated using molecules to form a conductive contact between the AuNS and the mirror surface. This was achieved by simply incubating the substrates in a solution of biphenyl-4,4'-dithiol (BPDT). The incubation was performed with the same procedure as used earlier to form BPT SAM. The BPDT molecule has been studied extensively for its electrical properties [151] and contains two thiol groups with one as the head and the other as the tail. This feature can be used to form a covalent bond between the AuNS and the SAM molecules thus allowing charges to pass through the molecule with minimal impedance due to the interaction between the  $\pi$ - $\pi$  bonds of the two benzene rings [152]. This is unlike the case with BPT molecules used earlier, as BPT SAM on mirror do not possess another thiol functional group to bind to the AuNS.

The behavior of the BPDT SAM layers was analyzed once again by preparing samples with short (2 hour) and long (25 hours) incubation times and exciting them through multiple exposures at constant powers and power dependence measurements. The results from illumination with constant power are 632 nm and 710 nm are shown in Figure 5.18 and Figure 5.19 respectively. Repeated exposure of S2 NPoMs to 632 nm lead to rapid redshift and decrease in amplitude of the BDP mode (fig 5.18 a, b). Surprisingly the S24 NPoMs do not change so dramatically when compared to S2 (fig 5.18 c, d). One proposed explanation for this effect is that in case of S24, the conductive SAM between the AuNS and the mirror does not allow excessive EM field enhancement leading to a stable NPoM. However, the SAM in S2 NPoM is not properly bonded to the AuNS due to its lying-down configuration and thus can enable a much higher EM field enhancement leading to poor stability of the NPoM. While this hypothesis would explain the behavior of S2 and S24 when exposed to 632 nm (Figure 5.18), it does not explain the opposite trends with observed using 710 nm (Figure 5.19). The S2 clearly behaves differently when illuminated with 710 nm, showing very low changes in the peak position and amplitude of the BDP mode (Figure 5.19 c, d) while the S24 responds in a manner similar to 632 nm exposure.

The second explanation to address the strange trends of S2 NPoMs using 632 nm along with their contrary response when using 710 nm can be explained by overlap of the laser line with the higher order dipole mode ( $l_2$ ) Figure 5.19. The scattering intensity of this mode, although

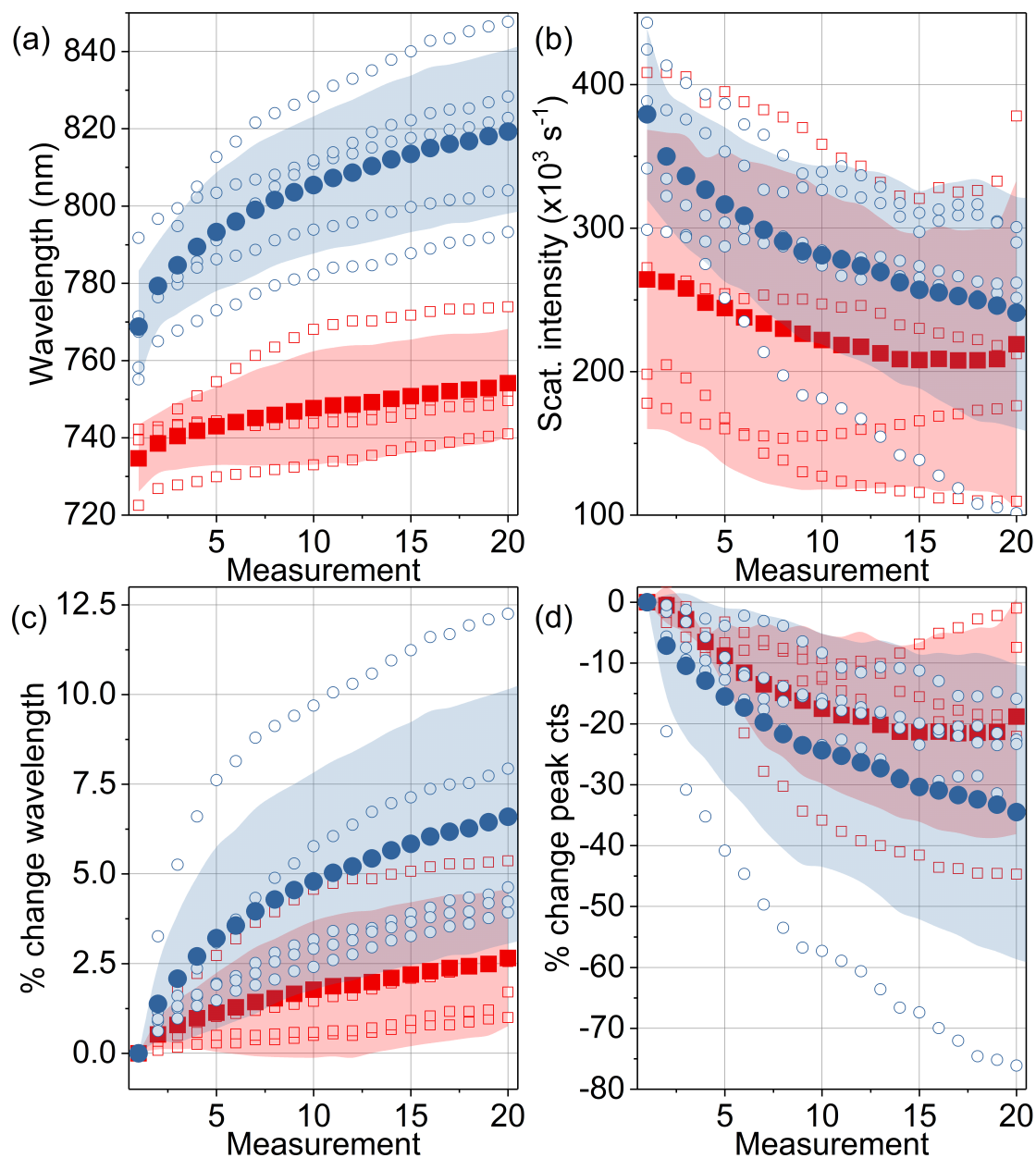


Figure 5.18: Repetitive exposure of multiple S2 (red) and S24 (blue) NPoMs with constant laser power  $12 \mu\text{W}$  at  $632 \text{ nm}$ . The repeated exposures cause a redshift in the peak wavelength of the dipole mode (b) along with a decrease in the scattering intensity (b). The percentage of the relative change in the position (c) and intensity (d) compared to the initial values are also depicted. The measured values are presented using unfilled symbols, while the average and the standard deviation are shown with filled symbols and the shaded regions respectively. The two different SAM layers were prepared by incubating the mirror substrates for 2 (S2) and 24 hours (S24) in BPD solution.

still lower than the BDP mode, was found to be much higher in BPD NPoMs than BPT NPoMs

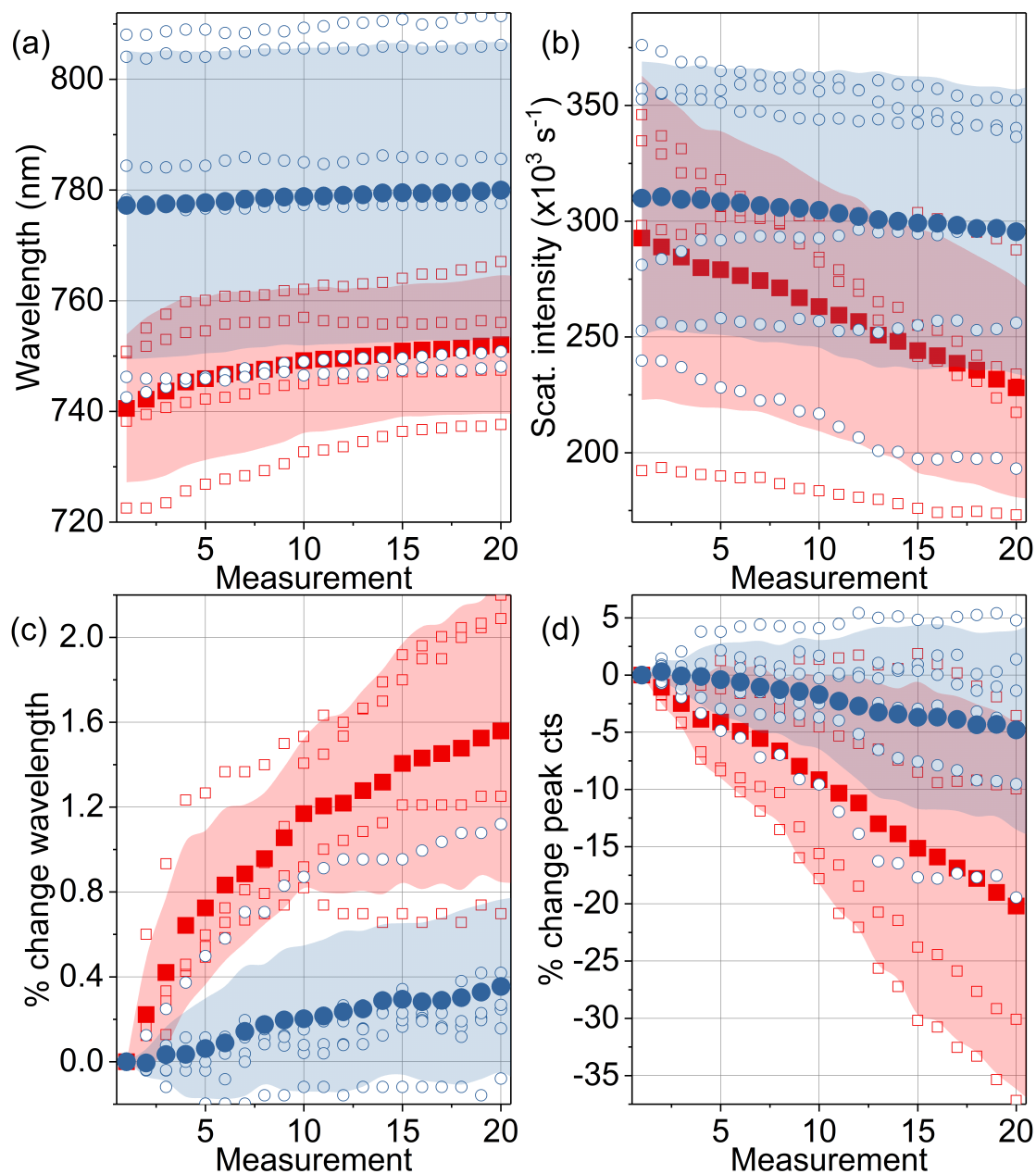


Figure 5.19: Repetitive exposure of multiple S2 (red) and S24 (blue) NPoMs with constant laser power  $12 \mu\text{W}$  at  $710 \text{ nm}$ . The repeated exposures cause a redshift in the peak wavelength of the dipole mode **(b)** along with a decrease in the scattering intensity **(b)**. The percentage of the relative change in the position **(c)** and intensity **(d)** compared to the initial values are also depicted. The measured values are presented using unfilled symbols, while the average and the standard deviation are shown with filled symbols and the shaded regions respectively. The two different SAM layers were prepared by incubating the mirror substrates for 2 (S2) and 24 hours (S24) in BPDT solution.

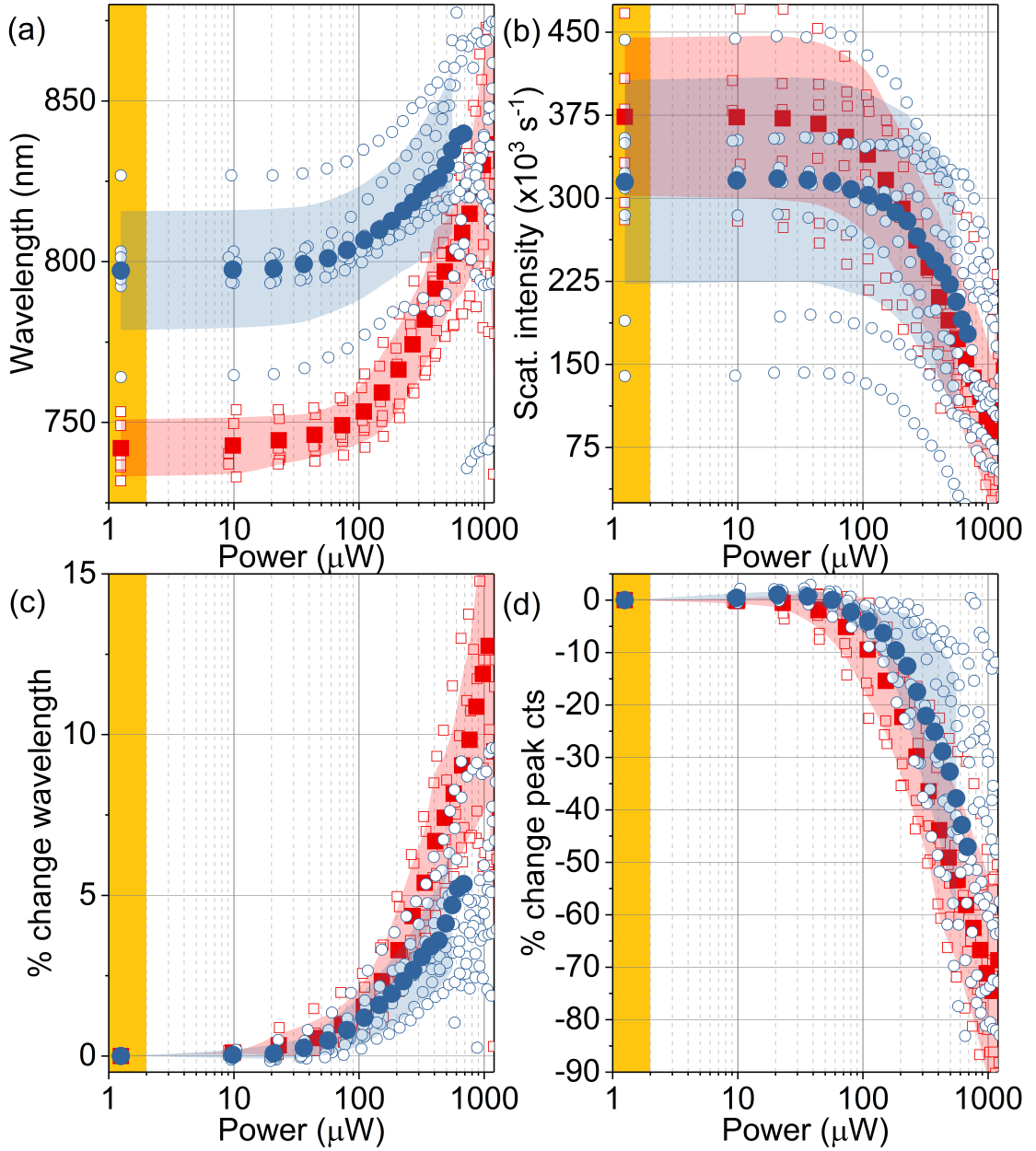


Figure 5.20: Exposure of multiple S2 (red) and S24 (blue) NPoMs with increasing laser power at 710 nm. The exposures cause a redshift in the peak wavelength of the dipole mode **(b)** along with a decrease in the scattering intensity **(b)**, however the S2 appears to withstand larger power than S24. The percentage of the relative change in the position **(c)** and intensity **(d)** compared to the initial values are also depicted. The measured values are presented using unfilled symbols, while the average and the standard deviation are shown with filled symbols and the shaded regions respectively. The two different SAM layers were prepared by incubating the mirror substrates for 2 (S2) and 24 hours (S24) in BPDT solution.

(Appendix A.2). However, the field enhancement of ( $l_2$ ) mode is found to be comparable to that

of the BDP mode [33]. The typical peak position of ( $l_2$ ) mode for BPDT NPoMs are found to be located between 600 nm-700 nm. Hence, when the NPoMs are excited with 632 nm the EM field within the nanocavity is much larger than 710 nm excitation, resulting in a faster change of the BDP mode using 632 nm. The S24 NPoM, are able to reduce this EM field due to the conductive nature of BPDT while the S2 NPoMs have no such connection, and so the changes are more pronounced in S2 NPoMs. The power dependence measurements performed using 710 nm on S2 and S24 NPoMs with BPDT SAM (Figure 5.20) support the second explanation. As the laser power is gradually increased, the changes to the S2 and S24 occur very closely at similar laser power unlike the difference observed using BPT-SAM (Figure 5.15). The S24 NPoMs with BPDT are able to bear higher powers in comparison to their BPT counterparts. The similarity between S2 and S24 BPDT NPoMs in power dependence hints towards the discrepancy between the DF spectra and the field enhancement within the nanocavities.

### 5.9 Measurement on NPoMs with Au nanocubes (AuNCs)

In order to investigate the effect of the nanoparticle shape on the stability of the NPoM structures, NPoMs were prepared using Au nanocubes (AuNC) as the nanoparticle. The preparation of these samples simply involved switch the AuNS with AuNC during the drop-casting. The gap layer for the experiments with AuNC was prepared by incubation of the mirror in the solution of BPT. Once more, to study the effect of incubation time, the mirrors were incubated for two different times (2 hours and 24 hours). The plasmonic modes and the corresponding EM field confinement are very different within the previously studied AuNS and the AuNC structures [79, 153]. Therefore, the comparison between two incubation times on samples with different plasmonic properties could help underpin the effect of plasmonic modes within the nanogap on the stability of NPoM structures.

Once again, the experiments were performed with constant laser power using 632nm and 710 nm laser wavelengths under conditions similar to the previous experiments. The initial position of the dipole mode is quite comparable to those obtained previously using AuNS. The results with 632 nm (Figure 5.21) show a trend similar to that observed on S2 and S24 NPoMs with AuNS, however the magnitude of the changes is slightly smaller than before. In case of 710nm (Figure 5.22), both the S2 and S24 NPoMs evolve alike to one another, with negligible changes in the position and peak height of the BDP mode. Compared to the modification of the BDP mode observed with AuNS as the nanoparticle, the AuNC based NPoMs seem very stable. This stability could be explained due to the increase in the lateral gap size when switching from AuNS to AuNC. The larger interaction region between the mirror and the nanoparticle in the NPoM leads to broader nearfield distribution and hence an overall less intense EM field. This decrease in the EM field thus allows the AuNC NPoMs to tolerate multiple laser exposures. Larger changes due to 632 nm (Figure 5.21 c, d) are still observed when compared to 710 nm (Figure 5.22 c, d). This is attributed to the position of the  $l_2$  mode in AuNC NPoMs. The  $l_2$  mode in case of S24 NPoMs was found to be present closer to 632 nm while the  $l_2$  mode for S2 NPoMs was further away at higher wavelengths (Appendix A.3). The power dependence measurements performed with 710



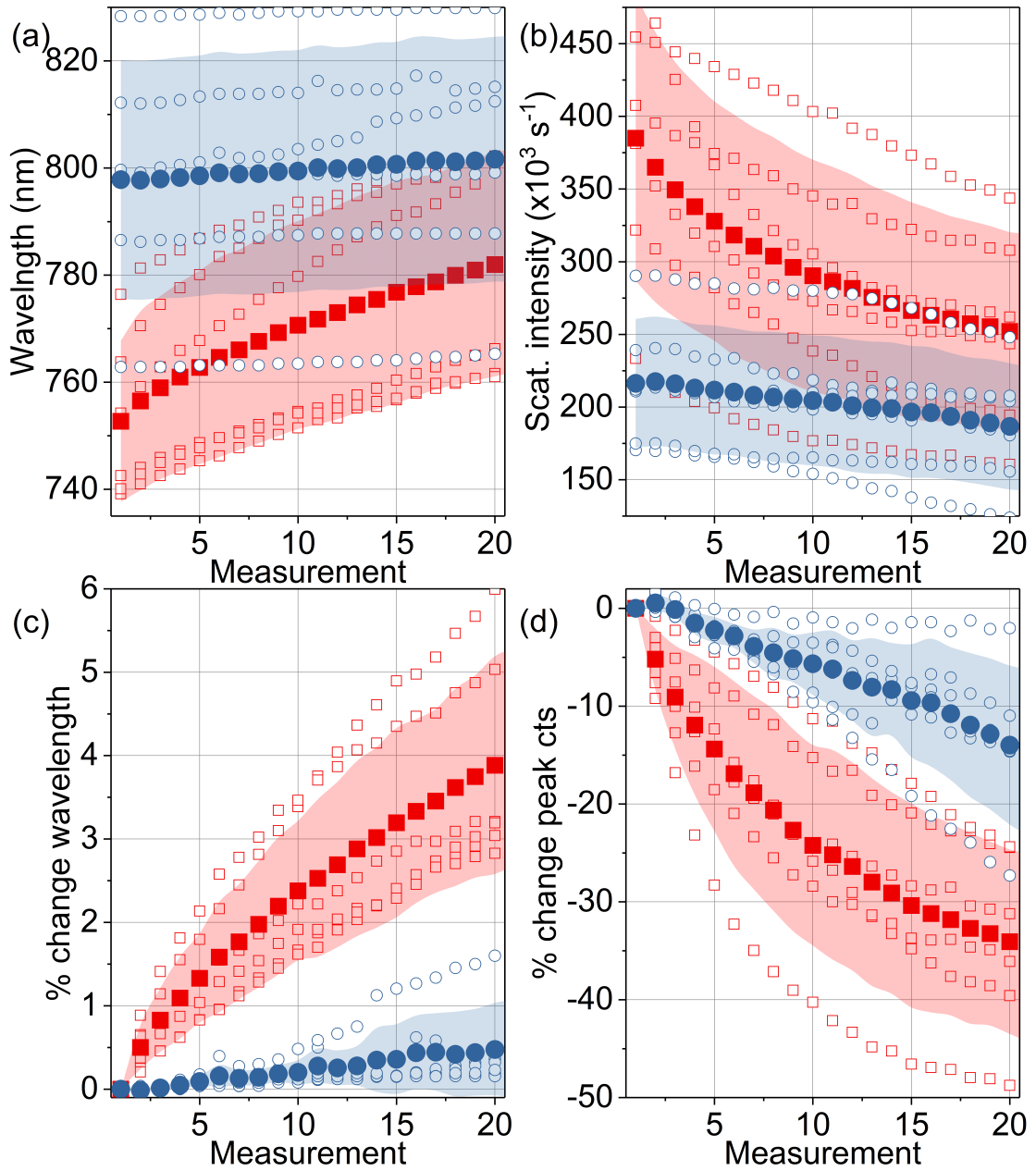


Figure 5.21: Repetitive exposure of multiple S2 (red) and S24 (blue) NPoMs with constant laser power  $12 \mu\text{W}$  at  $632 \text{ nm}$ . The repeated exposures cause a redshift in the peak wavelength of the dipole mode (b) along with a decrease in the scattering intensity (b). The percentage of the relative change in the position (c) and intensity (d) compared to the initial values are also depicted. The measured values are presented using unfilled symbols, while the average and the standard deviation are shown with filled symbols and the shaded regions respectively. The two different SAM layers were prepared by incubating the mirror substrates for 2 (S2) and 24 hours (S24) in BPT solution with AuNC as nanoparticles.

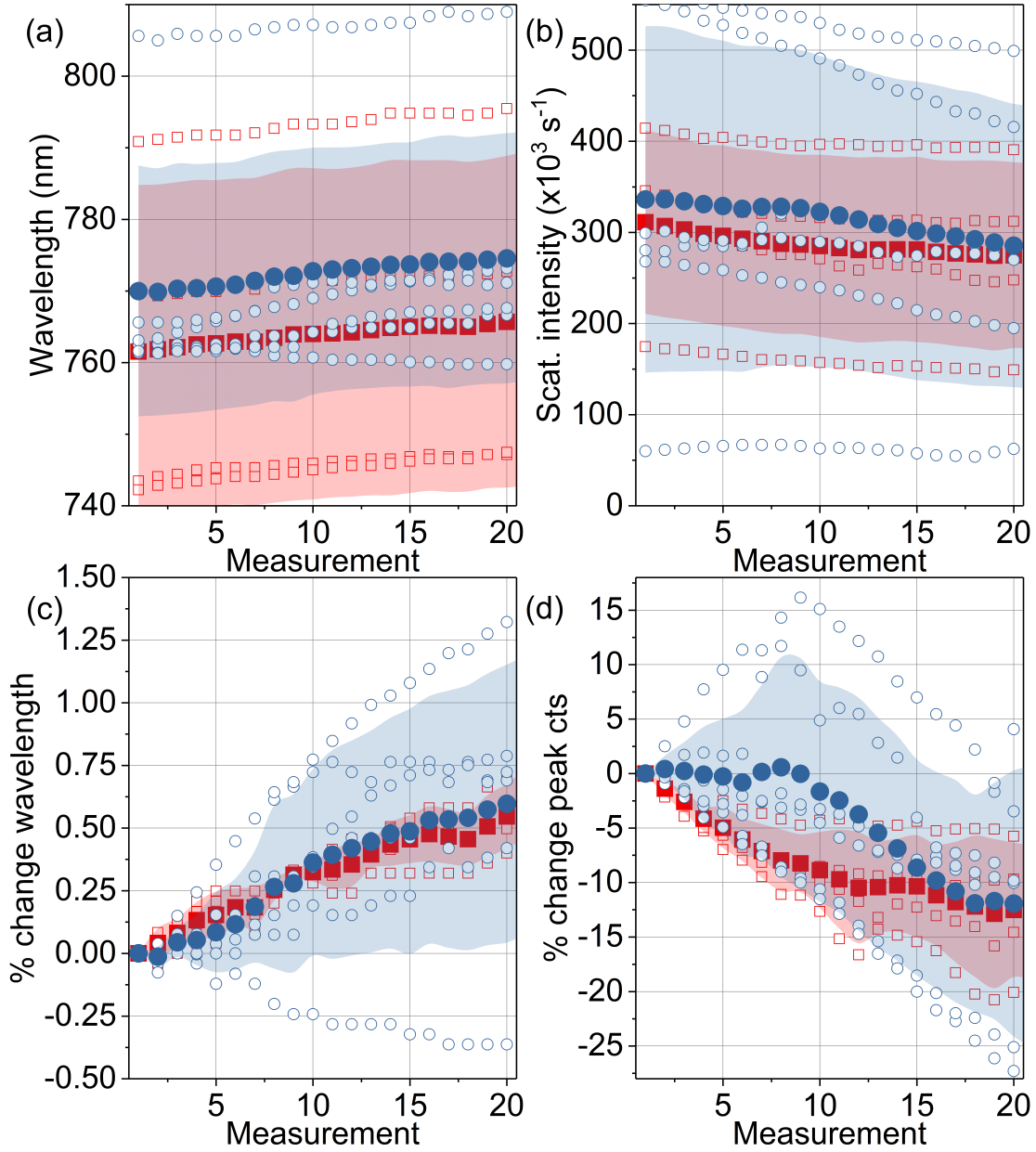


Figure 5.22: Repetitive exposure of multiple S2 (red) and S24 (blue) NPoMs with constant laser power  $12 \mu\text{W}$  at  $710 \text{ nm}$ . The repeated exposures cause a redshift in the peak wavelength of the dipole mode **(a)** along with a decrease in the scattering intensity **(b)**. The percentage of the relative change in the position **(c)** and intensity **(d)** compared to the initial values are also depicted. The measured values are presented using unfilled symbols, while the average and the standard deviation are shown with filled symbols and the shaded regions respectively. The two different SAM layers were prepared by incubating the mirror substrates for 2 (S2) and 24 hours (S24) in BPT solution with AuNC as nanoparticles.

nm (Figure 5.23) indicate that SAM layer has an impact on the stability of NPoM structure, albeit lower in magnitude than that observed earlier with AuNS (Figure 5.15). The initial values of peak

wavelength and intensity are quite similar to each other however as the laser power is increased the S2 NPoMs are able to maintain a stable response while S24 NPoMs begin to change slowly after the second exposure at approximately 20  $\mu$ W. The change in AuNC based NPoMs with the increase in laser power (Figure 5.23 c,d) is much less stark than that shown by AuNS (Figure 5.15 c, d), indicating that the EM field enhancement is a major contributor to of NPoM stability.

## 5.10 Comparing experiments and simulations

We now turn our attention to the understanding of the physical transformations underlying the changes in scattering spectra observed for S2 and S24 NPoMs. Starting with the case of BPT SAM on mirror with AuNS as nanoparticles (Figure 5.15), a number of different phenomena may occur during the laser exposure of the NPoM structure. Moreover, since the changes to the BDP mode are most pronounced during power dependence measurements, we consider the results from only those measurements for now. Limiting the study to sub-mW laser powers, we consider two physical mechanism likely responsible for the evolution of the scattering spectra: increase in facet size (Figure 5.24 a) and decrease in gap height (Figure 5.24 c). We use BEM simulations to predict the effects on DF spectra and consider these two processes independently; e.g. the facet size is gradually varied while keeping the gap size constant, and vice versa. The initial facet size of commercially available AuNS used for this study (80 nm diameter, BBI Solutions) is approximately 30 nm [32], and it was suggested that in similar systems the facet size can be irreversibly increased by sweeping the power of an incident laser [148]. To simulate the scattering spectra with different facet sizes (Figure 3b) the NPoM was modelled by placing an initially faceted AuNS above a 1.4 nm thick dielectric layer with a refractive index of 1.4. Starting from a facet diameter of 20 nm the dipole mode slightly redshifts until the facet diameter is close to 30 nm and then begins to blueshift. While the behavior of the dipole mode has been explained before [33], it clearly does not match our results. In contrast, our results match well with the scenario where the gap height gradually decreases (Figure 5.24 c). Simulating the scattering spectra of NPoM with gap height decreasing from 1.4 nm to 0.5 nm; and with constant facet size and refractive index of 30 nm and 1.4 respectively, a red shift of the dipole mode is observed, similar to our observations. In order to quantitatively compare simulations and experimental results the average initial (label i) and final (label f) positions of the dipole mode as observed on S2 (blue) and S24 (red) are plotted on top of the simulated data. The error bar represents the respective standard deviation. We conclude that, in contrast with previous reports invoking mostly the growth of facet size [148, 154], the shrinkage of the spacer layer and effective gap size is most consistent with our experimental observations and better explains the change in DF scattering spectrum caused by laser irradiation. (The text in this paragraph is extracted from [81].)

The decrease in the gap height can be explained by thermally driven reorientation of the spacer molecules during laser exposure. It has been observed before that upright and densely packed SAM layers, similar to those on S24, may develop defects and switch to a lying down configuration as the temperature is increased to 400 K [128, 133, 143, 155]. Temperatures ranging from

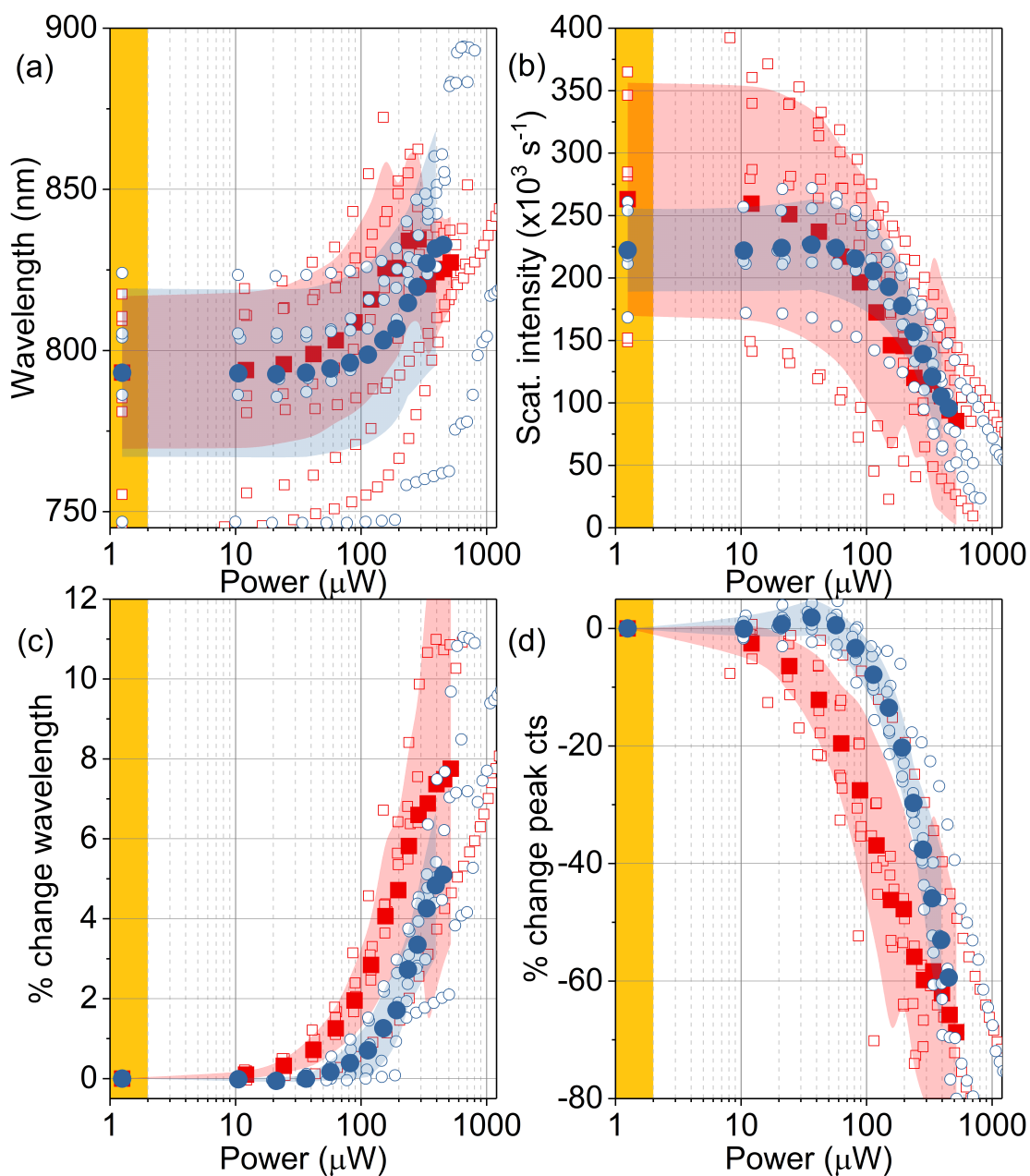


Figure 5.23: Exposure of multiple S2 (red) and S24 (blue) NPoMs with increasing laser power at 710 nm. The exposures cause a redshift in the peak wavelength of the dipole mode (b) along with a decrease in the scattering intensity (b), however the S2 appears to withstand larger power than S24. The percentage of the relative change in the position (c) and intensity (d) compared to the initial values are also depicted. The measured values are presented using unfilled symbols, while the average and the standard deviation are shown with filled symbols and the shaded regions respectively. The two different SAM layers were prepared by incubating the mirror substrates for 2 (S2) and 24 hours (S24) in BPT solution with AuNC as nanoparticle.

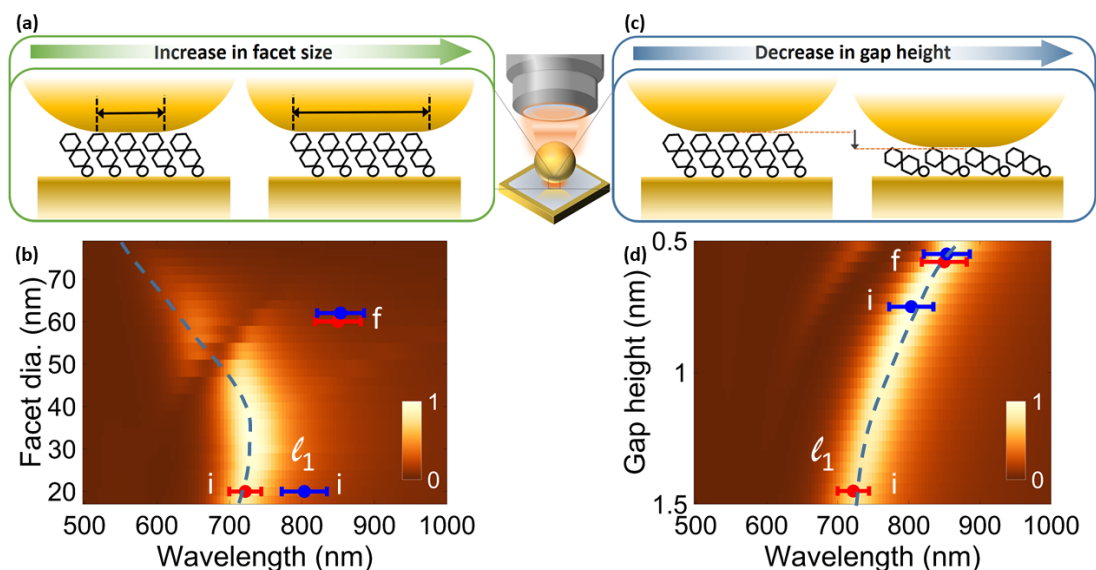


Figure 5.24: Two plausible explanations for the changes of the DF spectra from AuNS NPoMs. **(a)** The facet of AuNS may expand due to atomic migration under laser exposure; **(b)** BEM simulations show the evolution of the dipole mode  $l_1$  as the facet diameter is gradually increased with constant gap height of 1.4 nm. **(c)** Alternatively, the gap height may decrease due to molecular reconfiguration; **(d)** corresponding simulation where the gap size is swept from 0.5 nm to 1.5 nm keeping the facet size fixed at 30 nm. In both simulations the molecules were modelled as a dielectric layer with refractive index of 1.4. The experimental values for the average initial (label i) and final (label f) wavelength of the dipole mode on S24 (red symbol) and S2 (blue symbol) are shown, with their positions along the y axis adapted to match the simulations (note that it is not possible to reach a match in **(b)**). The error bars represent the standard deviation across multiple NPoMs. (Figure and caption adapted from [81].)

300 K up to a few thousand kelvin have been recorded in plasmonic nanogaps under optical excitation [156], hence making thermally-activated molecular reorientation a plausible mechanism. In case where the SAM is not densely packed, similar to S2, the molecules are already in a lying down phase [106] and hence show little changes at low laser powers. Our hypothesis implies that, as the SAM height of the NPoMs on S24 decreases it should at some point match the SAM height of NPoMs on S2, and both samples should feature similar resonance positions. We find that this statement is in good agreement with the experimental results shown in Figure 5.15. (The text in this paragraph is extracted from [81].)

A similar approach is used to described the behavior of AuNC based NPoMs on S2 and S24 (Figure 5.23). The changes in the scattering spectra are attributed to two main factor: conversion from cubic shape to a more round one (Figure 5.25 a) and decrease in gap height due to molecular reorganization (Figure 5.25 c). Once more, the average of the initial and final positions of the BDP mode observed experimentally, are overlaid on the simulated spectra for each scenario. To simulate the effect of roundness, a 75 nm AuNC was gradually transformed into a AuNS with a

diameter of 75 nm. The gap height was maintain at 1.4 nm with a refractive index of 1.4. The initial (i) and final (f) values of position measured on S2 (blue) and S24 (red) do not match well to the simulated spectra (Figure 5.25 b). If the experimental values were arranged such as to fit the simulation it would imply that the AuNC is becoming more cubic during laser exposure which is not possible [157]. On the other hand, the decrease gap height tends to mimic the experimental results very well, albeit the change between S2 and S24 is quite similar due to the similarity in the EM field within the gap (Figure 5.25 d). Thus, it is evident that the molecular reorganization is the primary reason behind the change in the scattering spectra and is greatly impacted by the EM field enhancement within the gap.

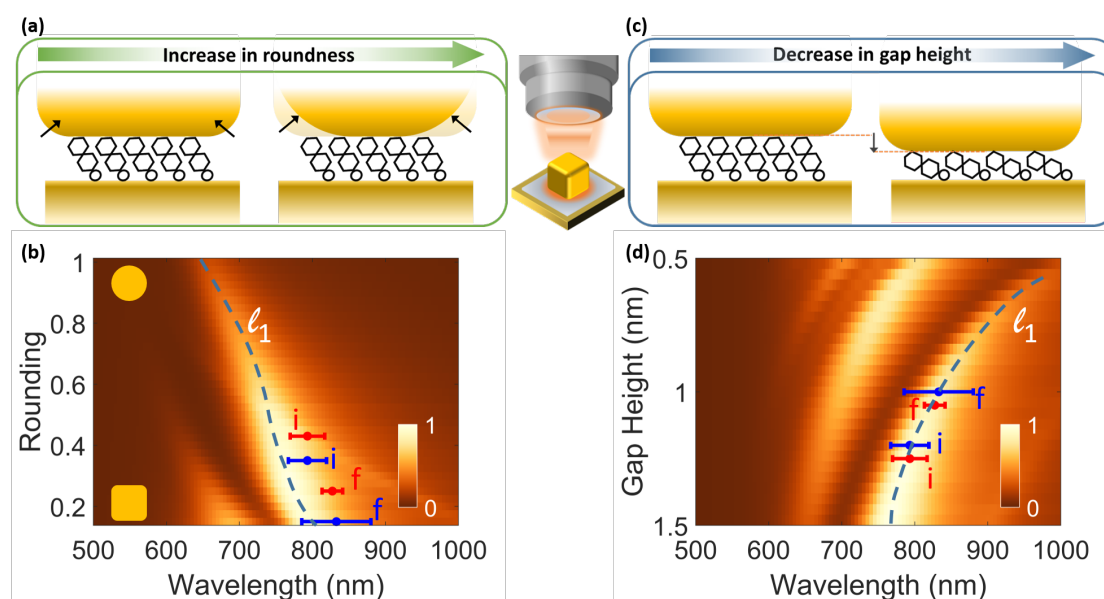


Figure 5.25: Two plausible explanations for the changes of the DF spectra from AuNC NPoMs. **(a)** The faces of the AuNC may adopt of a rounder shape under laser exposure; **(b)** BEM simulations show the evolution of the dipole mode  $l_1$  as the roundness is gradually increased with constant gap height of 1.4 nm. **(c)** Alternatively, the gap height may decrease due to molecular reconfiguration; **(d)** corresponding simulation where the gap size is swept from 0.5 nm to 1.5 nm keeping the roundness fixed at 0.25. In both simulations the molecules were modelled as a dielectric layer with refractive index of 1.4. The experimental values for the average initial (label i) and final (label f) wavelength of the dipole mode on S24 (red symbol) and S2 (blue symbol) are shown, with their positions along the y axis adapted to match the simulations (note that it is not possible to reach a match in **(b)**). The error bars represent the standard deviation across multiple NPoMs.

Our proposed explanation regarding the gap height change due to molecular reorganization is further supported by the experiment perform with BPDT, ALD NPoMs and NPoMs with SAM on the nanoparticle. The plasmonic properties of the NPoMs with BPDT SAMs are clearly different from those of BPT SAM. Nonetheless, it is evident from the power dependence measurements the magnitude of change of the BDP is related to the conductivity of the molecule. Moreover, the impact of incubation time is greatly reduced but not negligible. The experiment



on ALD NPoMs indicate that the changes observed in the scattering response originate due to changes in the gap. Thus by replacing the SAM with a sturdier layer results in increased stability of the NPoM. Functionalized nanoparticle based NPoMs indicate that the molecular rearrangement is unavoidable when the NPoMs are exposed to laser and the contribution of the surface restructuring, during self-assembly of SAM molecules, is not great if any.

Measurements with constant power and laser wavelength at 632 nm, and 710 nm on all the samples indicate that laser detuning from the dipole mode does have a slight impact on the behavior of the NPoMs. The difference in stability observed between S2 and S24 cannot be simply attributed to their different initial resonance position, however the role of the higher order dipole mode must be investigated further.

The changes in peak intensity of the dipole mode with laser power are slightly different for the two types of NPoMs (Figure 5.15 b). While the continuous decrease in the peak intensity for NPoMs on S24 is correlated with the redshift of the peak wavelength, the decrease in gap height alone cannot explain the decrease in peak intensity as shown by BEM simulations in Figure 5.24 d. This discrepancy is attributed to phenomena such as electron tunneling and charge screening that begin to play a significant role in sub-nanometer gap sizes and cannot be incorporated into simulations easily [82]. Moreover, changes in electrical conductivity and electron tunneling abilities of molecules occur as their orientation is varied [156, 158, 159, 160]. The laser-induced re-organization of the BPT SAM in S24 from densely-packed phase to sparsely-packed phase with the lying-down molecules is very likely associated with the changes in conductivity and charge tunneling properties of molecules. The difference in the density of molecules within the NPoMs on S2 and S24 could also have an impact on the tunneling properties and the overall behavior of the dipole mode. Lastly, increase in AuNS facet size, Au adatom density, and restructuring of the Au surface during incubation are also important factors and may play a role in explaining the experimental results in all their details. Further work is required to develop a comprehensive understanding of metal-molecule plasmonic nanojunctions and how to tailor their stability and other properties by surface science and molecular engineering. (The text in this paragraph is extracted from [81].)



## 6 Conclusion and Outlook

In conclusion, light matter interaction at the nanoscale was investigated using nanoparticle on mirror (NPoM) plasmonic nanocavities. The structure consists of a gold (Au) nanoparticle placed within nanometer range of a flat Au surface (mirror). This construct in particular supports a localized surface plasmon resonance (LSPR) corresponding to the excitation of a dipole in the particle normal to the substrate. Excitation of the dipole mirror image in the film results in the formation of a gap plasmon mode with the EM field confined in the gap to volumes far less than the diffraction limit – approximately 10 million times smaller by careful selection of parameters. As a part of this thesis, such structures were produced using molecular self-assembly on atomically smooth, patterned Au mirrors. As the commercial available Au films have high values of surface roughness, two process flows, using state of the art photolithography techniques, were developed and established to obtain the Au substrates. These patterns were designed solely with the intent of enabling convenient localization of the NPoM structures however there are other uses of these as well. Self-assembled monolayers (SAM) were prepared over the mirror to position the nanoparticle above the mirror with nanometer scale precision.

A custom optical setup was also constructed to perform Raman and elastic scattering spectroscopy experiments on the fabricated nanostructures. Three separate lasers mounted in the setup can be used to excite the molecules either individually or simultaneously with optical powers ranging from a few  $\mu\text{W}$  to 100's of mW. The emission wavelength of one of the laser can be tuned from 710 nm to 850 nm thus a wavelength sweep across the LSPR mode of the NPoM can be performed to probe vibrational amplification and damping regimes. The two other laser wavelengths at 532 nm and 632 nm can also be used to perform photoluminescence and Raman experiments. The scattering spectra depicting the plasmonic response of the NPoM structure can also be obtained by illuminating the structure from the side by a white light source. By combining laser excitation with the scattering spectroscopy, the influence of the laser parameter, such as wavelength and power, on the NPoM structures can be tracked. The setup was automated using off the shelf parts and could perform complex power and wavelength sweeping sequences, which would otherwise require a significant amount of time.

By sweeping the laser wavelength and power on single crystal silicon (Si) and diamond substrates, the absolute temperature could be extracted with reasonable accuracy. Laser powers of several hundred  $\mu\text{W}$  were used to obtain the anti-Stokes peaks with a decent signal to noise ratio (SNR). It was found that the NPoMs were unable to bear such high powers and degraded soon after laser exposure. Thus by performing exposure with constant as well as sweeping laser powers along with the acquisition of the scattering spectra, the optically driven structural variations in the NPoM could be observed through the changes in the dipole mode. Although these changes in the scattering spectra can be supposedly attributed to the restructuring of the nanoparticle under the intense laser beam [148, 154], the influence of the incubation time on the behavior of the NPoM cannot be explained. This change in the optical properties of the NPoM can only be understood by taking into account the molecular orientation within the gap. Longer incubation time (S24) results in samples having well-organized, highly packed SAM with the molecules being almost upright as indicated by STM scans. When subjected to laser beam, these molecules reorient themselves in a lying-down position resulting in decrease of the gap height. This is translated into redshift and decrease in the scattering intensity of the dipole mode. Alternatively, sample prepared with low incubation time have a lying down orientation of molecule and irradiating with laser has little effect. To validate the proposed explanation, several other samples with different spacer configurations were prepared. These samples helped in understanding influence of adatoms on the mirror, molecular conductivity and nanoparticle shape on the stability of the NPoM. It was found that NPoMs prepared with dielectric gap layers could sustain much higher levels of power without substantial change in their scattering spectra. Moreover, the Raman signal recorded during the exposure hints that majority of the changes in NPoM with dielectric gaps are due to the citrate ions present on the surface of Au nanoparticles. The effect of the gap conductivity was also investigated by using BPDT to make a conductive contact between the nanoparticle and the mirror. In this case, the difference between S2 and S24 was decreased as the presence of the conductive contact in S24 samples increases the stability of the NPoMs. Lastly, by replacing nanospheres with nanocubes, the effect of the electric field confinement was investigated. Even in this case the response of S2 and S24 NPoMs is quite distinct. All the experimental results in conjunction with simulations stress the importance of the structural parameters of SAM layer in NPoMs.

While we have addressed the stability of the NPoMs by observing the scattering spectra, influence of the molecular vibrations needs to be investigated further. The Raman data from the power dependence measurements presented in this thesis can be rigorously analyzed to understand the connection between the stability of the NPoM. Moreover, the sudden appearance of sharp peaks recorded in the Raman spectra must be compared to the theoretically estimated vibrational mode of BPT. The instantaneous fluctuations and the drift of the background under the Stokes sideband of the Raman signal can also be investigated. It is also important to characterize the role of plasmonic modes that largely contribute to the EM field enhancement within the gap. Optomechanical effects considering the coupling between molecular vibrations and the LSPR could also be studied by performing wavelength dependence measurement on the NPoMs once the stability of the structures has been addressed. This theory predicts a new regime where an out

---

of equilibrium phonon population in the analyte molecules is created by parametric amplification under laser excitation. This requires that the phonon creation rate be large compared to their decay rate, demanding extreme field confinement and enhancement.





# A Appendix

## A.1 Raman from citrates on ALD-NPoM samples

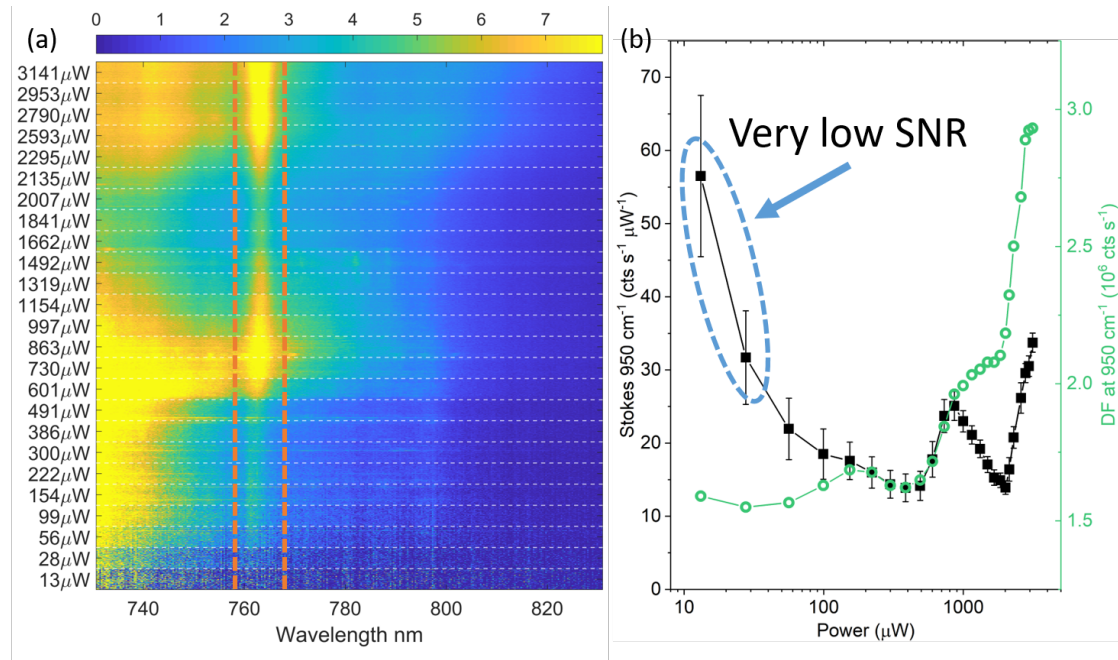


Figure A.1: (a) Stokes Raman spectra from ALD-NPoM at different power laser powers. The laser wavelength was 710 nm. The Raman mode of citrate at  $950 \text{ cm}^{-1}$  is indicated by dash orange lines. (b) The amplitude of the citrate Raman mode (black line) and the DF intensity at the same spectral position (green line).

## A.2 Scattering at 632 nm (S2 BPT vs. S2 BPDT)

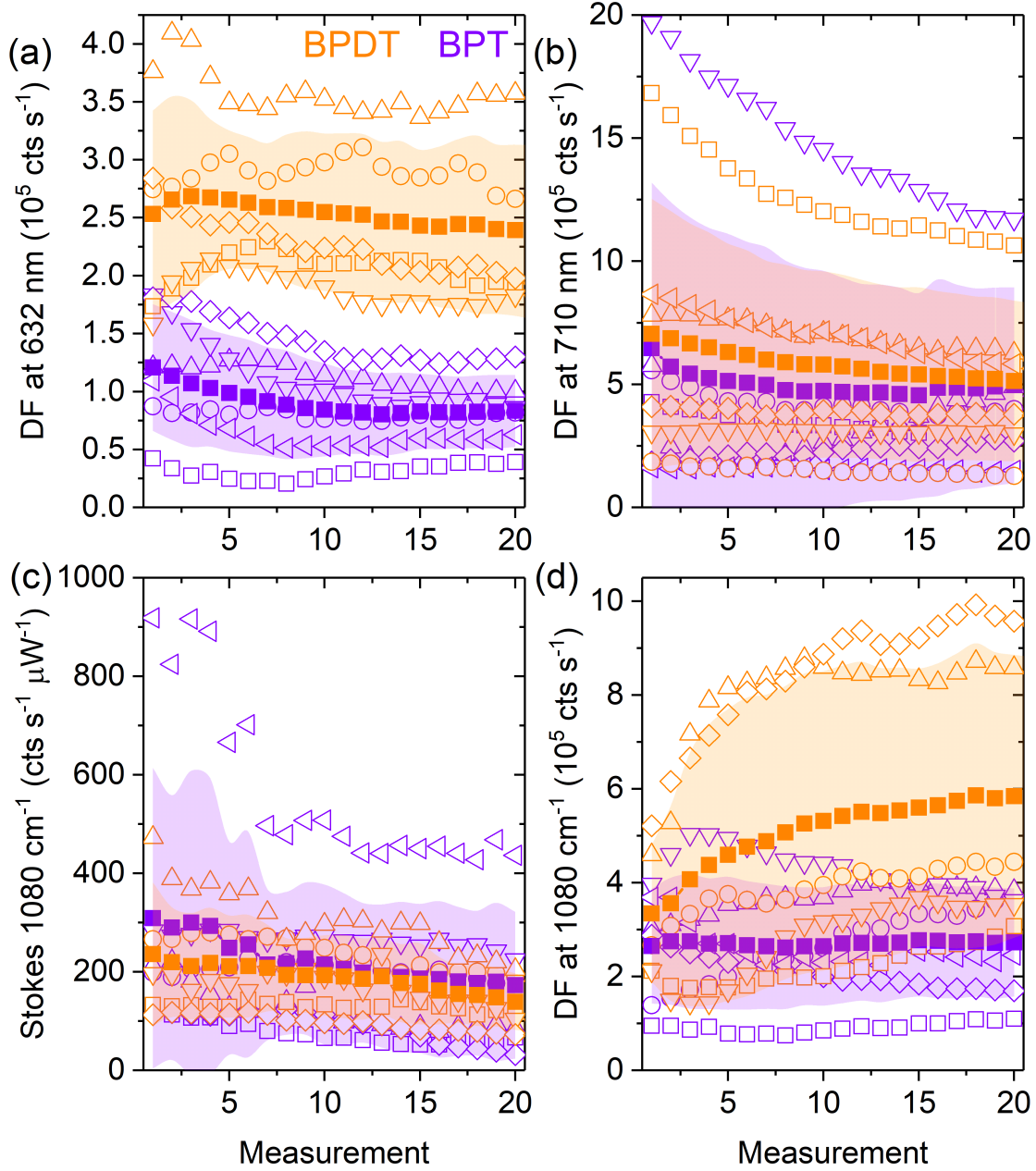


Figure A.2: **(a)** The DF at 632 nm indicates the difference between the S2 NPoMs (samples prepared by 2 hour incubation) with BPDT and BPT. **(b)** The DF at 710 nm are not very different for BPT and BPDT. **(c)** The intensity of the stokes peak at 1080  $cm^{-1}$  during excitation with 632 nm. **(d)** The intensity of the DF at 1080  $cm^{-1}$  during excitation with 632 nm.

## A.3 Scattering at 632 nm Au nanocubes (S2 vs. S24)

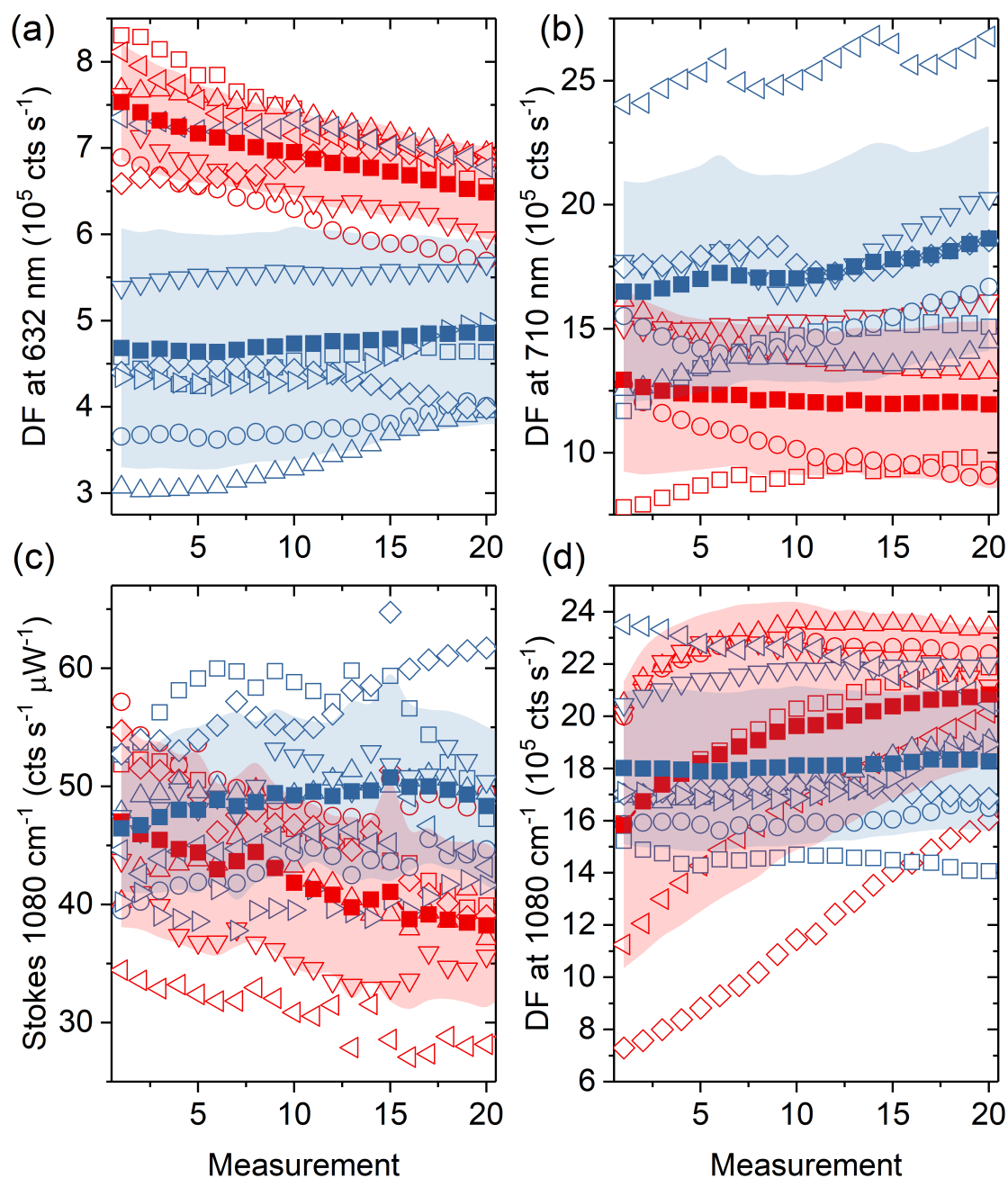


Figure A.3: **(a)** The DF at 632 nm indicates the difference between the S2 NPoMs (blue) and S24 NPoMs (red) with AuNCs. **(b)** The DF at 710 nm are not very different for S2 and S24. **(c)** The intensity of the stokes peak at  $1080\text{ cm}^{-1}$  during excitation with 632 nm. **(d)** The intensity of the DF at  $1080\text{ cm}^{-1}$  during excitation with 632 nm.

## A.4 Effect of refractive index

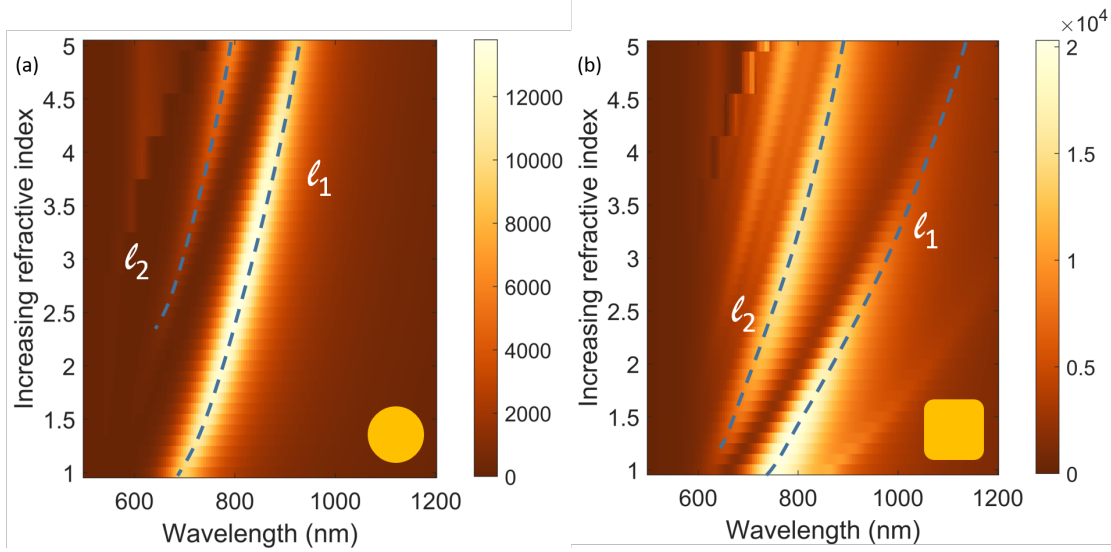


Figure A.4: Simulations reveal that the refractive index of the gap layer in the NPoM has a dramatic influence on the scattering spectra. **(a)** shows the scattering spectra for 80 nm diameter Au nanosphere with 30 nm diameter facet on the bottom placed 1.4 nm above an Au mirror. The BDP mode ( $l_1$ ) and the higher order dipole mode ( $l_2$ ) tend to redshift with increase in refractive index. Similar trends are also observed if the Au nanosphere was replaced by a Au nanocubes with 75 nm edge length and rounded corners **(b)**.

## A.5 Effect of gap size with *s* polarization

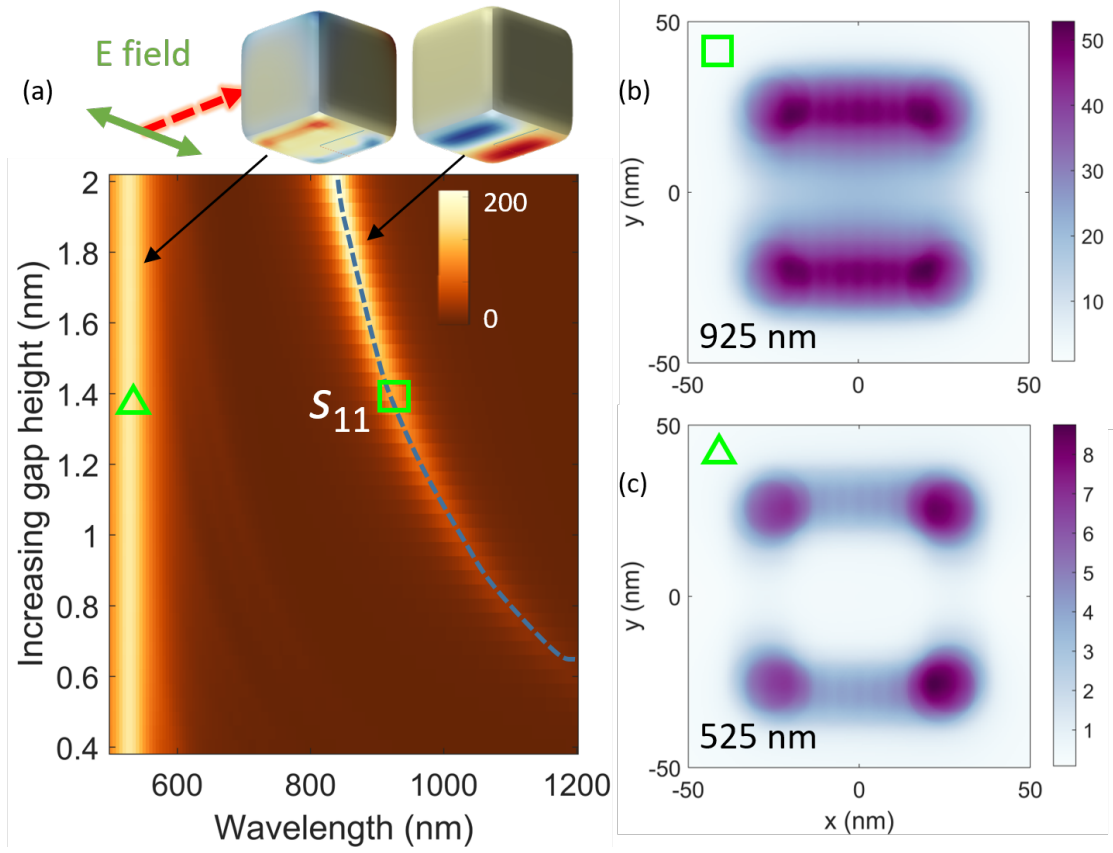


Figure A.5: Simulations show the scattering spectra for NPoM with increasing gap height between the Au nanocube and the mirror. The edge length of Au nanocube was taken to be 75 nm, while incoming E field had *s* polarization. In this case the only the transverse mode of the nanocube (525 nm) and the cavity mode of the NPoM ( $s_{11}$ ) contribute to the scattering spectra (a). The redshift and decrease amplitude of ( $s_{11}$ ) with decrease in gap height could be attributed to the increase in interaction with the mirror substrate [33]. Considering a gap height of 1.4 nm, the E field distributions in the gap for the  $s_{11}$  mode and the transverse mode are shown in (b) and (c) respectively. The colorbar represents the enhancement of the incoming of E field. During the simulations the refractive index of the gap layer was kept constant at 1.4.

## A.6 Effect of gap size with $p$ polarization

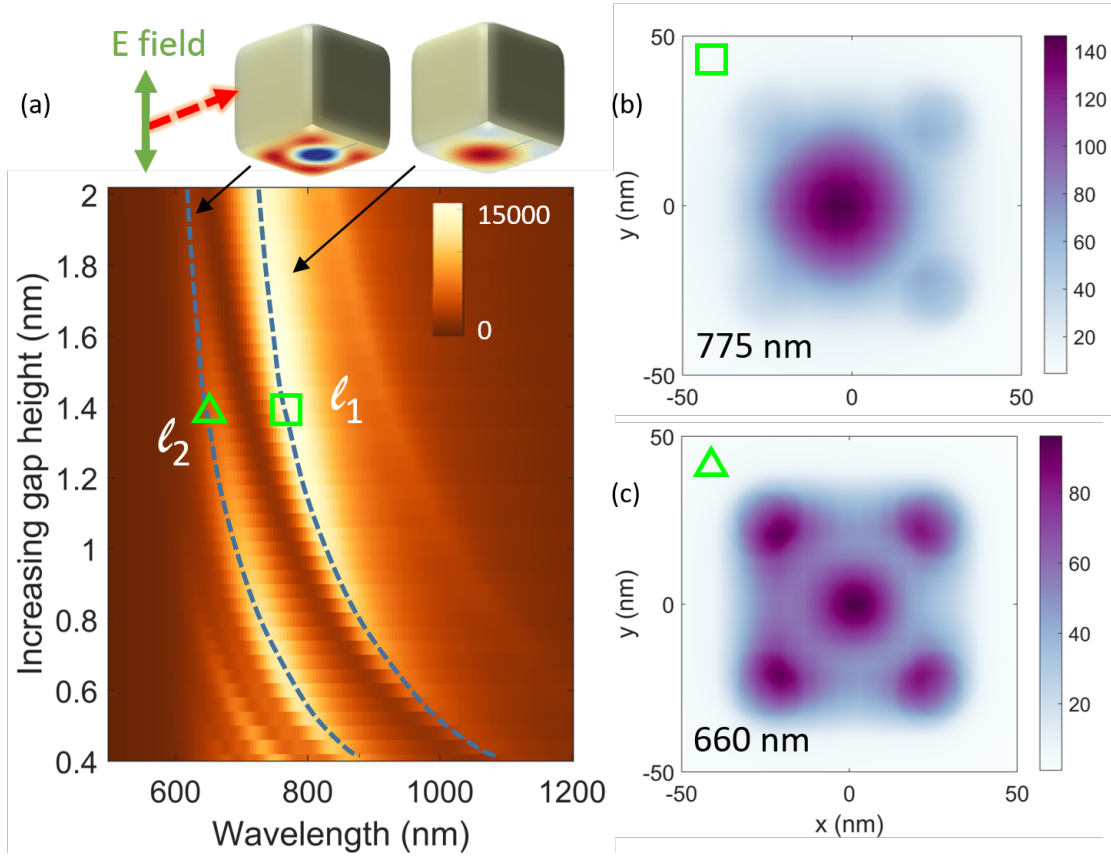


Figure A.6: Simulations are performed with parameters identical to Figure A.5 with the exception that the incoming E field had p polarization. Here, the BDP ( $l_1$ ) as well as the higher order dipole mode ( $l_2$ ) contribute mostly to the scattering spectra (a) but the ( $s_{11}$ ) is also present (a). Also, by comparing the scattering spectra with the two polarization it is evident that  $l_2$  is dipolar in nature. Considering a gap height of 1.4 nm, the E field distributions in the gap for the  $l_1$  mode and the ( $l_2$ ) are shown in (b) and (c) respectively. The colorbar represents the enhancement of the incoming of E field.



## A.7 Effect of rotation with Au nanocubes

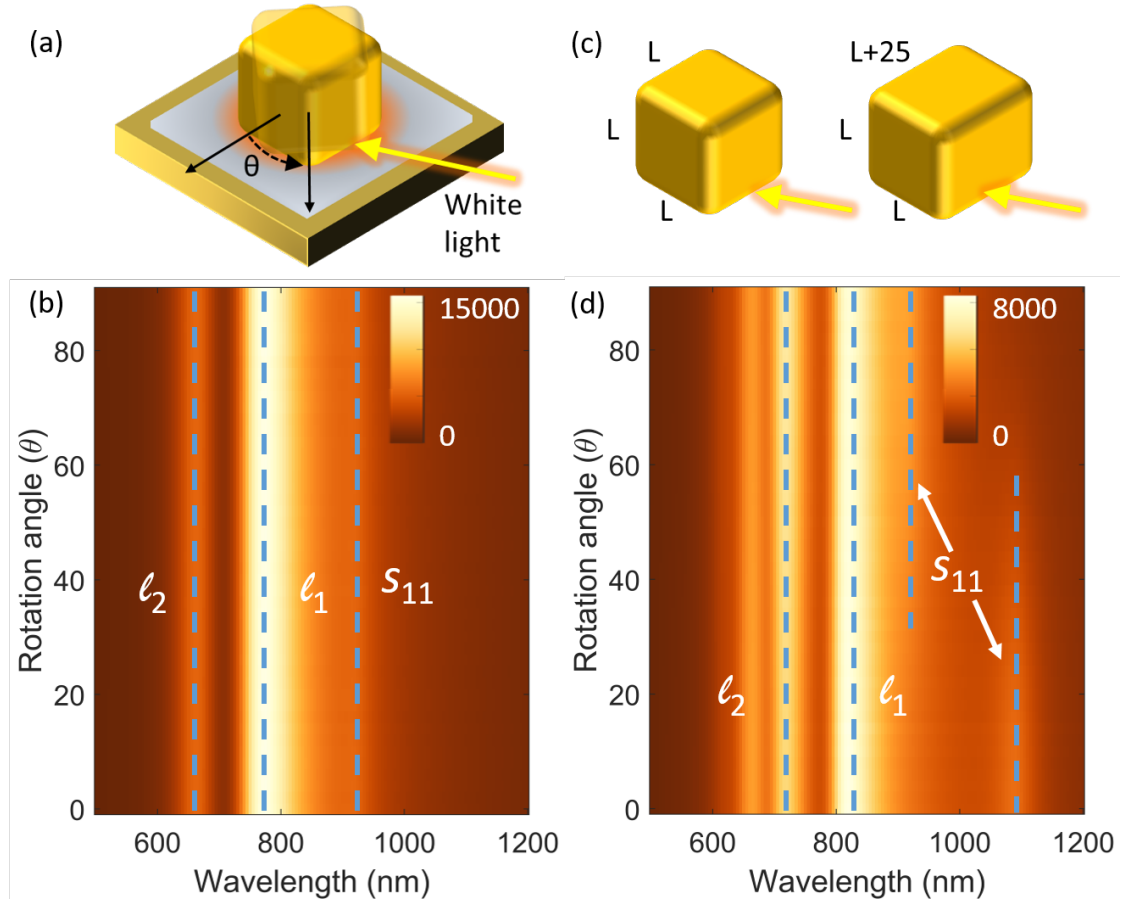


Figure A.7: **(a)** Schematics show the rotation of the Au nanocube by an angle  $\theta$  along the normal of the mirror. **(b)** Simulated scattering spectra with the Au nanocube being at different angle. No change is observed in the dipolar ( $\ell_1$ ,  $\ell_2$ ) as well as the cavity mode ( $s_{11}$ ). The simulations were performed with an Au nanocube with 75 nm edge length placed 1.4 nm above the mirror. The gap layer was modelled as a dielectric with a refractive index of 1.4. **(c)** Schematics shows Au nanocubes modelled earlier and another slightly elongated Au nanocubes. **(d)** The scattering spectra in case of rotation of a slightly elongated Au nanocube show no change in the dipolar modes. On the other hand the  $s_{11}$  shows a visible shift as the angle is tuned.



# Bibliography

- [1] E. Prodan, *Science* **302**, 419 (2003).
- [2] P. Bharadwaj, B. Deutsch, and L. Novotny, *Advances in Optics and Photonics* **1**, 438 (2009).
- [3] J. J. Baumberg, J. Aizpurua, M. H. Mikkelsen, and D. R. Smith, *Nature Materials* **18**, 668 (2019).
- [4] K. M. Mayer and J. H. Hafner, *Chemical Reviews* **111**, 3828 (2011), publisher: American Chemical Society.
- [5] M. W. Knight, H. Sobhani, P. Nordlander, and N. J. Halas, *Science* **332**, 702 (2011).
- [6] S. Linic, U. Aslam, C. Boerigter, and M. Morabito, *Nature Materials* **14**, 567 (2015).
- [7] H. Huh, H. D. Trinh, D. Lee, and S. Yoon, *ACS Applied Materials & Interfaces* **11**, 24715 (2019).
- [8] A. P. Olson, C. T. Ertsgaard, S. N. Elliott, and N. C. Lindquist, *ACS Photonics* **3**, 329 (2016), publisher: American Chemical Society.
- [9] M. L. Brongersma and V. M. Shalaev, *Science* **328**, 440 (2010).
- [10] N. Farmakidis, N. Youngblood, X. Li, J. Tan, J. L. Swett, Z. Cheng, C. D. Wright, W. H. P. Pernice, and H. Bhaskaran, *Science Advances* **5**, eaaw2687 (2019).
- [11] F. Benz, M. K. Schmidt, A. Dreismann, R. Chikkaraddy, Y. Zhang, A. Demetriadou, C. Carnegie, H. Ohadi, B. de Nijs, R. Esteban, J. Aizpurua, and J. J. Baumberg, *Science* **354**, 726 (2016).
- [12] R. Chikkaraddy, B. de Nijs, F. Benz, S. J. Barrow, O. A. Scherman, E. Rosta, A. Demetriadou, P. Fox, O. Hess, and J. J. Baumberg, *Nature* **535**, 127 (2016).
- [13] P. Vasa and C. Lienau, *ACS Photonics* **5**, 2 (2018).
- [14] M. Scalora, M. A. Vincenti, D. de Ceglia, V. Roppo, M. Centini, N. Akozbek, and M. J. Bloemer, *Physical Review A* **82**, 043828 (2010).

## Bibliography

---

- [15] J. Renger, R. Quidant, N. van Hulst, and L. Novotny, *Physical Review Letters* **104**, 046803 (2010).
- [16] G. Baffou and R. Quidant, *Laser & Photonics Reviews* **7**, 171 (2013).
- [17] E. Polo, P. del Pino, B. Pelaz, V. Grazu, and J. M. de la Fuente, *Chemical Communications* **49**, 3676 (2013).
- [18] R. Zhou and F. Basile, *Analytical Chemistry* **89**, 8704 (2017).
- [19] H. Wang, D. W. Brandl, P. Nordlander, and N. J. Halas, *Accounts of Chemical Research* **40**, 53 (2007).
- [20] J. T. Hugall, A. Singh, and N. F. van Hulst, *ACS Photonics* **5**, 43 (2018).
- [21] A. Klinkova, R. M. Choueiri, and E. Kumacheva, *Chemical Society Reviews* **43**, 3976 (2014).
- [22] A. Kuzyk, R. Jungmann, G. P. Acuna, and N. Liu, *ACS Photonics* **5**, 1151 (2018).
- [23] P. Aravind, R. Rendell, and H. Metiu, *Chemical Physics Letters* **85**, 396 (1982).
- [24] R. Ruppin, *Physical Review B* **45**, 11209 (1992).
- [25] P. Nordlander and E. Prodan, *Nano Letters* **4**, 2209 (2004).
- [26] C. Ciraci, R. T. Hill, J. J. Mock, Y. Urzhumov, A. I. Fernandez-Dominguez, S. A. Maier, J. B. Pendry, A. Chilkoti, and D. R. Smith, *Science* **337**, 1072 (2012).
- [27] H. Gleiter, *Acta Materialia* **48**, 1 (2000).
- [28] L. Kastrup and S. W. Hell, *Angewandte Chemie International Edition* **43**, 6646 (2004),  
\_eprint: <https://onlinelibrary.wiley.com/doi/pdf/10.1002/anie.200461337>.
- [29] J. Waxenegger, A. Trügler, and U. Hohenester, *Computer Physics Communications* **193**, 138 (2015).
- [30] J. Gong, G. Li, and Z. Tang, *Nano Today* **7**, 564 (2012).
- [31] A. O. Pinchuk and G. C. Schatz, *Materials Science and Engineering: B E-MRS 2007 Spring Conference Symposium A: Sub-wavelength photonics throughout the spectrum: Materials and Techniques*, **149**, 251 (2008).
- [32] F. Benz, R. Chikkaraddy, A. Salmon, H. Ohadi, B. de Nijs, J. Mertens, C. Carnegie, R. W. Bowman, and J. J. Baumberg, *The Journal of Physical Chemistry Letters* **7**, 2264 (2016).
- [33] C. Tserkezis, R. Esteban, D. O. Sigle, J. Mertens, L. O. Herrmann, J. J. Baumberg, and J. Aizpurua, *Physical Review A* **92**, 053811 (2015).

- 
- [34] I. Romero, J. Aizpurua, G. W. Bryant, and F. J. García De Abajo, *Optics Express* **14**, 9988 (2006).
- [35] K. J. Savage, M. M. Hawkeye, R. Esteban, J. Borisov, Andrei G. and Aizpurua, and J. J. Baumberg, *Nature* **491** (2012).
- [36] R. T. Hill, J. J. Mock, A. Hucknall, S. D. Wolter, N. M. Jokerst, D. R. Smith, and A. Chilkoti, *ACS Nano* **6**, 9237 (2012), publisher: American Chemical Society.
- [37] W. Cheng, M. J. Campolongo, S. J. Tan, and D. Luo, *Nano Today* **4**, 482 (2009).
- [38] J. Huang, F. Kim, A. R. Tao, S. Connor, and P. Yang, *Nature Materials* **4**, 896 (2005), bandiera\_abtest: a Cg\_type: Nature Research Journals Number: 12 Primary\_atype: Research Publisher: Nature Publishing Group.
- [39] R. Volinsky and R. Jelinek, *Angewandte Chemie* **121**, 4610 (2009), \_eprint: <https://onlinelibrary.wiley.com/doi/pdf/10.1002/ange.200900559>.
- [40] J. Henzie, M. Grünwald, A. Widmer-Cooper, P. L. Geissler, and P. Yang, *Nature Materials* **11**, 131 (2012), bandiera\_abtest: a Cg\_type: Nature Research Journals Number: 2 Primary\_atype: Research Publisher: Nature Publishing Group Subject\_term: Nanoparticles;Self-assembly;Theory and computation Subject\_term\_id: nanoparticles;self-assembly;theory-and-computation.
- [41] Z. Nie, D. Fava, E. Kumacheva, S. Zou, G. C. Walker, and M. Rubinstein, *Nature Materials* **6**, 609 (2007), bandiera\_abtest: a Cg\_type: Nature Research Journals Number: 8 Primary\_atype: Research Publisher: Nature Publishing Group.
- [42] T.-C. Lee and O. A. Scherman, *Chem. Commun.* **46**, 2438 (2010), publisher: The Royal Society of Chemistry.
- [43] A. P. Alivisatos, K. P. Johnsson, X. Peng, T. E. Wilson, C. J. Loweth, M. P. Bruchez, and P. G. Schultz, *Nature* **382**, 609 (1996), bandiera\_abtest: a Cg\_type: Nature Research Journals Number: 6592 Primary\_atype: Research Publisher: Nature Publishing Group.
- [44] C. V. Raman and K. S. Krishnan, *Nature* **122**, 12 (1928), bandiera\_abtest: a Cg\_type: Nature Research Journals Number: 3062 Primary\_atype: Research Publisher: Nature Publishing Group.
- [45] M. Fleischmann, P. J. Hendra, and A. J. McQuillan, *Chemical Physics Letters* **26**, 163 (1974).
- [46] K. Kneipp, Y. Wang, H. Kneipp, L. T. Perelman, I. Itzkan, R. R. Dasari, and M. S. Feld, *Physical Review Letters* **78**, 1667 (1997).
- [47] S. Nie and S. R. Emory, *Science* **275**, 1102 (1997), publisher: American Association for the Advancement of Science Section: Report.

## Bibliography

---

- [48] D. L. Jeanmaire and R. P. Van Duyne, *Journal of Electroanalytical Chemistry and Interfacial Electrochemistry* **84**, 1 (1977).
- [49] M. G. Albrecht and J. A. Creighton, *Journal of the American Chemical Society* **99**, 5215 (1977), publisher: American Chemical Society.
- [50] J. R. Lombardi, R. L. Birke, T. Lu, and J. Xu, *The Journal of Chemical Physics* **84**, 4174 (1986), publisher: American Institute of Physics.
- [51] M. Moskovits, *The Journal of Chemical Physics* **69**, 4159 (1978), publisher: American Institute of Physics.
- [52] M. K. Schmidt, R. Esteban, F. Benz, J. J. Baumberg, and J. Aizpurua, *Faraday Discussions* **205**, 31 (2017).
- [53] P. Roelli, C. Galland, N. Piro, and T. J. Kippenberg, *Nature Nanotechnology* **11**, 164 (2016), bandiera\_abtest: a Cg\_type: Nature Research Journals Number: 2 Primary\_atype: Research Publisher: Nature Publishing Group Subject\_term: Biosensors;Nanophotonics and plasmonics;Optomechanics Subject\_term\_id: biosensors;nanophotonics-and-plasmonics;optomechanics.
- [54] S. L. Kleinman, B. Sharma, M. G. Blaber, A.-I. Henry, N. Valley, R. G. Freeman, M. J. Natan, G. C. Schatz, and R. P. Van Duyne, *Journal of the American Chemical Society* **135**, 301 (2013), publisher: American Chemical Society.
- [55] A. D. McFarland, M. A. Young, J. A. Dieringer, and R. P. Van Duyne, *The Journal of Physical Chemistry B* **109**, 11279 (2005), publisher: American Chemical Society.
- [56] B. J. Kennedy, S. Spaeth, M. Dickey, and K. T. Carron, *The Journal of Physical Chemistry B* **103**, 3640 (1999), publisher: American Chemical Society.
- [57] Pilot, Signorini, Durante, Orian, Bhamidipati, and Fabris, *Biosensors* **9**, 57 (2019).
- [58] C. B. Saltonstall, J. Serrano, P. M. Norris, P. E. Hopkins, and T. E. Beechem, *Review of Scientific Instruments* **84**, 064903 (2013), publisher: American Institute of Physics.
- [59] R. C. Maher, C. M. Galloway, E. C. Le Ru, L. F. Cohen, and P. G. Etchegoin, *Chemical Society Reviews* **37**, 965 (2008).
- [60] H. Brugger and P. W. Epperlein, *Applied Physics Letters* **56**, 1049 (1990), publisher: American Institute of Physics.
- [61] R. C. Maher, J. Hou, L. F. Cohen, E. C. Le Ru, J. M. Hadfield, J. E. Harvey, P. G. Etchegoin, F. M. Liu, M. Green, R. J. C. Brown, and M. J. T. Milton, *The Journal of Chemical Physics* **123**, 084702 (2005).
- [62] P. Apell, R. Monreal, and S. Lundqvist, *Physica Scripta* **38**, 174 (1988), publisher: IOP Publishing.



- [63] T. Zhang, G. Lu, H. Shen, K. Shi, Y. Jiang, D. Xu, and Q. Gong, *Scientific Reports* **4**, 3867 (2014), bandiera\_abtest: a Cc\_license\_type: cc\_y Cg\_type: Nature Research Journals Number: 1 Primary\_atype: Research Publisher: Nature Publishing Group Subject\_term: Fluorescence spectroscopy;Nanoparticles;Nanophotonics and plasmonics;Raman spectroscopy Subject\_term\_id: fluorescence-spectrometry;nanoparticles;nanophotonics-and-plasmonics;raman-spectroscopy.
- [64] M. R. Beversluis, A. Bouhelier, and L. Novotny, *Physical Review B* **68**, 115433 (2003), publisher: American Physical Society.
- [65] Y.-Y. Cai, E. Sung, R. Zhang, L. J. Tauzin, J. G. Liu, B. Ostovar, Y. Zhang, W.-S. Chang, P. Nordlander, and S. Link, *Nano Letters* **19**, 1067 (2019).
- [66] J. T. Hugall and J. J. Baumberg, *Nano Letters* **15**, 2600 (2015).
- [67] J. R. M. Saavedra, A. Asenjo-Garcia, and F. J. García de Abajo, *ACS Photonics* **3**, 1637 (2016).
- [68] X. Xie and D. G. Cahill, *Applied Physics Letters* **109**, 183104 (2016), publisher: American Institute of Physics.
- [69] T. Jollans, M. Caldarola, Y. Sivan, and M. Orrit, *The Journal of Physical Chemistry A* **124**, 6968 (2020), publisher: American Chemical Society.
- [70] H. Sugimoto and M. Fujii, *ACS Photonics* **5**, 1986 (2018), publisher: American Chemical Society.
- [71] S. L. McCarthy and J. Lambe, *Applied Physics Letters* **30**, 427 (1977).
- [72] W. R. Holland and D. G. Hall, *Physical Review B* **27**, 7765 (1983).
- [73] T. Kume, S. Hayashi, and K. Yamamoto, *Physical Review B* **55**, 4774 (1997).
- [74] E. Hutter, J. H. Fendler, and D. Roy, *The Journal of Physical Chemistry B* **105**, 11159 (2001).
- [75] T. Okamoto and I. Yamaguchi, *The Journal of Physical Chemistry B* **107**, 10321 (2003).
- [76] J. J. Mock, R. T. Hill, A. Degiron, S. Zauscher, A. Chilkoti, and D. R. Smith, *Nano Letters* **8**, 2245 (2008), publisher: American Chemical Society.
- [77] D. Y. Lei, A. I. Fernández-Domínguez, Y. Sonnefraud, K. Appavoo, R. F. Haglund, J. B. Pendry, and S. A. Maier, *ACS Nano* **6**, 1380 (2012), publisher: American Chemical Society.
- [78] J. J. Mock, R. T. Hill, Y.-J. Tsai, A. Chilkoti, and D. R. Smith, *Nano Letters* **12**, 1757 (2012), publisher: American Chemical Society.

## Bibliography

---

- [79] J. B. Lassiter, F. McGuire, J. J. Mock, C. Ciraci, R. T. Hill, B. J. Wiley, A. Chilkoti, and D. R. Smith, *Nano Letters* **13**, 5866 (2013), publisher: American Chemical Society.
- [80] C. Lumdee, B. Yun, and P. G. Kik, *Nanoscale* **7**, 4250 (2015), publisher: The Royal Society of Chemistry.
- [81] A. Ahmed, K. Banjac, S. S. Verlekar, F. P. Cometto, M. Lingenfelder, and C. Galland, *ACS Photonics* **8**, 1863 (2021), publisher: American Chemical Society.
- [82] W. Zhu, R. Esteban, A. G. Borisov, J. J. Baumberg, P. Nordlander, H. J. Lezec, J. Aizpurua, and K. B. Crozier, *Nature Communications* **7**, 11495 (2016).
- [83] M. A. George, W. S. Glaunsinger, T. Thundat, and S. M. Lindsay, *Thin Solid Films* **189**, 59 (1990).
- [84] M. Todeschini, A. Bastos da Silva Fanta, F. Jensen, J. B. Wagner, and A. Han, *ACS Applied Materials & Interfaces* **9**, 37374 (2017), publisher: American Chemical Society.
- [85] L. Leandro, R. Malureanu, N. Rozlosnik, and A. Lavrinenko, *ACS Applied Materials & Interfaces* **7**, 5797 (2015), publisher: American Chemical Society.
- [86] D. I. Yakubovsky, Y. V. Stebunov, R. V. Kirtaev, G. A. Ermolaev, M. S. Mironov, S. M. Novikov, A. V. Arsenin, and V. S. Volkov, *Advanced Materials Interfaces* **6**, 1900196 (2019), \_eprint: <https://onlinelibrary.wiley.com/doi/pdf/10.1002/admi.201900196>.
- [87] M. Bosman, L. Zhang, H. Duan, S. F. Tan, C. A. Nijhuis, C. Qiu, and J. K. W. Yang, *Scientific Reports* **4**, 10.1038/srep05537 (2015).
- [88] M. Hegner, P. Wagner, and G. Semenza, *Surface Science* **291**, 39 (1993).
- [89] P. Nagpal, N. C. Lindquist, S.-H. Oh, and D. J. Norris, *Science* **325**, 594 (2009).
- [90] N. C. Lindquist, P. Nagpal, A. Lesuffleur, D. J. Norris, and S.-H. Oh, *Nano Letters* **10**, 1369 (2010).
- [91] C. Lumdee, B. Yun, and P. G. Kik, *The Journal of Physical Chemistry C* **117**, 19127 (2013), publisher: American Chemical Society.
- [92] G. Decher, *Science* **277**, 1232 (1997), publisher: American Association for the Advancement of Science Section: Special Articles.
- [93] S. Kim, W. Choi, D. J. Kim, H. S. Jung, D.-H. Kim, S.-H. Kim, and S.-G. Park, *Nanoscale* **12**, 12942 (2020), publisher: The Royal Society of Chemistry.
- [94] W. C. Bigelow, D. L. Pickett, and W. A. Zisman, *Journal of Colloid Science* **1**, 513 (1946).
- [95] R. G. Nuzzo and D. L. Allara, *Journal of the American Chemical Society* **105**, 4481 (1983), publisher: American Chemical Society.

- [96] T. W. Schneider and D. A. Buttry, *Journal of the American Chemical Society* **115**, 12391 (1993).
- [97] L. S. Alarcón, L. Chen, V. A. Esaulov, J. E. Gayone, E. A. Sánchez, and O. Grizzi, *The Journal of Physical Chemistry C* **114**, 19993 (2010).
- [98] M. D. Losego, M. E. Grady, N. R. Sottos, D. G. Cahill, and P. V. Braun, *Nature Materials* **11**, 502 (2012).
- [99] M. A. Reed, C. Zhou, C. J. Muller, T. P. Burgin, and J. M. Tour, *Science* **278**, 252 (1997), publisher: American Association for the Advancement of Science Section: Report.
- [100] L. A. Bumm, J. J. Arnold, M. T. Cygan, T. D. Dunbar, T. P. Burgin, L. Jones, D. L. Allara, J. M. Tour, and P. S. Weiss, *Science* **271**, 1705 (1996), publisher: American Association for the Advancement of Science Section: Reports.
- [101] G. Pieters and L. J. Prins, *New Journal of Chemistry* **36**, 1931 (2012), publisher: The Royal Society of Chemistry.
- [102] C. A. Schoenbaum, D. K. Schwartz, and J. W. Medlin, *Journal of Catalysis* **303**, 92 (2013).
- [103] S. Watson, M. Nie, L. Wang, and K. Stokes, *RSC Advances* **5**, 89698 (2015), publisher: The Royal Society of Chemistry.
- [104] D. Mandler and S. Kraus-Ophir, *Journal of Solid State Electrochemistry* **15**, 1535 (2011).
- [105] H. Klauk, U. Zschieschang, J. Pflaum, and M. Halik, *Nature* **445**, 745 (2007), number: 7129 Publisher: Nature Publishing Group.
- [106] W. Azzam, C. Fuxen, A. Birkner, H.-T. Rong, M. Buck, and C. Wöll, *Langmuir* **19**, 4958 (2003), publisher: American Chemical Society.
- [107] E. M. Euti, P. Vélez Romero, O. Linarez Pérez, G. Ruano, E. M. Patrito, G. Zampieri, E. P. M. Leiva, V. A. Macagno, and F. P. Cometto, *Surface Science* **630**, 101 (2014).
- [108] J. Li and Y. J. Yuan, *Langmuir* **30**, 9637 (2014), publisher: American Chemical Society.
- [109] M. Canepa, G. Maidecchi, C. Toccafondi, O. Cavalleri, M. Prato, V. Chaudhari, and V. A. Esaulov, *Physical Chemistry Chemical Physics* **15**, 11559 (2013), publisher: The Royal Society of Chemistry.
- [110] M. Hernandez, P. Chinwangso, K. Cimat, L.-o. Srisombat, T. R. Lee, and S. Baldelli, *The Journal of Physical Chemistry C* **115**, 4688 (2011), publisher: American Chemical Society.
- [111] V. Di Castro, F. Bussolotti, and C. Mariani, *Surface Science* **598**, 218 (2005).
- [112] X. Torrelles, C. Vericat, M. E. Vela, M. H. Fonticelli, M. A. Daza Millone, R. Felici, T.-L. Lee, J. Zegenhagen, G. Muñoz, J. A. Martín-Gago, and R. C. Salvarezza, *The Journal of Physical Chemistry B* **110**, 5586 (2006), publisher: American Chemical Society.

## Bibliography

---

- [113] C. Vericat, M. E. Vela, G. Benitez, P. Carro, and R. C. Salvarezza, *Chemical Society Reviews* **39**, 1805 (2010).
- [114] L. Carbonell, C. M. Whelan, M. Kinsella, and K. Maex, *Superlattices and Microstructures European Materials Research Society 2004, Symposium T. Substrate Nanostructuration: Self-assembling and Nanopatterns*, **36**, 149 (2004).
- [115] S. D. Evans, R. Sharma, and A. Ulman, *Langmuir* **7**, 156 (1991), publisher: American Chemical Society.
- [116] N. Faucheux, R. Schweiss, K. Lützow, C. Werner, and T. Groth, *Biomaterials* **25**, 2721 (2004).
- [117] A. A. S. M. Zahid, M. A. Hanif, I. Lee, M. A. Islam, and J. R. Hahn, *Surface and Interface Analysis* **51**, 1102 (2019), \_eprint: <https://analyticalsciencejournals.onlinelibrary.wiley.com/doi/pdf/10.1002/sia.6697>.
- [118] T. Takami, E. Delamarche, B. Michel, C. Gerber, H. Wolf, and H. Ringsdorf, *Langmuir* **11**, 3876 (1995).
- [119] Y. T. Kim, R. L. McCarley, and A. J. Bard, *Langmuir* **9**, 1941 (1993).
- [120] A. W. Adamson and A. P. Gast, *Physical chemistry of surfaces* (Wiley, New York, 1997) oCLC: 263940491.
- [121] S. A. Claridge, W.-S. Liao, J. C. Thomas, Y. Zhao, H. H. Cao, S. Cheunkar, A. C. Serino, A. M. Andrews, and P. S. Weiss, *Chemical Society Reviews* **42**, 2725 (2013), publisher: The Royal Society of Chemistry.
- [122] G. E. Poirier and E. D. Pylant, *Science* **272**, 1145 (1996), publisher: American Association for the Advancement of Science Section: Reports.
- [123] S. Xu, S. J. N. Cruchon-Dupeyrat, J. C. Garno, G.-Y. Liu, G. Kane Jennings, T.-H. Yong, and P. E. Laibinis, *The Journal of Chemical Physics* **108**, 5002 (1998), publisher: American Institute of Physics.
- [124] G. Haehner, C. Woell, M. Buck, and M. Grunze, *Langmuir* **9**, 1955 (1993), publisher: American Chemical Society.
- [125] M. H. Dishner, P. Taborek, J. C. Hemminger, and F. J. Feher, *Langmuir* **14**, 6676 (1998), publisher: American Chemical Society.
- [126] G. E. Poirier, *Langmuir* **13**, 2019 (1997), publisher: American Chemical Society.
- [127] F. P. Cometto, Z. Luo, S. Zhao, J. A. Olmos-Asar, M. M. Mariscal, Q. Ong, K. Kern, F. Stellacci, and M. Lingenfelder, *Angewandte Chemie* **129**, 16753 (2017), \_eprint: <https://onlinelibrary.wiley.com/doi/pdf/10.1002/ange.201708735>.

- [128] D. Käfer, G. Witte, P. Cyganik, A. Terfort, and C. Wöll, *Journal of the American Chemical Society* **128**, 1723 (2006), publisher: American Chemical Society.
- [129] R. Yamada, H. Wano, and K. Uosaki, *Langmuir* **16**, 5523 (2000), publisher: American Chemical Society.
- [130] S. De Feyter and F. C. De Schryver, *The Journal of Physical Chemistry B* **109**, 4290 (2005), publisher: American Chemical Society.
- [131] D. P. Goronzy, M. Ebrahimi, F. Rosei, Arramel, Y. Fang, S. De Feyter, S. L. Tait, C. Wang, P. H. Beton, A. T. S. Wee, P. S. Weiss, and D. F. Perepichka, *ACS Nano* **12**, 7445 (2018), publisher: American Chemical Society.
- [132] V. Karoutsos, M. Toudas, A. Delimitis, S. Grammatikopoulos, and P. Pouloupoulos, *Thin Solid Films* **520**, 4074 (2012).
- [133] E. A. Wood, *Journal of Applied Physics* **35**, 1306 (1964), publisher: American Institute of Physics.
- [134] T. Y. B. Leung, P. Schwartz, G. Scoles, F. Schreiber, and A. Ulman, *Surface Science* **458**, 34 (2000).
- [135] M. C. Leopold, J. A. Black, and E. F. Bowden, *Langmuir* **18**, 978 (2002), publisher: American Chemical Society.
- [136] I. Horcas, R. Fernández, J. M. Gómez-Rodríguez, J. Colchero, J. Gómez-Herrero, and A. M. Baro, *Review of Scientific Instruments* **78**, 013705 (2007), publisher: American Institute of Physics.
- [137] T. Stangner, H. Zhang, T. Dahlberg, K. Wiklund, and M. Andersson, *Applied Optics* **56**, 5427 (2017).
- [138] A. C. Albrecht, *The Journal of Chemical Physics* **34**, 1476 (1961).
- [139] J. J. Gallardo, J. Navas, D. Zorrilla, R. Alcántara, D. Valor, C. Fernández-Lorenzo, and J. Martín-Calleja, *Applied Spectroscopy* **70**, 1128 (2016).
- [140] F. Benz, C. Tserkezis, L. O. Hermann, B. de Nijs, A. Sanders, D. O. Sigle, L. Pukenas, S. D. Evans, J. Aizpurua, and J. J. Baumberg, *Nano Letters* **15**, 669 (2015).
- [141] F. Benz, B. de Nijs, C. Tserkezis, R. Chikkaraddy, D. O. Sigle, L. Pukenas, S. D. Evans, J. Aizpurua, and J. J. Baumberg, *Optics Express* **23**, 33255 (2015).
- [142] J. C. Love, L. A. Estroff, J. K. Kriebel, R. G. Nuzzo, and G. M. Whitesides, *Chemical Reviews* **105**, 1103 (2005).
- [143] C. Vericat, M. E. Vela, G. Corthey, E. Pensa, E. Cortés, M. H. Fonticelli, F. Ibañez, G. E. Benitez, P. Carro, and R. C. Salvarezza, *RSC Adv.* **4**, 27730 (2014).

## Bibliography

---

- [144] N. Arisnabarreta, G. D. Ruano, M. Lingenfelder, E. M. Patrito, and F. P. Cometto, *Langmuir* **33**, 13733 (2017), publisher: American Chemical Society.
- [145] D. G. Matei, H. Muzik, A. Götzhäuser, and A. Turchanin, *Langmuir* **28**, 13905 (2012).
- [146] F. P. Cometto, E. M. Patrito, P. Paredes Olivera, G. Zampieri, and H. Ascolani, *Langmuir* **28**, 13624 (2012), publisher: American Chemical Society.
- [147] H.-T. Rong, S. Frey, Y.-J. Yang, M. Zharnikov, M. Buck, M. Wühn, C. Wöll, and G. Helmchen, *Langmuir* **17**, 1582 (2001), publisher: American Chemical Society.
- [148] J. Mertens, A. Demetriadou, R. W. Bowman, F. Benz, M.-E. Kleemann, C. Tserkezis, Y. Shi, H. Y. Yang, O. Hess, J. Aizpurua, and J. J. Baumberg, *Nano Letters* **16**, 5605 (2016).
- [149] C. Carnegie, M. Urbieto, R. Chikkaraddy, B. de Nijs, J. Griffiths, W. M. Deacon, M. Kamp, N. Zabala, J. Aizpurua, and J. J. Baumberg, *Nature Communications* **11**, 682 (2020).
- [150] W. Azzam, A. Al-Rashdi, A. Subaihi, M. Rohwerder, M. Zharnikov, and A. Bashir, *Physical Chemistry Chemical Physics* **22**, 13580 (2020), publisher: The Royal Society of Chemistry.
- [151] M. Bürkle, J. K. Viljas, D. Vonlanthen, A. Mishchenko, G. Schön, M. Mayor, T. Wandlowski, and F. Pauly, *Physical Review B* **85**, 10.1103/PhysRevB.85.075417 (2012).
- [152] L. Cui, B. Liu, D. Vonlanthen, M. Mayor, Y. Fu, J.-F. Li, and T. Wandlowski, *Journal of the American Chemical Society* **133**, 7332 (2011).
- [153] N. Kongsuwan, A. Demetriadou, M. Horton, R. Chikkaraddy, J. J. Baumberg, and O. Hess, *ACS Photonics* 10.1021/acsp Photonics.9b01445 (2020).
- [154] A. Xomalis, R. Chikkaraddy, E. Oksenberg, I. Shlesinger, J. Huang, E. C. Garnett, A. F. Koenderink, and J. J. Baumberg, *ACS Nano* **14**, 10562 (2020).
- [155] L. J. Cristina, G. Ruano, R. Salvarezza, and J. Ferrón, *The Journal of Physical Chemistry C* **121**, 27894 (2017), publisher: American Chemical Society.
- [156] W. Haiss, H. van Zalinge, D. Bethell, J. Ulstrup, D. J. Schiffrin, and R. J. Nichols, *Faraday Discuss.* **131**, 253 (2006).
- [157] J. Mertens, M.-E. Kleemann, R. Chikkaraddy, P. Narang, and J. J. Baumberg, *Nano Letters* **17**, 2568 (2017).
- [158] L. Belding, S. E. Root, Y. Li, J. Park, M. Baghbanzadeh, E. Rojas, P. F. Pieters, H. J. Yoon, and G. M. Whitesides, *Journal of the American Chemical Society* **143**, 3481 (2021), publisher: American Chemical Society.
- [159] L.-L. Lin, C.-K. Wang, and Y. Luo, *ACS Nano* **5**, 2257 (2011), publisher: American Chemical Society.



- [160] T. Frederiksen, C. Munuera, C. Ocal, M. Brandbyge, M. Paulsson, D. Sanchez-Portal, and A. Arnau, *ACS Nano* **3**, 2073 (2009), publisher: American Chemical Society.





# AQEEL AHMED

+4915212950019

[aqeel.ahmed@epfl.ch](mailto:aqeel.ahmed@epfl.ch)

## EDUCATION

### **Doctor of Philosophy** | *Photonics*

École Polytechnique Fédérale de Lausanne

Aug. 2017 – Present  
Lausanne, Switzerland

### **Master of Science** | *Lasers and Photonics*

Ruhr University Bochum

Oct. 2014 – July 2017  
Bochum, Germany

### **Bachelor of Science** | *Major: Laser and Optoelectronics*

GIK Institute of Engineering Science and Technology

Aug. 2010 – June 2014  
Topi, Pakistan

## WORK EXPERIENCE

### **Student Assistant**

Ruhr University Bochum

- Modelling charge carrier dynamics in photoconductive antennas

Dec. 2015 – June 2016  
Bochum, Germany

### **Internee**

Pakistan Telecommunication Limited

- Operation and maintenance of main distribution frame (MDF)

July 2013 – Aug. 2013  
Rawalpindi, Pakistan

## DOCTORAL THESIS

### **Investigation of photoinduced effects in plasmonic nanocavities**

## MASTER THESIS AND OTHER PROJECTS

### **Effect of reflectivity modulation of gold film on the pulse duration of ultrashort laser pulses**

Other projects:

- Polarization switching of VCSEL subjected to in plane strain
- Characterization of nanoparticles generated via laser ablation of silicon
- Raman characterization of patterned graphene and graphene oxide

## SKILLS

### **Microfabrication**

Mask preparation, photolithography, dry and wet etching, thin film deposition

### **Programming**

C, C++, Python, ladder diagrams

### **Characterization techniques**

Raman spectroscopy, contact angle measurement, AFM, SEM, FIB, EDX, DLS

### **Scientific Software**

MATLAB, Simulink, AutoCAD, LabView, OpticsStudio, ImageJ, P-Spice, Proteus, MIDE-51, CX Programmer, WPL-soft

## INTERESTS

Computer graphics design with Blender, running, and cooking